Experimental Advances toward a Compact Dual-Species Laser Cooling Apparatus

by

Keith Ladouceur

B.Sc., University of Guelph, 2004

A THESIS SUBMITTED IN PARTIAL FULFILMENT OF
THE REQUIREMENTS FOR THE DEGREE OF

Master of Science

in

The Faculty of Graduate Studies

(Physics)

The University of British Columbia

(Vancouver, Canada)

April, 2008

Abstract

This thesis describes the advances made towards a dual-species magneto-optical trap (MOT) of Li and Rb for use in photoassociation spectroscopy, Feshbach resonance studies, and, as long-term aspirations, the formation of ultracold heteronuclear polar molecules. The initial discussion will focus on a brief theoretical overview of laser cooling and trapping and the production of ultracold molecules from a cold atom source. Subsequently, details of the experimental system, including those pertaining to the required laser light, the vacuum chamber, and the computer control system will be presented. Finally, preliminary optimization and characterization measurements showing the performance of a single species Li MOT are introduced. These measurements demonstrated the loading of over 8×10^7 Li atoms directly into a MOT without the need for a Zeeman slower.

Table of Contents

List of Tables

List of Figures

Acknowledgements

The contributions discussed within this thesis are really a very small part of a much larger whole; as such I owe a great amount of gratitude to all those I've had the pleasure of working with. Their knowledge and dedication are the reason this experiment has progressed so far. To this end I'd like to thank my supervisor, Dr. Kirk Madison, for everything that he has taught me. Dr. David Jones for his perspective and advice. Dr. Bruce Klappauf for patiently ignoring the inanity of my many questions, and Janelle Van Dongen for her pragmatic approach to experiment. Further, I'd like to thank Dr. Art Mills, Dr. Jim Booth, and Swati Singh for their contributions and conversation. To the great many others who I have had the honour of working with, the list is becoming too long to write, know that your insights and friendships have been very much appreciated.

On a more personal side, I would like to thank my family, and in particular my parents, for their for their ever present love and support. It is a great comfort to know that, regardless of my path in life, they are always there to offer encouragement.

Finally, I would like to thank my very patient and understanding girlfriend Katie Dinelle. She has been a source of strength from the beginning, and I could not have seen this to the end without her.

Chapter 1

Introduction

The term 'ultracold' is used to describe temperature regimes below 1μK[5]. At such low temperatures, the subtle many-body quantum effects that are normally suppressed at high temperatures become extremely important. The idea that atoms could be cooled through the use of laser radiation was first proposed by Hänsch and Schawlow [6] in 1975. From this inception, methods of laser cooling and trapping were steadily developed and refined — culminating in 1995 with the first demonstrations of Bose-Einstein condensation in Rubidium[7] and Cesium[8]. These demonstrations showed that the techniques used for cooling and trapping atoms had matured; with a clear experimental path, access to dense samples of ultracold atoms intensified interest and further spurred theoretical and experimental research.

The progression from atoms to molecules is a natural one. The additional internal structure and anisotropic interactions present in molecules make their study a far more intriguing proposition. Unfortunately, this added complexity precludes the simple extension of laser cooling techniques to a source of hot molecules. Undeterred, researchers instead developed methods of forming molecules from a prepared sample of ultracold atoms. These methods include photoassociation, where the free states of a colliding atomic pair are coupled to a vibrationally excited bound molecular state by the introduction of a resonant photon, and Feshbach resonance, where degeneracy of the atomic and molecular states is achieved by tuning an applied magnetic field. The availability of cold, stable molecules in the vibrational ground state are critical in furthering research across many areas of physics and chemistry.

Of particular interest are heteronuclear polar molecules, such as LiRb, as they are characterized by a permanent electric dipole moment. This dipole moment, at ultracold temperatures where the thermal energy of the molecules is low, can be controlled by an applied electric field. Possible applications include the implementation of polar molecules in a lattice as a quantum computation device [9], where a qubit is represented by the alignment of the dipole with or against an electric field. The full depth and breadth of ultracold physics has yet to fully realized, and although the technical difficulties of generating such systems are great, the possible rewards are extremely tantalizing.

The research being conducted within the Quantum Degenerate Gas (QDG) Laboratory is concerned with many of the aspects of these ultracold systems, and as such is quite extensive in its scope. The aim of the project from its inception was to build a modularized infrastructure capable of supporting multiple experiments focused on the study and manipulation of ^{85,87}Rb and ^{6}Li in cold and ultracold atomic and molecular states. Alkali atoms are used most prevalently within ultracold experiments as the single valence electron leads to a simplified energy structure, while the energy difference between the internal states is accessible by optical and near infra-

red light. The high vapour pressure of Rubidium allows for loading from an atomic vapour, while the lower pressure of Lithium requires an effusive oven to generate an atomic source. As a foundation for this infrastructure, an isolated master table was built for generating, locking, and conditioning the light necessary for all species and isotopes. The design of the amplification systems, vacuum chambers, and trapping cells were generalized for use within multiple experimental systems; small deviations from a basic plan would differentiate an experiment probing Feshbach resonances from one concerned with photoassociation spectroscopy. The control system, necessary in such experiments where the timing of the state change of individual devices is critical, was to be developed as a powerful, fully realized method of supporting precise experimental sequencing for data collection.

The following discussion will be focused on the development of this system; the relevant theoretical background, the experimental developments toward a dual-species MOT, and early performance results of the apparatus in a single species Li MOT configuration will be shown. A project of this scope is by necessity long term in nature, as such what I present is merely the state of the apparatus in its current form and not as a finished product.

Chapter 2

Principles of Laser Cooling and Trapping

The interaction of light with matter is fundamental in cooling and trapping dense samples of atomic gases. The mechanical force resulting from this interaction is derived from two basic mechanisms; the scattering force and the dipole force.

2.1 Scattering Force

The scattering force is most naturally developed by considering light as a particle. During the absorption of a photon by an atom, conservation requirements dictate that the atom experiences a momentum shift of $\hbar\mathbf{k}$ where $\mathbf{k}$ is the wave vector of the incoming photon. The excited atom is unstable and will decay back to the ground state through spontaneous emission. The direction of the outgoing photon is determined by the radiation pattern of the transition. Solving the optical Bloch equations for a two-level atom in the presence of a radiation field results in the following expression for the average scattering force [10]

$$F_{scatt} = \hbar\mathbf{k}\frac{\Gamma}{2}\left(\frac{\Omega^2/2}{\delta^2 + (\Gamma^2/4) + (\Omega^2/2)}\right) = \hbar\mathbf{k}\gamma_S \tag{2.1}$$

where Γ is the natural linewidth of the excited state, $\delta = \omega - \omega_O + \mathbf{k}\cdot\mathbf{v}$ corresponds to the detuning of the photon frequency from the atomic resonance with the Doppler shift of the atom taken into account, Ω is the characteristic Rabi frequency of the atom-field interaction, and γ_S is the spontaneous scattering rate.

The Rabi frequency and the natural linewidth are related to the saturation intensity by

$$\frac{I}{I_{sat}} = \frac{2\Omega^2}{\Gamma^2} \tag{2.2}$$

where $I_{sat} = \pi hc/3\lambda^3\tau$, and τ is the decay time for the transition. Introducing this relation to (2.1)

$$F_{scatt} = \hbar\mathbf{k}\frac{\Gamma}{2}\left(\frac{I/I_{sat}}{1 + (I/I_{sat}) + (4\delta^2/\Gamma^2)}\right) \tag{2.3}$$

At high light intensities, this equation reduces to $F_{max} = \hbar\mathbf{k}\Gamma/2$. The rate of spontaneous emission from a two level atom approaches $\Gamma/2$ because the populations in the upper and lower states both approach 1/2.

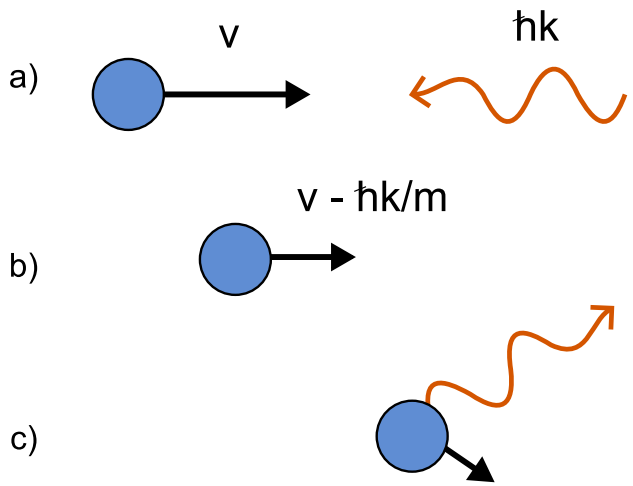

Figure 2.1: Absorption and spontaneous emission process for an atom with initial velocity v. (a) A photon of momentum $\hbar k$ is absorbed by an atom; (b) The atom has been slowed by $\hbar k/m$; (c) Spontaneous emission of a photon in a random direction.

This force can be exploited as a mechanism for slowing down atoms. Since the radiation pattern of the spontaneous emission is symmetric, the emission process does not contribute to the average momentum shift of the atom. Laser light away from the atomic resonance will preferentially scatter from an atom whose velocity $\mathbf{v}$ results in a Doppler shifted detuning δ close to zero.

2.2 Dipole Force

The optical cross section of an atom, when interacting with a resonant radiation field, is of a radius equal to the wavelength of the light; a radius significantly larger than that of the outer electron orbital of atom. It is most intuitive to consider the optical cross section of the atom as a lens. If the light intensity across the atom is not uniform, then the manner in which the atom deflects the light will be non-symmetric. This non-symmetry results in a force acting on the atom due to the momentum change of the light; the force will draw the atom towards the maxima of the radiation field if the light is red detuned, and towards the minima of the field if the light is blue detuned.

The dipole moment for an atom in the presence of a field $\mathbf{E}$ is given by

$$\mathbf{d} = -\alpha \cdot \mathbf{E} \tag{2.4}$$

where α is the polarizability. For a two-level system, α can be expressed as [11]

$$\alpha = 6\pi\epsilon_0 c^3 \frac{\Gamma/\omega_o^2}{\omega_o^2 - \omega^2 - i\left(\omega^2/\omega_o^2\right)^3 \Gamma} \tag{2.5}$$

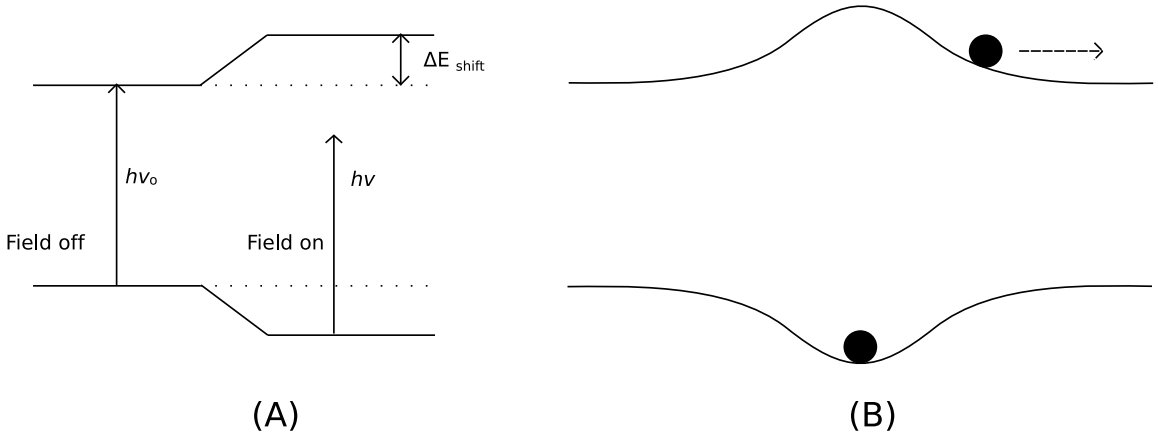

Figure 2.2: A two-level atom in the presence of a red detuned electric field. (a) The energy levels of the atomic states are driven in opposite directions; (b) The presence of a spatially homogeneous field generates a minima in the potential, allowing for atoms to be trapped.

As before, ω_o is the frequency, and Γ the natural linewidth of the ground to excited state transition. The interaction potential of the induced dipole moment with the light field $\mathbf{E}$ is then

$$U_{dip} = -\frac{1}{2}\mathbf{d}\cdot\mathbf{E} = -\frac{1}{2}\epsilon_0 c Re(\alpha) I \tag{2.6}$$

and the dipole force simply

$$F_{dip} = -\nabla U_{dip} = \frac{1}{2\epsilon_0 c} Re(\alpha)\nabla I \tag{2.7}$$

For large detunings ($|\delta| \gg \Gamma$) and high intensities (where $|\delta| \gg \Omega$) the rotating wave approximation becomes valid. The interaction potential and scattering rate reduce to

$$U_{dip} \simeq \frac{\hbar\Omega^2}{4\delta} \equiv \frac{\hbar\Gamma}{8}\frac{\Gamma}{\delta}\frac{I}{I_{sat}} \tag{2.8}$$

$$\Gamma_{scatt} \simeq \frac{\Gamma}{8}\frac{\Gamma^2}{\delta^2}\frac{I}{I_{sat}} \tag{2.9}$$

where $\delta = \omega - \omega_o$. As described earlier, and now shown explicitly, a positive detuning results in a decreasing potential from the region of highest intensity, while a negative detuning results in a trapping potential. It is important to note that at such large frequency detunings, the scattering rate has a I/δ^2 dependence while the trap depth is proportional to I/δ. This means that it is possible to create a trap that is sufficiently deep to confine atoms while keeping the scattering rate low to reduce spontaneous scattering; the result is a conservative potential for which the atom does not change its internal state.

2.3 Optical Molasses

An optical molasses is an arrangement of three orthogonal sets of counter-propagating light fields such that an atom within the intersection of the fields is subject to a reduction in velocity regardless its direction of movement. If we focus solely on the beams propagating in the $+x$ and $-x$ directions, the equation describing the scattering force (2.1) for an atom travelling opposite to the direction of the beam becomes

$$F_{+} = \hbar \mathbf{k} \frac{\gamma}{2} \left(\frac{I/I_{sat}}{1 + I/I_{sat} + \left(\delta_o + kv\right)^2 / \Gamma^2} \right) \tag{2.10}$$

for a beam propagating in the same direction as the atom, where $\delta_o = \omega - \omega_o$, and

$$F_{-} = -\hbar \mathbf{k} \frac{\gamma}{2} \left(\frac{I/I_{sat}}{1 + I/I_{sat} + \left(\delta_o - kv\right)^2 / \Gamma^2} \right) \tag{2.11}$$

An atom at rest will have no net force acting on it, as the two beams (assuming identical frequencies and intensities) will cancel. However, if the atom is moving with some velocity $\mathbf{v}$ then the forces will no longer balance. Further, if the velocity of the atom is such that $|kv| \ll \Gamma$ and $|kv| \ll |\delta_o|$, then the total force acting on the atom is approximated by [12]

$$F_{molasses} = 4\hbar k^2 \frac{I}{I_o} \frac{2\delta \Gamma v}{\left[1 + \left(2\delta/\Gamma\right)^2\right]^2} \tag{2.12}$$

where terms of order $(kv/\Gamma)^4$ and higher have been neglected. If the detuning δ_o is less than zero, then the force will oppose the velocity of the atom. This results in a damping force on the atom similar to the force on a particle in a viscous fluid. This similarity is what originally led to the appellation of the 'Optical Molasses Technique' [13].

2.4 MOT

An optical molasses will cool atoms; however, the atoms are free to exit from the region where the cooling beams intersect. Removed from this region, the atoms are no longer accessible to the laser light until they once again reenter the beam path by way of diffusion. In order to trap the beams within the cooling region, an inhomogeneous magnetic field is applied in such a way as to combine with the light beams to produce spatial confinement by way of a position dependent radiation pressure. This arrangement is known descriptively as a magneto-optical trap (MOT) and was first demonstrated in three dimensions in 1987 Raab et al. [14].

A magnetic field with a constant gradient is overlaid with the counter propagating, circularly polarized cooling beams described in the optical molasses section. The magnetic field is produced by way of two magnetic coils in an anti-Helmholtz configuration (the direction of current flow in one coil is opposite that of the other coil), such that there exists a zero field at the intersection of the cooling beams with a

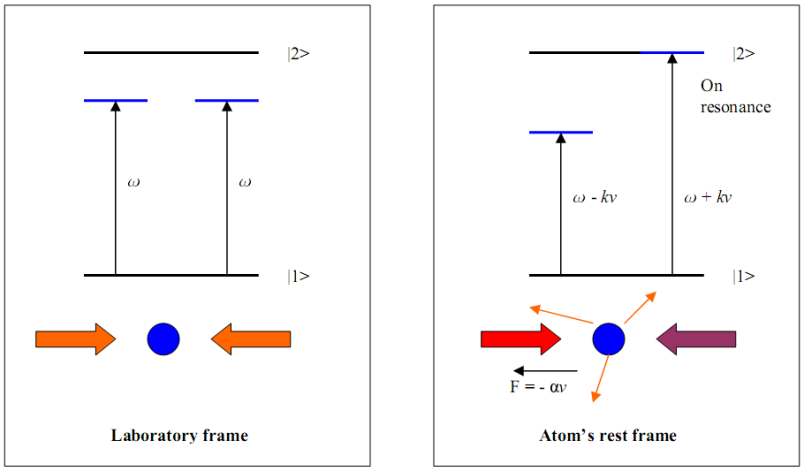

Figure 2.3: Counter-propagating laser fields red detuned from an atomic transition. **Left** An atom at rest does not absorb photons from either beam; **Right** An atom with velocity v will preferentially absorb photons from the beam Doppler shifted to resonance.

radially increasing, linear magnetic field away from the center. In this configuration, the Zeeman shift of the electronic levels of the atom are dependent on the position of the atom within the trap.

In order to understand the mechanism underlying this trapping scheme, a two-level atom travelling in the $+x$ direction with a $J = 0 \longrightarrow J = 1$ transition is considered. The Zeeman shifts of the electronic levels due an applied magnetic field $B(z)$ are

$$\Delta w_B = \frac{\mu_B}{\hbar} \cdot \frac{dB}{dx} \cdot x \tag{2.13}$$

where μ_B is the Bohr magneton. This atom is also in the presence of two counter-propagating laser beams along the $\pm x$ directions with the same circular polarizations. The direction of the beam propagation with respect to the magnetic field is what drives the σ^- transition of an atom moving in the $+x$ direction, and the σ^+ of an atom moving in the $-x$ direction. Incorporating both the force due to the Doppler shift, as well as the force due to the Zeeman shift gives

$$F_- = -\frac{\hbar k}{2}\Gamma \frac{I/I_{sat}}{4\left(\delta_o + kv + \frac{\mu_B}{\hbar} \cdot \frac{dB}{dx} \cdot x\right)^2 + I/I_{sat} + 1} \tag{2.14}$$

The reverse is true for an atom propagating in the $-x$ axis.

$$F_+ = \frac{\hbar k}{2}\Gamma \frac{I/I_{sat}}{4\left(\delta_o - kv - \frac{\mu_B}{\hbar} \cdot \frac{dB}{dx} \cdot x\right)^2 + I/I_{sat} + 1} \tag{2.15}$$

For small velocities and displacements, the total restoring force acting on an atom can be given by

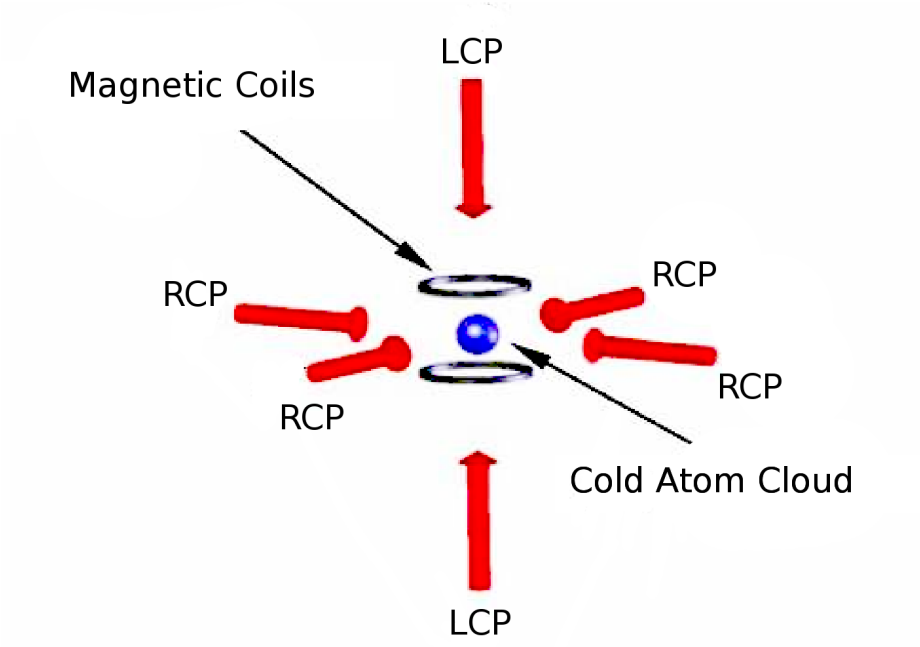

Figure 2.4: Schematic diagram showing the polarizations and directions of the cooling light in a magnetic trap.

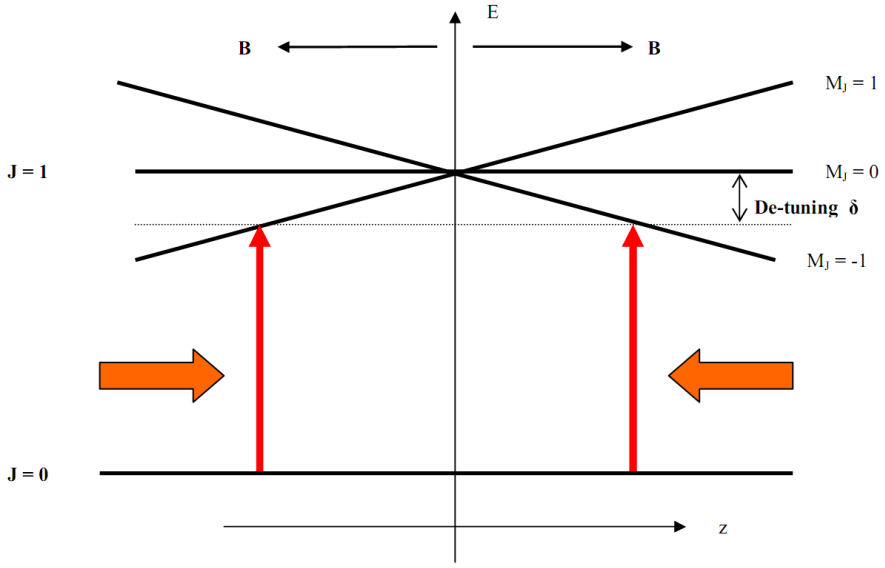

Figure 2.5: Diagram showing the hyperfine splitting of the excited atomic state in the presence of a linearly varying magnetic field in one-dimension. This splitting is the origin of the position dependent force in a magneto-optic trap.

$$F_{MOT} = -\alpha v - Kx \tag{2.16}$$

where α is the damping constant, corresponding to the frictional force responsible for the optical molasses, and K is the spring constant of the damped harmonic oscillator, resulting in a position dependent restoring force to the zero of the magnetic field. This one-dimension derivation can be expanded to include all three Cartesian axes, although in three dimensions there is required further discussion of the exact nature of the cooling and loss mechanisms responsible for the bounds on the ensemble temperature and number.

2.5 Magnetic Trap

A MOT is essential for the initial cooling and trapping of free atoms, but it is not always the most convenient environment for probing an ultracold atomic gas due to the constant variation in the internal state of the atoms.

A magnetic dipole μ in the presence of a magnetic field has potential energy

$$V = -\mu \cdot B \tag{2.17}$$

for an atom in a state $|IJFm_F\rangle$ the Zeeman energy is given by

$$V = g_F \mu_B m_F B \tag{2.18}$$

This result is the basis for magnetic trapping. The potential of the atom is only dependent on the magnitude of the field at any given position, and not on the direction. The reason is that as the atom moves throughout the trapping region, the atomic dipole adiabatically rotates to maintain an alignment with the magnetic field. From this, the force on the atom is simply

$$F = -g_F \mu_B m_F \nabla B \tag{2.19}$$

The spin dependence of the force means that, depending on the sign of g_F, a positive spin state will experience a trapping potential, while a negative spin state will be expelled from the trapping region and lost to the ensemble. For an initial MOT of $F = 1/2$ atoms with equally populated hyperfine states, this results in an initial loss of approximately 50% in the atom number.

The field for the magnetic trap can be created by the same coils used to produce the magnetic field in the MOT. The MOT coils are implemented in an anti-Helmholtz configuration, producing a quadrupole magnetic field. This field has the disadvantage of producing a vanishing field at the center of the trap. In this region, the energy spacing of the atomic hyperfine states is negligible (the spacing being of order $\mu_B B$) and a pronounced mixing of the magnetic quantum states occur. This results in an appreciable transfer of atoms from the trapped $m_F > 0$ states to the untrapped $m_F < 0$ states. Atoms transferred in this way are quickly expelled from the trap. There are various methods available to compensate for this loss mechanism. It is possible to lift the average potential of the trap center by applying an oscillating

bias field to the system. Known as a TOP trap, this method was used in the first successful Bose-Einstein condensation experiments. It is also possible to expel atoms from the center of the trap using an applied laser field.

Magnetic trapping is used to increase the density of the laser cooled atoms in order to achieve high collision rates necessary for efficient evaporative cooling [15].

2.6 Cooling Mechanisms

The Doppler cooling method is the most important in the preparation of cold, trapped atoms from a hot atomic source [16]. Although there is a theoretical lower bound on the temperature attainable using this technique, further cooling mechanisms are available that remove this limitation The Doppler cooling limit, as well as the supplementary cooling techniques used within our experiment will be discussed.

2.6.1 Doppler Cooling limit

The force on an atom from a single laser beam can be written as

$$\mathbf{F} = \mathbf{F}_{abs} + \delta\mathbf{F}_{abs} + \mathbf{F}_{spont} + \delta\mathbf{F}_{spont} \tag{2.20}$$

Clearly, the scattering force corresponds to the average force from the absorption of a photon, and the net force from spontaneous emission must average to zero due to symmetry considerations. What must be considered is the effect of the small fluctuations $\delta\mathbf{F}_{spont}$ and $\delta\mathbf{F}_{abs}$ on the internal energy of the atom.

Each emission event alters the state of the atom by some recoil velocity $v_r = \frac{\hbar\mathbf{k}}{m}$, where $\mathbf{k}$ is the wave-vector of the photon emitted. Similar to the Brownian motion of pollen in a liquid, the atom undergoes a random walk in its velocity due to the random nature of the emission process. After N emission events, the mean displacement in velocity space is proportional to $\sqrt{N}$[12]. During a time t the average emission events is

$$N = \Gamma_{scatt} t \tag{2.21}$$

and the mean-square of the velocity in one of the three Cartesian coordinates will increase as

$$\overline{v^2}_{spont} = \eta v_r^2 \Gamma_{scatt} t \tag{2.22}$$

The factor $\eta = \langle \cos^2\theta \rangle$ is the angular average. For a completely isotropic emission pattern $\eta = 1/3$.

Absorption events due not occur uniformly in time. Since each absorption event is followed by spontaneous emission, the mean number of photons absorbed in time t is also given by (2.21). However, if it is assumed that the events follow a Poisson distribution, then there will exist a one-dimensional random walk in the velocity along the laser beam in conjunction with the change in velocity due to the mean force. Since all the photons have a common $\mathbf{k}$ vector, the factor η is unity.

$$\overline{v^2}_{abs} = v_r^2 \Gamma_{scatt} t \tag{2.23}$$

Now, employing Newton's second law it is possible to rewrite (2.20) in terms of the average velocities of the individual mechanisms

$$\frac{d}{dt}\left(\frac{1}{2}m\overline{v^2}\right) = \frac{d}{dt}\frac{1}{2}m\left(\overline{v^2}_{abs} + \overline{v^2}_{spont} + \overline{v^2}_{scatt}\right) \tag{2.24}$$

Incorporating (2.22) and (2.23) gives

$$\frac{d}{dt}\left(\frac{1}{2}m\overline{v^2}\right) = \frac{1}{2}m\left(v_r^2\Gamma_{scatt} + \eta v_r^2\Gamma_{scatt} + 2\overline{v}_{scatt}\frac{d}{dt}\overline{v}\right) \tag{2.25}$$

and the addition of a counterpropagating beam gives

$$\frac{d}{dt}\left(\frac{1}{2}m\overline{v^2}\right) = mv_r^2(1+\eta)\Gamma_{scatt} + \overline{v}F_{molasses} \tag{2.26}$$

This describes the balance between the contributions of the optical molasses towards cooling, and the contributions of the fluctuations towards heating. Assuming that the light fields are symmetric (this isotropy gives the value of η as one) and that the intensities are far from saturation (allowing for the assumption that the scattering rate of the atom is six times as the rate for a single beam), the extension to a three dimensional optical molasses results in

$$\frac{d}{dt}\left(\frac{1}{2}m\overline{v^2}\right) = 2mv_r^2\Gamma_{scatt} + \alpha\overline{v}^2 \tag{2.27}$$

In the cooling limit, the net force on the atom must be zero. The equilibrium state for each of the three axes is then given by

$$\overline{v}^2 = 2mv_r^2\frac{\Gamma_{scatt}}{\alpha} \tag{2.28}$$

According to the equipartition theorem, the kinetic energy of the atom is related to the temperature by

$$\frac{1}{2}m\overline{v^2} = \frac{1}{2}k_BT \tag{2.29}$$

Using the above relation, as well as the previously derived values for α and Γ_{scatt}, allows for an expression for the temperature to be written

$$k_BT = \frac{\hbar\Gamma}{4}\frac{1+(2\delta/\Gamma)^2}{(-2\delta/\Gamma)} \tag{2.30}$$

It is straightforward to show that the minimum temperature occurs for a detuning of half the natural linewidth to the red ($\delta = -\Gamma/2$).

$$k_BT_D = \frac{\hbar\Gamma}{2} \tag{2.31}$$

This result is the lowest temperature achievable in an optical molasses with a two-level atom and is referred to as the **Doppler cooling limit**[17]. For comparison, the Doppler limit for a Lithium ensemble is approximately $140\mu K$[18] , and $146\mu K$ for Rubidium [19] .

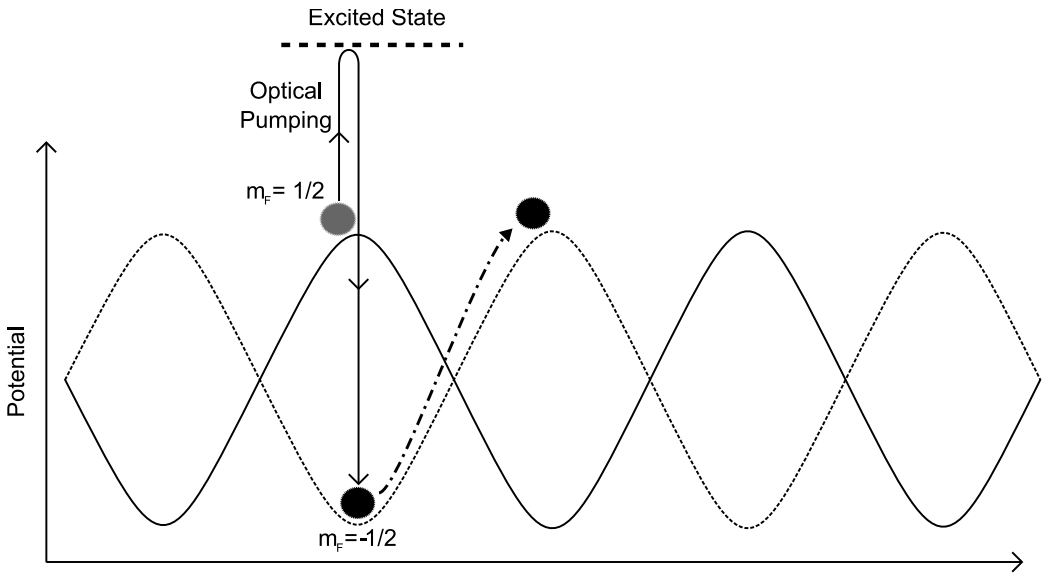

Figure 2.6: Schematic diagram demonstrating the method of gradient cooling. As the atom reaches the peak potential, it is driven to the lower energy state by optical pumping. The energy difference is released as a spontaneously emitted photon.

2.6.2 Sub-Doppler Cooling

This lower limit was assumed valid until experimental results demonstrated cold atomic gases with temperatures far below what should be achievable by laser cooling [20]. Throughout the above derivation, the atom was modelled as a non-degenerate two-level system in the presence of a homogeneous radiation field. These two assumptions proved invalid; the counter-propagating beams produce an inhomogeneous field, and, when the Earth's magnetic field has been compensated for, atomic states are degenerate.

Sisyphus Cooling and the Recoil Limit

These deviations from the predicted model turned out to have beneficial effects for cooling atoms [21]. Counter-propagating light fields with orthogonal polarizations will produce a total field whose polarization varies sinusoidally in space. Since the coupling of the ground state magnetic sublevels to the excited state are dependent on the polarization of the light field, an atom moving in space will experience a periodic potential that is dependent on its internal m_F state.

An atom with sufficient kinetic energy will climb the potential hill. In the absence of any other processes it would then proceed to descend to a trough, converting the gained potential energy back into kinetic energy. However, at the top of the potential hill the atom is optically pumped to a magnetic sublevel that has a potential trough at that position. The excess energy is carried by the spontaneously emitted photon. The atom then continues to climb the next potential hill, where the process is repeated until the atom no longer has sufficient energy to reach the potential maxima.

The temperature limit for this process is the recoil limit, given by

$$k_B T_R = \frac{\hbar^2 k^2}{2M} \tag{2.32}$$

where M is the atomic mass. This absolute lower limit for photon assisted cooling is based on the residual momentum transfer to the atom from the final spontaneous emission event. Exotic cooling schemes have been shown capable of bypassing this limit[22][23].

Evaporative Cooling

As described previously, laser cooling by optical molasses produces atomic gas ensembles with mean temperatures below the Doppler cooling limit but still far above the recoil limit. One method of further reducing the temperature of the atom cloud, albeit at the expense of the atomic number, is by exploiting the magnetic trapping technique[24].

As the name suggests, the mean temperature of the system can be reduced by allowing the hottest atoms to leave the trap. An apt analogy is to compare the atoms in the magnetic trap to the water molecules in a hot cup of coffee. As the most energetic molecules escape the system as steam, the remaining molecules in the coffee rethermalize to a lower temperature.

If the distribution of energies of the atoms in the magnetic trap is given as a Boltzmann distribution;

$$N(E) = N_o \exp[-E/k_B T_I] \tag{2.33}$$

where N_o is the total number of atoms in the trap, and T_I is the initial temperature. The key aspect of the technique is to apply some cut to the system that preferentially removes those atoms whose energy is above a specific threshold

$$E_{cut} = \eta k_B T_I \tag{2.34}$$

where the variable η determines the magnitude of the cut. The elastic collision rate $\Gamma_{el} = \bar{n}\sigma v$, where $\bar{n}$ is the average density of the trap, σ is the elastic scattering cross section, and v is the average velocity, determines how quickly the remaining atoms rethermalize to a new temperature $T_{new} < T_I$. The collision rate depends on the atom number through the mean density term, and to the temperature through the velocity term, so that $\Gamma_{el} \propto N/T$. It is critical that the temperature of the ensemble decrease at a rate proportional to the decrease in atom number in order that efficient rethermalization occurs. The removal of high energy atoms can be applied repeatedly after rethermalization as a means of continuously reducing the mean temperature of the system.

The energy cut can be applied in various ways. The simplest method is to reduce the trap depth of the magnetic field[25]. In this way, atoms with high energies are able to overcome the potential barrier and exit the system. Although shown effective with both Rb and Cs [7], this method suffers from a drastic reduction in trap density and the inability to support the atomic cloud against gravity. Atoms may also be preferentially removed through the use of well-defined radio frequency (RF) radiation

to couple transitions between the trapped and untrapped spin states[26]. Since the separation between the $m_F = \pm 1$ states is dependent on the position of the atom within the magnetic trap, an applied RF field (ω_{RF}) will drive transitions for hot atoms whose oscillations extend beyond a radius r_{cut} from the trap center.

Sympathetic Cooling

Evaporative cooling is not possible with spin-polarized fermionic atoms as s-wave scattering is forbidden, due to the necessary antisymmetry of the wavefunction, and p-wave scattering is extremely small at low temperatures. Sympathetic cooling works by mixing the fermionic atoms with another species, allowing the s-wave collisions necessary for evaporative cooling. In our system, fermionic ^6Li atoms are to be mixed with bosonic Rb atoms. The Rb atoms can then be evaporatively cooled using an RF knife, in turn cooling the ^6Li atoms.

Chapter 3

Ultra-Cold Molecules

Ultimately this experiment is concerned with the study of ultracold molecules in the quantum regime. Molecules, by nature of their increased complexity, can be used to study physical effects that are not present within an atomic ensemble. The availability of cold molecules below 1K has direct application in the areas of ultracold chemistry[27], precision measurements[28], molecular interferometry[29], and quantum computing [9].

Unfortunately, the very complexities that make studying ultracold molecules interesting are also what make them difficult to realize experimentally. The techniques described previously for cooling and trapping atoms are not viable for use with molecules. Laser cooling of atoms exploits the resonant coupling of energy states where both the excitation and decay transitions are well defined and subsequently controllable. Molecules have both vibrational and rotational energy levels; the allowed optical transitions are plentiful and closely packed. There is no closed level scheme by which hot molecules can be cooled using laser light.

3.1 Methods of Production

There exist multiple methods for producing cold molecules, these are conveniently divided into the categories of either 'direct' or 'indirect'. Direct methods begin with relatively hot molecules, and through a combination of slowing, cooling, and trapping are able to produce a cloud of cold molecular gas. Two of the more established techniques are Buffer-Gas Cooling and Stark-deceleration.

Buffer-Gas Cooling A Helium buffer gas is used to cool molecules by way of elastic collisions. The temperature is limited by the equilibrium vapour pressure of the buffer gas, typically this is a few hundred millikelvin [30]. Aside from the temperature, the main issue with this method is coupling molecules into the cryogenic He buffer gas. There have been various methods both proposed and implemented, each with advantages and drawbacks. This technique was experimentally realized by the Doyle group in 1997[31].

Stark-Deceleration Time-dependent, inhomogeneous fields are produced by an array of field stages. These fields alter the velocity of the molecules by repetitively modifying the Stark potential energy. From conservation principles, an increase of the Stark potential energy must come at the expense of the kinetic energy of the molecule. An added provision of this technique is the ability to select the internal energy state of the molecule. Although this method was first proposed in the 1950's,

its implementation was only realized in 1999 by Meijer's group[32].

Indirect methods rely on an ensemble of ultracold atoms as the basis for generating ultracold molecules. These methods, as will be described in detail later on, rely on the coupling of free atomic states to bound molecular states through either optical or magnetic means. These techniques have proven extremely fruitful in obtaining molecule ensembles with translational temperatures in the μK regime[33].

3.2 Molecules from Cold Atoms

The formation of ultracold molecules from cold atoms was primarily spurred by the advent of Bose-Einstein condensation experiments. As the accessibility to cold atoms became more prevalent, and the experimental difficulties overcome, the study of molecular spectroscopy and Feshbach resonances led to developments in generating ultracold molecules from cold atom sources.

The binding mechanism in a molecule is derived from the shared electron cloud. Approaching atoms are subject to an attractive force at long interatomic distances. However, this force becomes repulsive as the separation nears that of an atomic radius due to the overlap of the electronic orbitals. Cold atoms cannot form molecules during a binary collision for reasons of momentum and energy conservation. Thus, methods of coupling the free atom energy channel to that of a closed molecular state are essential in creating ultracold molecules.

3.2.1 Photoassociation

In 1987, Thorsheim et al.[34] proposed that the addition of a photon during the collision event, and of a suitable frequency, could drive the ground state atom pair into a bound electronically excited molecular state.

One-Photon Photoassociation

A single photon, resonant with a bound excited state of the molecule, will drive the transition from free atoms. However, the molecules formed in this manner are short lived and decay by spontaneous emission back into free atoms. Since the photon emitted is often red detuned with respect to the photoassociation light, the kinetic energy of the free atoms is larger than the depth of the trap and they are lost from the ensemble. Although this single photon method is not directly useful for creating cold molecules, it is vital as a means of mapping out the energy levels of the electronic excited state. Single-photon spectroscopy observes the fluorescence of the atom trap as a function of the frequency ω_{PA} of the photoassociation light. Scanning the photoassociation laser will result in trap loss as ω_{PA} passes through a transition of the free atom to bound molecule. The resolution is limited by the width of the statistical distribution of the initial kinetic energy of the colliding atoms and the natural linewidth of the photoassociation laser. At room temperature the resolution

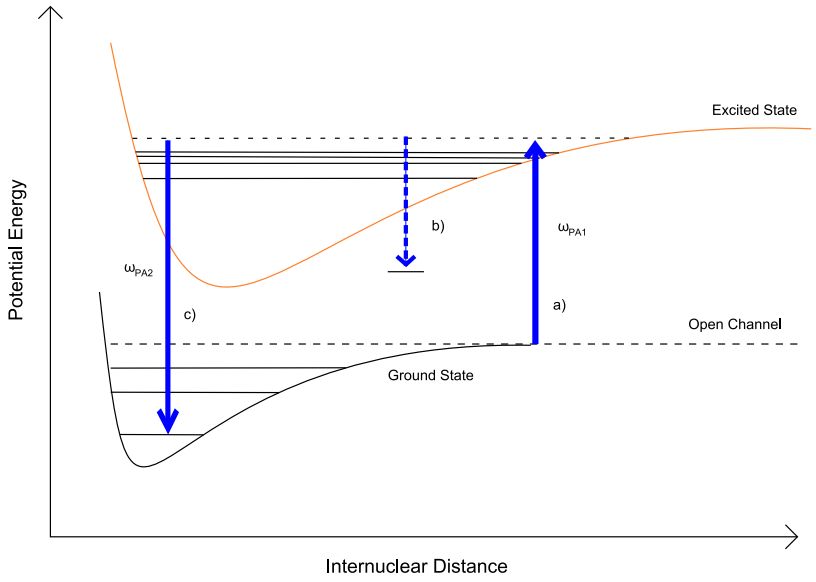

Figure 3.1: Photoassociation method for producing ultracold molecules. (a) A photon of sufficient energy couples with a free atom pair during a collision event, generating a bound excited state molecule. (b) The molecule quickly decays back into its constituent atoms. These atoms often gain kinetic energy during this process and exit the trap. (c) A second photon may drive the transition from the upper excited state to a lower ground state. Careful tuning of this second photon may allow for the production of vibrationally cold ground state molecules.

is extremely poor, but at temperatures nearing $100\mu K$, the width of the distribution approaches 2MHz. Photoassociation is dependent on coupling the atoms with a photon during a collision event. The probability of finding two atoms separated by a distance R scales as R^2, meaning that photoassociation is more efficient for long-range molecular states. The excited state potential of heteronuclear dimers (such as LiRb) has a $1/R^6$ dependence, whereas that of homonuclear dimers (such as Rb_2) scales as $1/R^3$. The photoassociation cross-section is therefore much larger than for homonuclear dimers.

Since the ability to couple the excited molecule to a ground state is highly dependent on the vibrational and rotational states of the excited molecule, one-photon spectroscopy is a vital step towards generating ultracold ground state molecules via two-photon processes[35].

Two-Photon Photoassociation

The addition of a second frequency ω_{PA2}, where $\omega_{PA2} > \omega_{PA1}$, allows for the resonant coupling of the excited molecule to a ground molecular state.

The ability of the second photon to coherently transfer population from the excited state of the molecule to a lower ground state is highly dependent on the overlap of the wavefunctions of each state. This is known as the Franck-Condon Principle, and is the main reason why it is essential to fully map the energy levels of the excited state prior to performing two photon photoassociation; only specific states of the

excited molecule will couple well with the ground vibrational and rotational state of the molecule. By carefully preparing the excited state molecules, and choosing the correct wavelength of the second photon, it should be possible to create ultracold molecules in the lowest bound energy state[36].

3.2.2 Feshbach Resonance

At ultra-cold temperatures, interatomic collisions are almost entirely s-wave in nature[37]. This is due to the low relative velocity of the atom pair, and the small interaction length. As a consequence, the relevant collision rates of an atomic ensemble are described completely by the s-wave scattering length a_o. For instance, the elastic scattering cross section for a pair of bosonic atoms in the ultracold limit is

$$\sigma = 8\pi a_o^2 \tag{3.1}$$

which further defines the time required for evaporative cooling in a magnetic trap. The s-wave scattering length is essential in the description of cold atomic gas behaviour; the thermalization rate, mean-field energy, and the stability of the ultracold atomic cloud are all dependent on this single parameter[38].

Feshbach resonances occur when a quasi-bound state of the system (such as a molecule) becomes degenerate with the collisional energy level of the open free atom channel. Suppose that at zero magnetic field, the closed channel of the excited molecular state is at a higher energy than that of the free atom channel. An asymmetry in the magnetic moments of the two state results in a shift of the relative energy. If the closed channel has a large, negative magnetic moment compared to the open channel, an increasing magnetic field will result in a decreasing energy difference between the states. This shift in the relative energies is known as 'Zeeman Tuning'. As these levels approach degeneracy, the production of molecules from free atoms can be induced by the coupling of the closed and open channel.

Feshbach resonances provide yet another means of both mapping the interatomic interaction potential and generating ultracold molecules from a cold atom source. Although homonuclear molecules have been well studied, there exists relatively little information on Feshbach resonances between two different atomic species. Observations of $^6Li-^{23}Na$ [39] and $^{40}K-^{87}Rb$ [40] systems have been made, but only very recently have the $^6Li-^{87}Rb$ resonances that are the focus of our experiment been observed[41] .

Pursuing heteronuclear Feshbach resonances, although experimentally and theoretically more complex than the homonuclear counterpart, gives access to a richer field of physics. Ultracold heteronuclear molecules provide access to studying Bose-Fermi mixtures with tunable interactions [42], and the possibility of ultracold polar molecules with extremely high phase-space densities[43].

3.2.3 Electric Field Induced Feshbach Resonances

It has been proposed that collisions between ultracold atoms may be further controlled by use of an external electric field[44]. The theoretical framework for this proposal

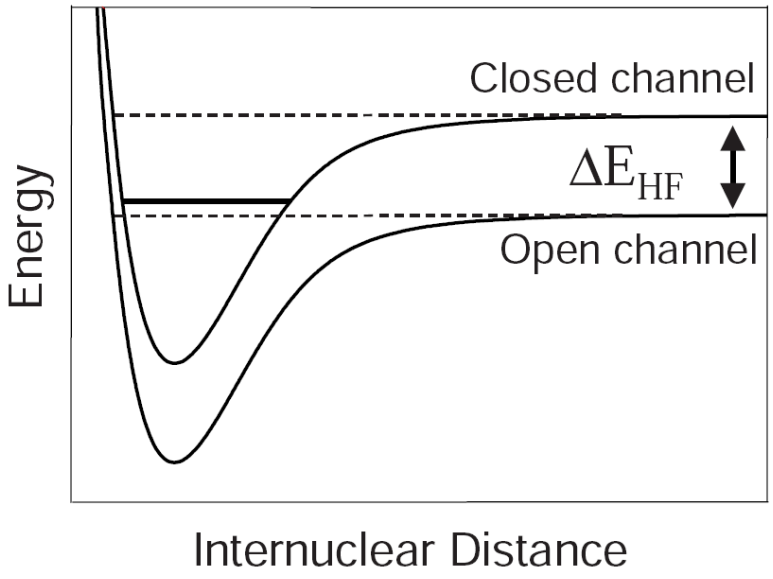

Figure 3.2: Increasing magnetic field strength drives the closed channel closer in energy to the open channel. A Feshbach resonance occurs for a magnetic field at which these two channels become degenerate.

is based on the instantaneous dipole moment formed during the collision of two atoms. Typical Feshbach resonances couple only the s-wave bound states of the free atoms, but it has been shown that strong DC electric fields may provide a method for coupling initial and final states of differing orbital momenta. This interaction between the dipole moment and the electric field is greatly enhanced near p-wave scattering resonances. It is further predicted that the electric-field couplings may shift the positions of existing Feshbach resonances while possibly inducing new s-wave magnetic resonances in the process.

Experimental Strategy There is progress towards implementing an experimental system to measure these predicted resonances. A pair of DC electrodes have been fabricated for use within the experimental system. The design was chosen so that the electrodes could be positioned within the volume of the trapping cell, close to the atomic cloud. Machined from 316 stainless steel, the electrodes are supported, and supplied current, by two extended, 1/4" copper feedthroughs. A *Macor*© screw is used to adjust the distance between the electrodes while maintaining electrical isolation. Currently, this distance is set to 1.3mm. A photo of the electrodes are shown in fig (3.3).

Since extremely high electric fields are required to probe these new resonances (in excess of 100kV/cm), it is important that the surfaces of the electrodes are as smooth and clean as possible to avoid arcing. After being machined, the electrodes were polished using successively higher grades of sandpaper, followed by an extensive buffing stage using a cloth and a commercial metal polisher. There was concern

that these polishing stages could embed contaminants into the electrodes that could hinder their functionality, and introduce unwanted materials into the vacuum system. Although this remains a concern, the polishing products were chosen to minimize these possibilities.

The electrodes were briefly tested in an extra vacuum chamber to check both the placement and the ability to handle high voltages. The voltage was systematically increased from 0 to 10kV without any sign of arcing or other defects in the build.As a final means of reducing the surface roughness, the electrodes will be sent out to a local company to be electropolished.

Figure 3.3: High DC voltage electrodes for use in the electric field induced Feshbach resonance experiment. The electrodes are attached to a 1.33" vacuum CF flange electrical feedthrough. Inserted into the vacuum chamber, the extended length will allow the electrodes to be placed physically close to the trapping region of the atomic gas. The spacing of the electrodes is approximately 1.3mm.

Once the electrodes are placed within the second generation experiment, they will be need to be 'burned in' during the vacuum pump out stage. This is accomplished by slowly increasing the applied voltage in an effort to further clean and smooth the surface of the electrodes. The small arcing events that occur due to imperfections in the electrodes have the advantage of destroying the imperfections in the process. An optical ammeter is in the process of being constructed that would allow for the detection of these micro-arcs, and allow for the 'cleaning' to be done in a controlled manner.

The electrodes cannot be placed directly at the position of the MOT, so a means of transporting the trapped atoms from the initial position to one centred within the 1.3mm spacing of the electrodes is required. The atoms will first need to be transferred to an optical dipole trap, with the beam of the dipole trap being subsequently repositioned using two galvos. This will need to be done in a manner that minimizes trap loss and avoids contaminating the surface of the electrodes. Once the trapped atoms are positioned, it should be possible to observe losses using absorption spectroscopy.

Chapter 4

Laser Light

Laser light is ubiquitous within this experiment. Cooling, trapping, and manipulating the atoms can all be accomplished through various combinations of wavelengths and intensities. For this reason there exist a wide range of lasers used within the experiment, each chosen for specific reasons based on the requirements of the system.

4.1 Requirements

The theoretical framework for laser cooling was based on the assumption of a well defined two level system, a single wavelength tuned near the transition resonance is enough to preferentially slow the atoms within the ensemble. In practice this simplified system is not realized; although we use alkali atoms with only a single electron in the outer shell, there exist multiple ground state energy levels for the electron to decay to. An atom whose electron is lost to the cooling transition is lost to the ensemble. Experimentally it is necessary to incorporate a mechanism that reintroduces the lost electron back to the cooling transition.

4.1.1 Lithium

^{6}Li has the advantage of being a spin-1/2 system. Theoretically this makes it a much cleaner and simpler model to work with as it is the alkali that most closely approximates the electronic structure of hydrogen. Unfortunately, these theoretical niceties come at the expense of experimental simplicity.

The small mass of lithium results in fine and hyperfine energy level splittings that are significantly smaller than those for other alkali atoms; specifically a hyperfine splitting of the ground state of 228MHz, and a splitting of the excited $2P_{3/2}$ state (4.4MHz) that is smaller than the natural line-width of the transition (6MHz)[45]. As such, Lithium is often approximated as a three level system with two ground states with a single excited state transition.

In this three level system, two frequencies of light are required for efficient cooling of Lithium atoms. The first is used to couple the $2S_{1/2}F = 3/2$ ground hyperfine state to the $2P_{3/2}$ manifold. This transition is known as the cycling or cooling transition due to the fast absorption and spontaneous emission rates. The second laser is necessary to reintroduce atoms that decay to the $2S_{1/2}F = 1/2$ state back to the cycling transition. The transition to the lower ground state occurs relatively quickly due to the narrow splitting of the excited state; light tuned near the cycling transition will drive transitions to all three excited levels. This requires that the repump light for Lithium be much more intense than that for Rubidium. Since the atoms scatter light

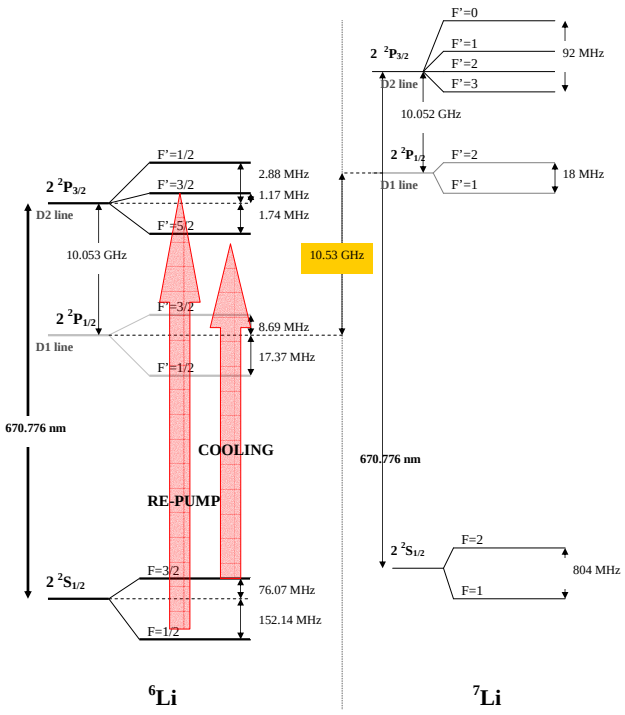

Figure 4.1: Energy level diagram of ^{6}Li with ^{7}Li shown for comparison. The cooling and repump light transitions are shown. [1]

nearly as often from the repump beams, they must be made to contribute to the laser cooling and so are integrated into the system along all six directions with the cooling light. Further, the unresolved nature of the excited hyperfine states severely limits the efficiency of sub-Doppler cooling. The polarization gradient is contingent on a well defined 'closed' transition that is not available for Lithium atoms.

An acousto-optic modulator, discussed further in the **Control System Hardware** section, can be used to induce a frequency shift of the master laser output in order to produce light for both the cooling and repump transitions.

4.1.2 Rubidium

Rubidium requires a separate master laser for both the cooling and repump light as the ground state hyperfine splittings are many gigahertz apart. Further, the excited state cannot be approximated as a single level as is the case for Lithium. The result is that the decay rate from the cooling transition is much lower; repump light of low power along a single direction of the MOT beams is sufficient for repopulation to the cooling states.

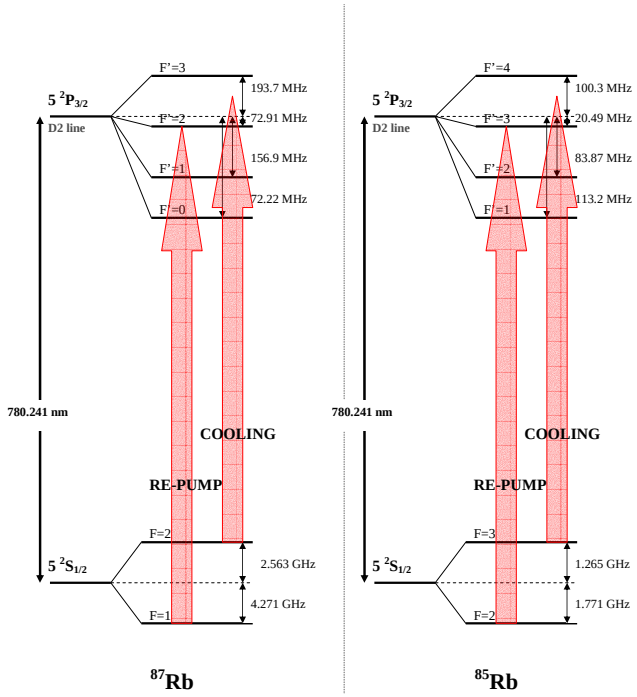

Figure 4.2: Energy level diagrams for ^{85}Rb and ^{87}Rb with the corresponding cooling and repump transitions shown.[1]

4.2 Master and Slave Lasers

There exist commercially available semiconductor lasers with natural output wavelengths close to the transition wavelengths of 780nm for ^{85,87}Rb and 671nm for ^{6}Li. These diode lasers produce light through the application of a forward bias current across a p-n junction, stimulating the recombination of electrons and holes[10].

Ultra-stable, well-collimated reference light is generated by locking the output of single 'master' laser to a specific energy transition of the atom by way of a saturated absorption spectroscopy technique[46]. This is a well established technique, described later, that provides a wide tunability with a narrow bandwidth. Amplification of this reference light is achieved through injection locking of further diode lasers.

In all, five master lasers are necessary for the experiment. Four are required for ^{85,87}Rb and one for ^{6}Li. The light from each of the Rubidium masters is sent to a slave laser for amplification. Most of the amplified light is then coupled into an optical fiber and sent to various experiments, with a small amount of light being reserved for diagnostic use by way of a Fabry-Perot interferometer. The interferometer is integral for verifying that the slave lasers are adequately locked to the appropriate frequency. The Lithium light is similar, except that the light is first frequency shifted using

an acousto-optical modulator such that the correct frequencies for the cooling and repump light (spaced 228MHz apart) are achieved. These distinct frequencies are then amplified and sent out to various experiments.

4.2.1 Master Locking Technique

Semiconductor diode lasers suffer from two major drawbacks; the output power of a single diode is a fraction of the total power needed for the experiment, and the natural linewidth of the emitted light spans hundreds of megahertz. Fortunately, the latter issue can be corrected through feedback mechanisms, while the former is compensated for through the introduction of an amplification system based on an injection scheme for diode lasers that remains extremely cost effective when compared with other laser systems[47].

The diode laser consists of a semiconductor gain medium enclosed within a resonator cavity. The short diode laser cavity is typically on the order of a millimetre with a low front facet reflectivity, and a broad frequency linewidth of the emitted light (100MHz). A diffraction grating, placed external to the diode cavity and driven by piezoactuators, is used to narrow and stabilize the output frequency of the laser[48]. The first order diffracted beam is reflected back into the laser cavity, This injected light results in a saturation of the gain medium and the extinction of all other competing frequencies. This is known as a Littrow configuration[49]. The frequency of the light is then controlled by changing both the angle of the diffraction grating, and the length of the resonator cavity by means of current and temperature. The frequency is narrow and stabilized only when the injected light couples resonantly into the diode cavity[50].

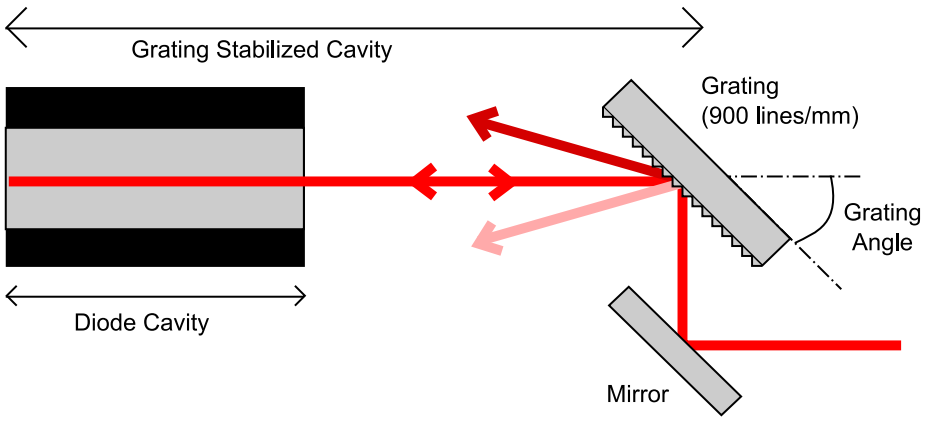

Figure 4.3: Schematic representation of the Littrow configuration used as a feedback mechanism for the master laser diodes. The grating and mirror are monolithic and move as a single entity in order to minimize the translation of the output beam as the grating angle and cavity are varied.

Saturated absorption spectroscopy is used to determine the exact location of the energy transition. From the output of the master laser, a fraction of the light picked off, split using a PBS, and sent as counterpropagating beams along the $\pm z$ axis of

either a Rubidium vapour cell or a Lithium heat pipe (the vapour pressure of Lithium does not allow for a room temperature vapour cell). Referred to as the pump and probe beams, they have identical frequencies ν_0 but opposite $\mathbf{k}$ vectors. The probe beam is detected on a photodiode; in the absence of any pump beam, the absorption signal will follow a frequency dependent Voigt profile due to the convolution of the natural Lorentzian line shape and the Maxwell-Boltzmann distribution of the atom velocities within the vapour cell. The addition of the higher intensity, counter propagating pump beam results in the appearance of sharp dips in the absorption profile at frequencies corresponding to resonances of the $v_z = 0$ atoms.

In order to generate an error signal for locking purposes, the light of the pump beam is frequency modulated by some small amount δv such that the new frequency is given by $v = v_o + \delta v \sin(\omega t)$. This is achieved with an acousto-optical modulator driven by a sinusoidally varying frequency signal from a direct digital synthesizer (DDS, described further within the QDG control system section). The intensity of the saturated absorption signal detected on the photodiode is dependent on the frequency of the pump and probe beams. The frequency modulated intensity of the photodiode signal, when expanded about the initial frequency ν_0, is given by

$$I(v) = I(v_o) + \frac{dI}{dv}|_{v_o}(\delta v \sin(\omega t)) + \frac{1}{2}\frac{d^2I}{dv^2}|_{v_o}(\delta v \sin(\omega t))^2 + O(\delta v)^3 \tag{4.1}$$

A home-built electronic 'lock-box' is used to produce a feedback signal[51]. The lock box consists of a lock-in amplifier and a PI controller. The modulated saturated absorption signal is multiplied with a sine wave of the modulation frequency (177.8kHz) and time averaged to extract the error signal ($\frac{\partial I}{\partial v}$). Adjusting the phase difference $\Delta\phi$ between the absorption signal and the reference frequency allows for the maximization of the output signal.

$$OutputAmplitude = \frac{1}{T}\int_0^T I(v,\omega)\cdot\sin(\omega t + \phi) \propto \frac{dI}{dv}|_{v_o}\delta v \tag{4.2}$$

The derivative of the absorption signal is used as the error signal for a feedback controller. The derivative of a saturation dip in the Voigt profile of the absorption signal is shown in fig (4.4). Locking to the zero crossing of this signal by use of a standard proportional-integral stage feedback loop allows for frequency stabilization of a few MHz. A slow correction output to the PZT voltage compensates for acoustic fluctuations of the grating position and for temperature drifts by adjusting the angle of the grating and the cavity length of the external laser cavity, while a fast correction output to the current controller compensates for small and fast fluctuations by adjusting the injection current to the diode.

4.2.2 Injection Locking of Slave Lasers

As discussed, the output from a single master laser is insufficient for the experiment. Light from the master laser is coupled into the gain medium of the slave laser diode. If the frequency of the master light is resonant with the internal cavity of the diode, then this frequency will saturate the gain medium and extinguish competing modes so that the slave laser output is pulled to a single, well-defined frequency at its natural

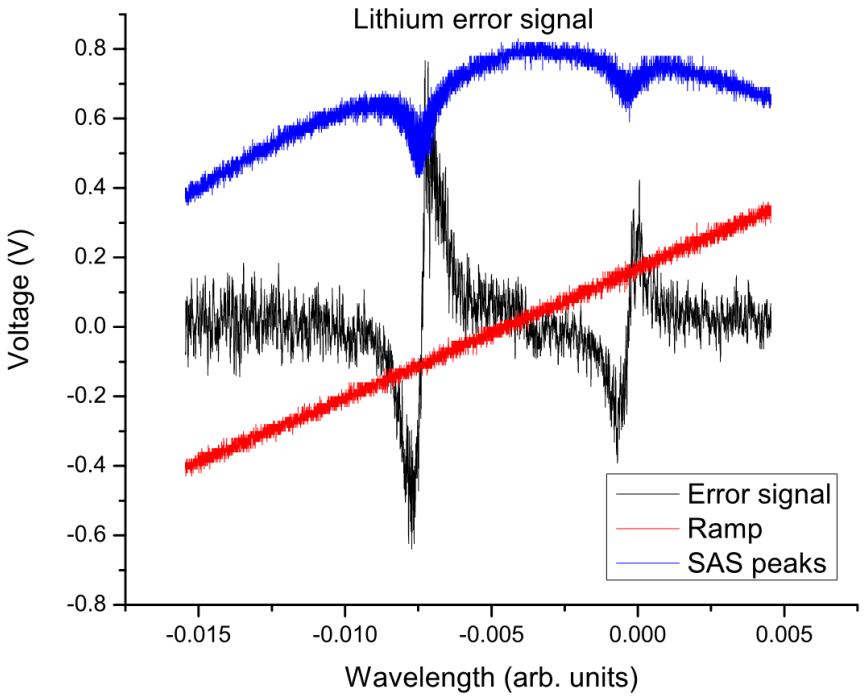

Figure 4.4: Sample error signal (shown in black) derived from the saturated absorption spectrum (shown in blue) for ^{6}Li. The laser frequency is locked to the zero crossing of the error signal.

output power. The master light is coupled into the output path of the slave laser through the side port of an optical isolator. The temperature and current of the slave laser are critical in ensuring that the master light is amplified. If these values are not set correctly, the output of the slave laser will not follow the injected master light.

4.3 Photoassociation Laser

The photoassociation laser is a Coherent Ti:Sapphire 899-21 pumped by a 10W Coherent Verdi laser. Since our interest is in the study of the molecular potentials corresponding to the asymptotic atomic states Li + Rb*, the laser will be scanned from a wavelength of 795nm, corresponding roughly to the D1 and D2 transitions of Rb*, and continuing further to the red.

The laser is locked to a frequency comb of a mode locked fiber. This should reduce the linewidth of the Ti:Sapphire laser to the kHz range. Scanning the wavelength of the laser is accomplished by tuning the repetition rate of the fiber comb.

The photoassociation light will be coupled into the trapping cell along the same optical axis as the dipole trap light. This is done due to space constraints, and to allow the greatest overlap between the trapped atoms and the photoassociation light.

4.4 Fiber Laser for Optical Dipole Trap

As discussed in the preceding theory section, atoms can be trapped by exploiting the interaction between an induced atomic dipole and a radiation field. A high intensity, strongly focused laser beam will have an attractive potential if the wavelength is tuned to the red of an atomic transition.

In order that the light is not resonant with any atomic transition, and in order that the scattering rate is as small as possible to avoid heating, it is advantageous that the wavelength should be detuned as far to the red as possible. Since the trap depth is inversely proportional to the detuning, a high intensity field is needed as compensation. Currently, a 20W fiber laser from IPG outputting a single-mode, linearly polarized beam at a wavelength of 1064nm is being used as the source for the dipole trap.

Theoretical calculations [2] show that the potential energy difference between the open channel and the first excited state of the LiRb molecule to be at 2182.1nm. It is therefore possible that the wavelength of the laser may result in the excitation of ground state molecules. The linewidth of such a transition, contingent on its existence, should be smaller than that of the bare atomic states (6MHz) due to the Franck-Condon overlap between the free and deeply bound states. Although this is a limiting factor, it could be overcome by simply tuning the narrow band trapping laser away from such a resonance.

An optical trap is based on the dipole force, described earlier, and is highly dependent on the intensity of the light. Since there does not exist a saturation intensity, as is the case for Doppler cooling, it is beneficial to increase the intensity of the light as much as possible. Initially, the dipole trap will consist of light from the 1064nm fiber laser focused to a $50\mu m$ waist close to the MOT. The light will be reflected back through the cell in order to increase the trap depth by way of an increased intensity. Future iterations of the dipole trap will use a stabilized resonator cavity to approach intensities of 120W.

4.5 Ionization Laser

An ionization laser is necessary to perform time of flight measurements of the molecular ions. Initially, an Nd:YAG Continuum Minilite, frequency doubled to 532nm, was to be used as the ionization laser within this experiment. The laser emits 5.6ns pulses at peak energies of 25mJ per pulse. The time of flight apparatus was developed and implemented by Nina Rauhut as part of her diplome work [2]. Although the apparatus has been successfully placed within the first generation experiment, it is currently inoperable due to technical reasons. The ionization laser was on loan from another research group, and recently needed to be returned. Possible replacements for this light source are being discussed, but as it is not currently required for the first generation experiment the final purchase will be delayed until later. Before the laser was returned, it was used to test the viability of laser ablation as a means of loading a Lithium MOT without the use of an emissive oven. These results of this test will be presented later within the **Measurements** chapter.

Chapter 5

Experimental Setup

A dual species Li and Rb MOT is necessary for the production of heteronuclear polar molecules. As was discovered, working with these laser cooled gases requires a wide range of expertise; including working knowledge of vacuum systems, atomic sources, and detection methods.

5.1 Vacuum System

Ensembles of cold atoms are delicate and can only be produced in an ultra high vacuum (UHV) environment. UHV is typically characterized by pressures below 10^{-9} torr.

Creating a UHV is a difficult prospect, creating one with the added restrictions placed on the system by the experiment requires careful planning and handling during all steps of the process. Nitrile gloves are worn when handling any of the vacuum system, the natural oils from a fingerprint are enough to keep the vacuum from reaching the necessary limit. The parts used must be composed of materials with very low vapour pressures — if even one component within the vacuum does not conform to this standard, then natural outgassing occurring from the materials may be too high to maintain a suitably low pressure within the vacuum chamber. Finally, any material at room temperature will naturally have organics, as well as air and water adsorbed to the surface. If left in this state, these components will slowly degas within the vacuum chamber and cause the background pressure to rise. To counter this, all parts are cleaned thoroughly in a series of ultrasonic baths consisting of a degreasing agent, clean water, methanol, and finally finished with acetone. The parts are assembled quickly to avoid recontamination, then heated to a temperature between 200 °C and 450 °C while the chamber is being pumped(certain parts, especially those with a glass to metal transition, cannot be heated as high as parts that are all metal. In general the assembly is heated to the highest temperature possible for all parts). This accelerates the outgassing of the materials and the degassing of the adsorbed air and water so that when the assembly is cooled a much lower pressure is attainable. This baking procedure can extend upwards of weeks, and can consist of multiple cycles in order to achieve the lowest possible background pressure.

5.1.1 Trapping Cell

The trapping cell is the most important part of the vacuum system. Our cell is composed entirely of highly polished, optical quality Borosilicate glass in order to allow for a greater range of optical access for the numerous light beams and detection devices. Purchased from OptoSigma, the cell is 9.5cm in length with an inner diameter

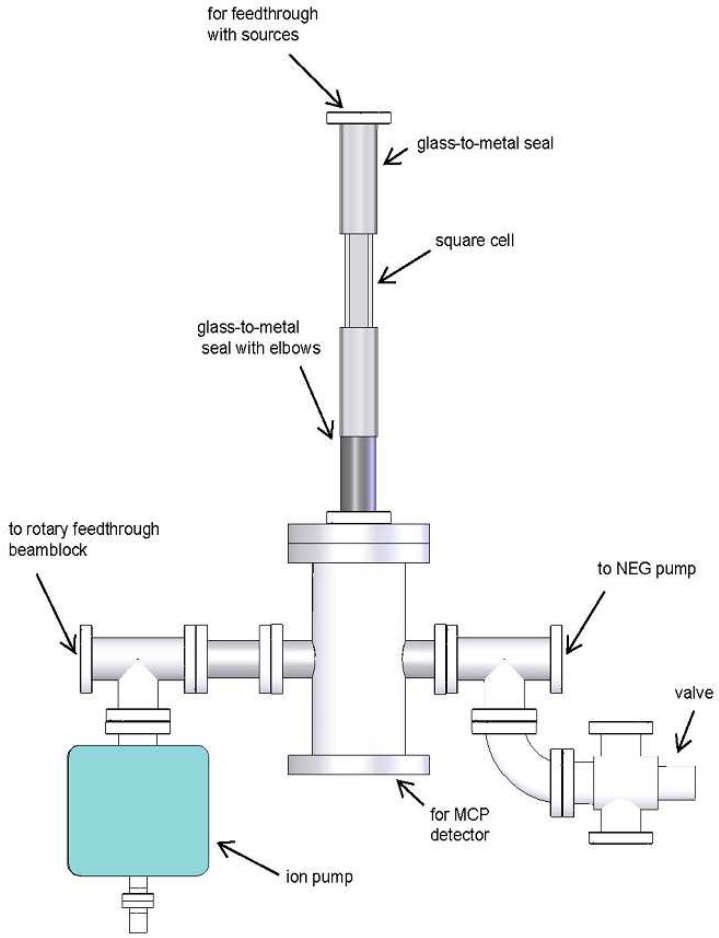

Figure 5.1: Simplified view of the vacuum system including positions of the ion and NEG pumps, as well as the glass trapping cell.

of 20mm and outer diameter of 30mm. It is adapted to the rest of the vacuum system by glass-to-metal seal purchased from MDC and Larson Electronics and further assembled by Ron Bihler at Technical Glass. The Lithium and Rubidium sources are attached to electrical feedthroughs mounted on one end of the cell, with the other end of the cell is connected to a four way cross. The cross supports both an ion and a non-evaporable getter pump with the time-of-flight (TOF) detector mounted parallel, and extending into, the trapping cell.

5.1.2 Vacuum Pumps

Ultimately, the ability to create an ultra high vacuum rests on how well one can remove the influx of gas into the system. Even the most well crafted vacuum systems are subject to a rise in background pressure if left unpumped. In general the equilibrium pressure of the vacuum system can be described by[52]

$$p = Q \times (S_p^{-1} + S_i^{-1}) \tag{5.1}$$

where Q represents the total influx of gas into the system from outgassing, degassing, leaks, and connections to other systems at a different pressures. S_p represents the speed of the pump in liters/second, and S_i represents the throughput of the connections between the vacuum system and the pump. Generally for atom trap experiments the volume of the vacuum is kept relatively small, typically less than 10 litres. With such small volumes, pumps designed for commercial applications (higher pressures but much larger volumes) are more than adequate in achieving UHV. The limiting factor in obtaining a really good UHV is almost entirely concentrated in maximizing the throughput of the connections between the pump and the vacuum.

Unfortunately, there does not exist a single pump capable of pumping efficiently over the entire range of pressures or the full range of elements required to obtain UHV[53]. For this reason it is necessary to use a combination of pumps, each one designed for use in a specific pressure regime and best suited to removing certain types of elements found within the vacuum. A turbo pump is used to quickly reduce the pressure from atmosphere to 10^{-4} torr, this pump is most useful during periods of baking and is removed by way of a bakeable valve when the vacuum system is mounted within the experiment. Lower pressures are achieved and maintained by a combination of an ion pump and a non-evaporable getter (NEG) pump. These pumps remain connected and active during the entire lifetime of the experiment.

Turbo Molecular Pump

Turbo molecular pumps were first introduced in 1957 [54] and work on the principle that particles can be accelerated in a specific direction using repeated collisions with a solid, moving surface. A high speed turbine rotor, whose blades have been angled in order to maximize the momentum transfer, is used to preferentially pump out gas molecules that collide with the blades. Used widely in industry and research for achieving moderately high vacuums, they are capable of pumping 70 litres/second with rotor speeds of 80,000 rev/min.

A Varian V70 turbo molecular pump was used in the bake-out of the vacuum chamber when large pumping speeds are integral in removing the high influx of degassed particles.

Ion Pump

Ion pumps become useful when the pressure drops below 10^{-5} torr and are used only after the turbo pump has reduced the background pressure to an acceptable level. Ion pumps consist of multiple anode cells with usually two cathodes. Ions are formed from the gas molecules present in the vacuum system by way of electrostatic discharge. The strong electric field of the discharge then accelerates the ionized particle toward the cathode where it is either buried directly, or reflected to be buried in another container. The magnet produces cyclotron motion of the free electrons, improving the ionization of the gas to be pumped. Further, the pump also works by binding reactive gases to a metal such as titanium. In both instances, particles are not removed from the system but instead are bound either chemically or physically so as to no longer contribute to the pressure of the system.

Due to the strong magnetic fields present, ion pumps must usually be placed at a distance from the main experiment. This constraint tends to reduce the throughput of the system. Ion pumps are also inefficient with respect to particles of low reactivity and many hydrocarbons. A Varian StarCell pump, capable of pumping at 20 litres/second, is used in our experiment.

Non-Evaporable Getter Pump

Non-evaporable getter pumps contain a highly reactive getter material that adsorbs active gas molecules through chemical reactions. The pump is activated by resistively heating the getter material, diffusing the passive surface layer into the bulk. Devoid of magnetic fields, or vibration inducing moving components, the pump can be placed arbitrarily close to the experimental chamber. Our experiment uses an SAES CapaciTorr pump using both a Ti-V alloy and a sintered Zr-V-Fe alloy as the reactive getter material. NEG pumps are very efficient in removing water and hydrogen, two major contaminants in vacuum systems.

5.2 Atomic Sources

5.2.1 Rubidium

Rubidium is selectively released using a commercial SAES Getters dispenser containing Rb_2CrO_4 and ZrAl in a stainless steel container. The ZrAl acts as a reducing agent and is responsible for not only returning the Rubidium alloy to its pure metallic state, but also for absorbing chemically reactive gases present in the dispenser. Passing a current through the dispenser results in the emission of atomic ^{85}Rb and ^{87}Rb vapour at their natural abundances of 72.17% and 27.83%.

5.2.2 Lithium

Lithium isotopes exist naturally in both fermionic (^{6}Li) and bosonic (^{7}Li) forms. For the purpose of this experiment, only the fermionic form is of interest; the bosonic form is essentially an unwanted impurity. This presented two major obstacles; the natural abundance of ^{6}Li is only 7.5%, and the low vapour pressure of lithium at room temperature meant that building a dispenser was not a viable option. The first issue was resolved by using an enriched source of ^{6}Li (95%), reducing greatly the contamination from ^{7}Li. The second issue necessitated building an effusive atomic beam source. The source consisted of an 80mm^3 reservoir machined from NiCr with a small exit hole. Resistive heating of a small ^{6}Li enriched crystal resulted in evaporation; the small exit hole of the oven confined the output to a collimated atomic beam source.

Typically an atomic source of this nature is implemented with a Zeeman slower in order to access a much larger section of the velocity distribution of the atoms[55]. Technical complexity and space considerations led to discussions concerning the benefits of a slowing system for use within our experiment. Naturally, eliminating any

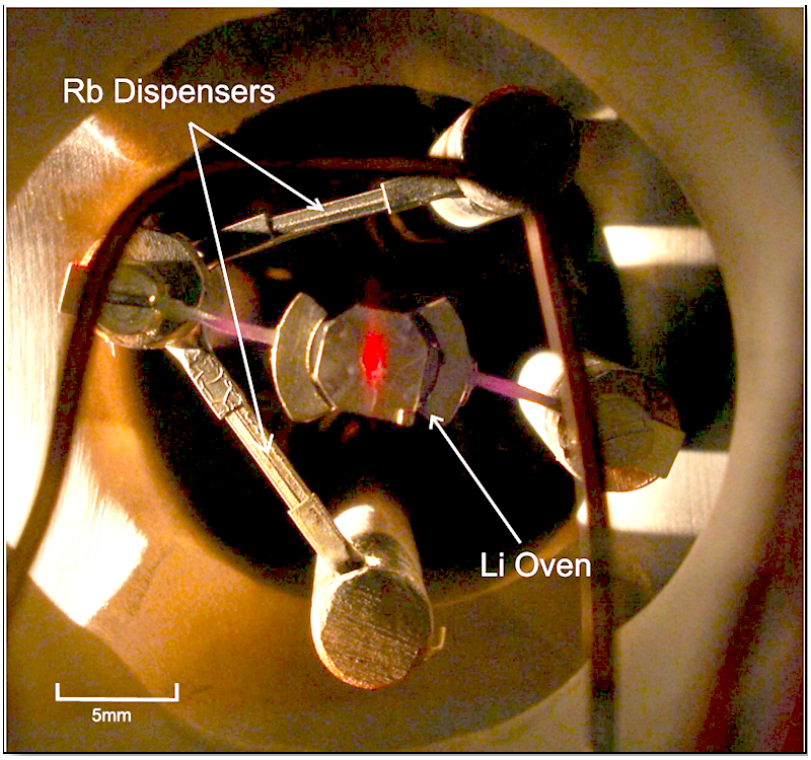

Figure 5.2: Direct view of the atomic sources used within the experiment. Attached to a UHV feedthrough, the Rb atoms are dispensed by way of a temperature dependent chemical reaction while the Li atoms are emitted from the effusive oven as the metal is heated above its melting point.

slowing mechanisms means that the number of atoms that our cooling light will have access to will be severely limited. However, this is compensated for slightly by being able to move the Lithium oven much closer to the position of the MOT, and by reducing the total volume of the vacuum system. The first increases the number of atoms that reach the trapping region, while the second allows for a smaller background pressure. A simple mechanical beam block is used to shelter the trapping region from being directly bombarded by hot Lithium atoms. Since we are mainly concerned with loading the cooled atoms into an optical dipole trap, where 10^5 atoms are sufficient for our experiments, we don't require large atom numbers in the MOT to begin with. For a more complete analysis of the motivation behind this method see S. Singh's Master's Thesis[1]. Initial measurements of the Li MOT are presented within the **Measurements** section.

5.3 Helmholtz and Compensation Coils

Magnetic fields are required for numerous aspects of the experiment. They are required to compensate for the earth's magnetic field, for use in a magneto-optical trap, for use in a pure magnetic trap, and, finally, for creating Feshbach resonance fields.

5.3.1 Compensation Coils

The compensation system consists of three pairs of coils in an anti-Helmholtz configuration. Each coil is composed of eighty windings of Kapton coated copper wires. They are placed so that each pair is perpendicular to one of the axes of the MOT light. The current through each coil is independent of the others; full control of the zero of the field is possible. These coils are used primarily to offset the earth's magnetic field, but can also be used to change the position of the MOT within the trap cell.

5.3.2 Helmholtz Coils

The Helmholtz coils are used to produce fields for everything else. Two identical coils are placed in the z-axis and are separated by a distance equal to the radius of the coils. Current can either be sent through the coils in the same direction, or in opposite directs. For current travelling in the same direction, the magnetic field produced is spatially uniform in a cylindrical region extending between the center of the coils. The field produced is calculated to be [56]

$$B_z = \mu_o I \frac{R^2}{\left(D^2+R^2\right)^{3/2}} + \mu_o I \frac{3R^2\left(4D^2-R^2\right)}{2\left(D^2+R^2\right)^{7/2}}\left(z^2-\rho^2/2\right)+... \tag{5.2}$$

$$B_\rho = \mu_o I \frac{3R^2\left(4D^2-R^2\right)}{2\left(D^2+R^2\right)^{7/2}} z\rho + ... \tag{5.3}$$

where z is the position along the axis, B_z is the magnetic field component along that axis, ρ the radial position, B_ρ the radial field component, μ_o the permeability constant, I the current, R the radius of the loop, and $2D$ the separation. For a Helmholtz configuration, where $R = 2D$, the fields reduce to

$$B_z = \mu_o I \frac{8}{5\sqrt{5}R} + ... \tag{5.4}$$

$$B_\rho = 0 + ... \tag{5.5}$$

From this it can be seen that the radial component is zero, while the component along the z-axis is uniform. This configuration is used for creating the large, uniform magnetic fields necessary for Feshbach resonance studies.

For currents running in opposite directions, the fields are given by

$$B_z = 3\mu_o I \frac{DR^2}{\left(D^2+R^2\right)^{5/2}} z + \frac{15}{24}\mu_o I \frac{R^2\left(4D^2-3R^2\right)}{\left(D^2+R^2\right)^{9/2}}\left(4z^3-6\rho^2 z\right)+... \tag{5.6}$$

$$B_\rho = -\frac{3}{2}\mu_o I \frac{DR^2}{\left(D^2+R^2\right)^{5/2}} \rho + \frac{15}{16}\mu_o I \frac{R^2\left(4D^2-3R^2\right)}{\left(D^2+R^2\right)^{9/2}}\left(\rho^3-4\rho z^2\right)+... \tag{5.7}$$

In this case, the third order terms do not vanish for $R = 2D$ as in the Helmholtz configuration. Instead, to first order, the gradient fields are maximized

$$\frac{dB_z}{dz} = \mu_o I \frac{48}{25\sqrt{5}R^2} = 2\frac{dB_\rho}{d\rho} \tag{5.8}$$

This is important for use as the magnetic field for a MOT. The anti-Helmholtz configuration gives a linear (to first order) field in both ρ and z with a maximized gradient.

Each coil, constructed by Paul Lebel [57], consists of approximately 250 windings of Kapton coated copper wire housed in a watertight PVC chamber. The contribution from these loops, for a maximum current of 25A, is predicted to be near 1kG. These coils are water cooled as the power dissipation when run at maximum field gradients is close to 1kW.

A coil driver, constructed by the UBC electronics lab, is used to toggle the coils between a Helmholtz or anti-Helmholtz configuration. The driver is controlled with a digital input for quickly switching the current on and off, and an analog input for controlling the current supplied to the coils. Toggling the coils from a Helmholtz to anti-Helmholtz configuration must be done manually by reversing the polarity of the output ports of the coil driver. In this way a single pair coils can be used in both the preparation of the trapped atom cloud and also later for use in feshbach resonance studies. When used for trapping, the typical current to the coils is between 4 and 6A.

5.4 Photoassociation Table

The master light is transported via fiber optical cables to a separate optical table where the vacuum chamber and MOT cell are housed. Once the light arrives at the table, it is necessary to further amplify and condition the light for use within the experiment.

The Lithium light arrives to the Photoassociation table already possessing the proper frequencies needed for the experiment. Both the cooling and repump light are amplified through the use of slave lasers. The Rubidium cooling light is amplified using a single slave laser. The amplified light is then sent through an AOM double pass configuration in order to shift the light to the proper frequency. The Rubidium repump light does not require any amplification, but a further frequency shift using an AOM double pass is necessary. The frequency of the light is further shifted on the Photoassociation table for a few reasons; the light is shared among many experiments and this method allows for all of them to be independently functional, and it greatly simplifies the experimental sequencing of devices by keeping any necessary changes local to the Photoassociation table.

The Rubidium repump light only needs to be coupled into the MOT along a single axis. Since the optical pumping is much stronger for Lithium, the repump light needs to be coupled along all three axis with the cooling light for Rubidium and Lithium. To this end, both frequencies of Lithium light are combined on a polarizing beam splitter (PBS) with the Rubidium cooling light combined with the Lithium frequencies using a dichroic mirror coated to reflect the Rubidium light but transmit the Lithium light. Initially a PBS was used in lieu of the dichroic mirror, but issues

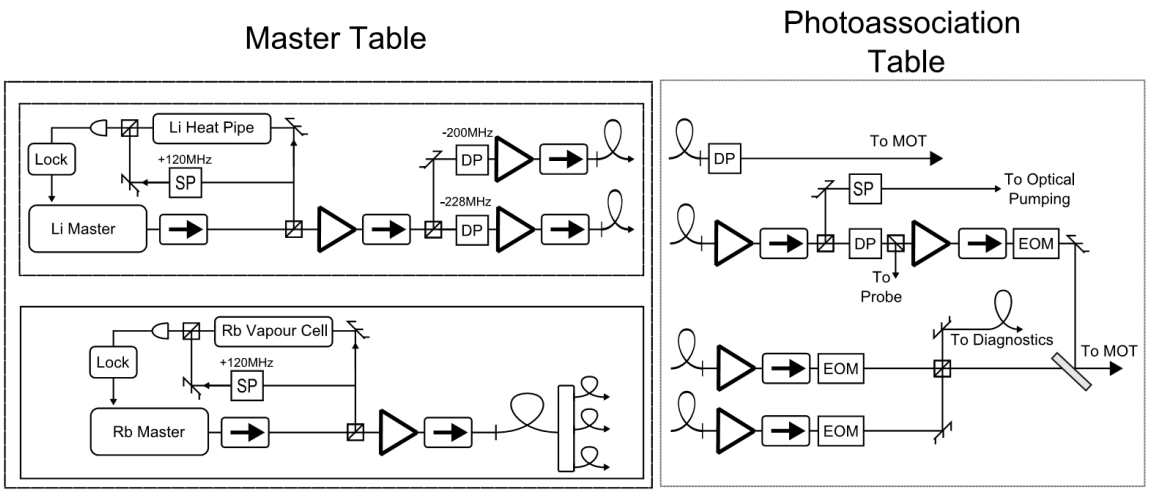

Figure 5.3: Schematic diagram depicting the procedure for creating the necessary frequency locked light on the Master table. The light is then sent to the Photoassociation experiment via fiber optical cables where it is further frequency shifted and amplified before being introduced to the MOT chamber.

arose due to the cross polarization of the Rubidium and Lithium cooling light. Once all the light has been combined along a common optical axis, it is split along the three MOT axes through the use of half-wave plates and polarizing beam splitters.

5.5 Detection Methods

5.5.1 Fluorescence

Fluorescence measurements are the main method for obtaining quantitative measurements of the atom cloud. Since we are trapping multiple species of atoms simultaneously, our experiment requires a means of detecting the light emitted from the Li and Rb atoms together and separately. The trapped atoms are detected using both charge-coupled devices (CCD) and calibrated silicon photodiodes.

Photodiode Individual Thorlabs SMIPD2B photodiodes are used to detect the fluorescence emanating from the Li and Rb MOTs. The detectors have been mounted 30cm from the center of the trap cell in order to increase the optical access for the other laser light and detection methods in the system. A set of two lenses, each having a focal length of 75mm, are used to image the MOT. The lenses were chosen, and positioned, so that each MOT is imaged, unmagnified, in the plane of the photodiode. A dichroic mirror placed directly after the second lens separates the fluorescence light from each species. The Li fluorescence (671nm) is transmitted through the mirror with an efficiency of 98%, while the Rb fluorescence (780nm) is reflected with an efficiency of 96%. The imperfect efficiency of the dichroic mirror is corrected by means of an interference filter with a bandwidth of 5nm around the fluorescence of the desired atomic species.

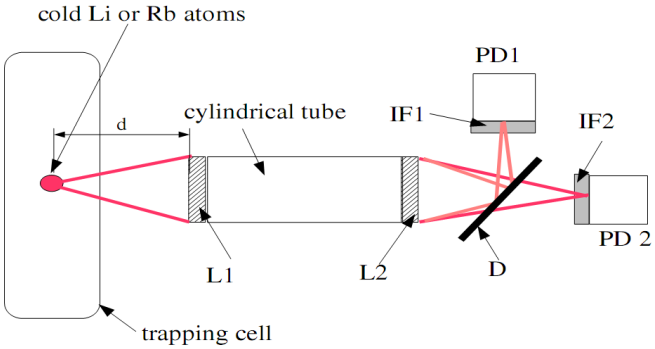

Figure 5.4: The photodiode fluorescence imaging system. The light for both atomic species is imaged independently on PD1 and PD2 through the use of a dichroic mirror and two interference filters (IF1 and IF2).[2]

The signal from the photodiode can be related directly to the number of trapped atoms by the following expression;

$$P_{det} = \frac{hc\Omega}{4\pi\lambda} \cdot L \cdot R \cdot N_{atoms} \cdot \Gamma_{scatt} \tag{5.9}$$

where $\frac{hc}{\lambda}$ is the energy of a single photon, $\frac{\Omega}{4\pi}$ is the solid angle subtended by the detection system at the atomic cloud, L is the signal loss due to optical components, and R is the responsivity of the photodiode in millivolts. This will be further discussed in the **Measurements** section.

Camera A Pixelink PL-A714 monochrome camera with a 1280×1024 resolution and a variable frame rate is used to detect fluorescence due to spontaneous photon emission after a scattering event. It is controlled externally through class functions written into the QDG control system software. In this way, images can be coordinated with state changes in the system.

5.5.2 Absorption

This method images the shadow cast by the atomic cloud on a resonant probe beam. Since the laser light is sent through the region of the cloud, it is important that the width of the light beam is larger than the dimension of the region to be imaged. After the beam has passed through the atomic cloud, it is imaged onto a CCD camera so that the plane of the MOT is in focus. An Apogee Alta series U6 camera, as well as the Pixelink camera described above are used to for this measurement.

5.6 RF State Selection

As discussed in the evaporative cooling section, a magnetic field produces a split in the hyperfine levels of the atom that is dependent on the radial distance from the field minimum. Control of the atomic state is an important part of the experiment

for reasons beyond evaporative cooling. The energy splittings of the hyperfine states or extremely different for each of the three isotopes present in the experiment. For ^{6}Li it is 228.2MHz, for ^{85}Rb it is 3.03GHz, and for ^{87}Rb it is 6.83GHz. This large difference allows independent control over a single atomic isotope, but also requires two separate antenna systems in order to have full control of the entire range of atomic species; a radio frequency system to access ^{6}Li, and a microwave system to access both ^{85}Rb and ^{87}Rb.

5.6.1 Lithium Antenna System

The fine structure energy splitting of the $F = 1/2$ to $F = 3/2$ states in ^6Li is 228MHz. By applying an RF field at this frequency to the atomic cloud, it is possible to drive transitions between the two energy states. In the presence of a magnetic field the hyperfine levels become non-degenerate, allowing for further control of the internal state of the atom. It is also useful to induce state transitions between the hyperfine levels of the $F = 1/2$ state. As discussed in section (2.5), the $m_F = 1/2$ state can be trapped by a magnetic field, while the $m_F = -1/2$ state will be expelled. The zeeman splitting between the two states scales approximately as 1.4MHz/Gauss; our magnetic trap varies from a zero field at the trap center, to 40G at the trap extremities.

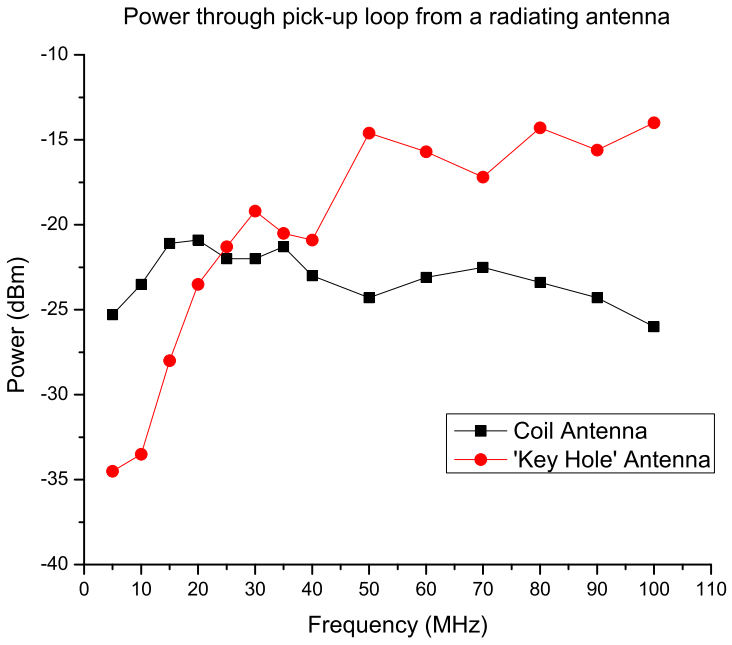

Figure 5.5: Frequency dependence of the radiated power, as measured by a one-loop pick-up coil, of the two RF state selection antennas. The antennas are driven by an amplified signal directly from a DDS device. The sharp decline in output power of the 'Key Hole' antenna at low frequencies necessitated a dual antenna system.

Two different antennas have been implemented for Li state selection. Initially,

a 'Key Hole' antenna was developed for use at 228MHz. This design was primarily motivated by anecdotal advice on the radiative properties of certain antenna designs. It is important that the RF signal couple well into the antenna so as to minimize power loss, and it was advised that this design had been seen to be the most efficient within similar frequency ranges. The first iteration consisted of two antennas placed in a Helmholtz configuration to maximize the radiation power at the position of the atomic cloud. Although marginally more efficient than a single antenna design, space constraints within the experimental setup made the dual antenna setup unfeasible.

The 'Key Hole' antenna was first tested in situ by scanning the frequency from DC to 40MHz in an attempt to empty a magnetic trap of Li atoms. Proving unsuccessful, a ten coil loop antenna, with a diameter equal to that of the 'Key Hole' design, was quickly built and tested in a similar manner. With this design proving capable of emptying the magnetic trap of atoms, it was necessary to characterize both implementations in order to discern the possible reasons for the initial failure.

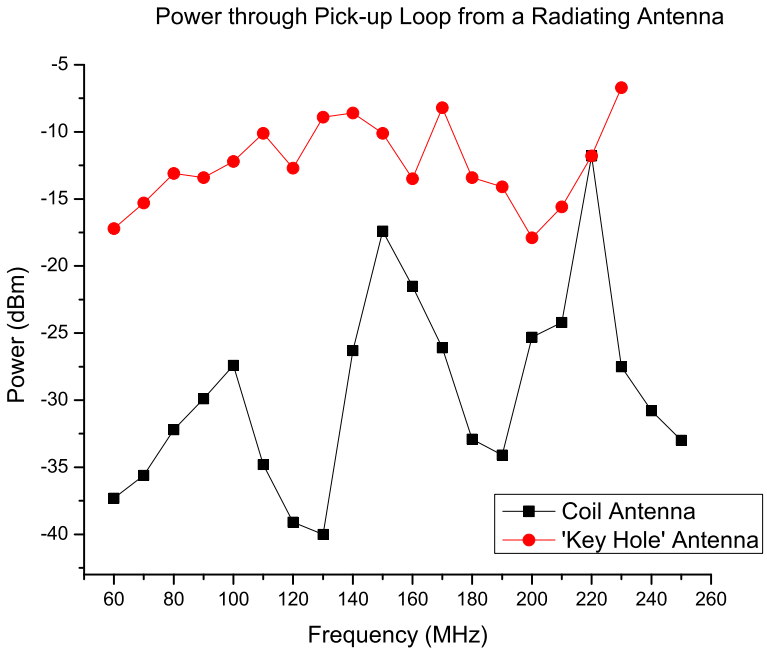

Figure 5.6: Determination of the radiated power of the dual antenna system at high frequencies measured by a one-loop pick-up coil on axis at a distance R from the center of the coils. The antennas are driven by an amplified, frequency doubled DDS signal.

Figs. (5.5) and (5.6) show the relative power fluctuations through a small pick-up coil placed at the equivalent position of the atomic cloud. As predicted, the 'Key Hole' design is much more efficient across most of the relevant frequencies, except within a small region extending from DC to approximately 25MHz where the efficiency of the 'Key Hole' antenna degrades rapidly. Since this range is critical in manipulating the state transfer between the ground hyperfine states, it was decided that a dual system

would be implemented; one using a simple ten coil loop antenna driven directly by an amplified DDS signal, and the second using the 'Key Hole' antenna driven by a 228MHz amplified signal derived from a frequency doubled 114MHz DDS output.

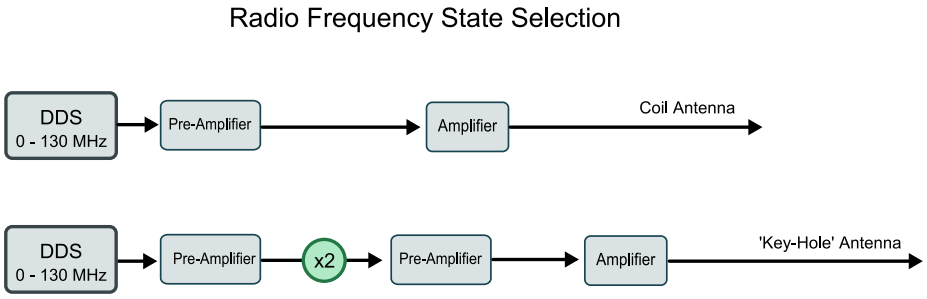

Figure 5.7: Schematic diagram showing the dual antenna implementation for RF state selection. The coil antenna is used to drive hyperfine ground state transitions below 40MHz, while the 'Key Hole' antenna is used to drive transitions at 228MHz.

A schematic diagram showing the method used for controlling the RF signal and coupling it into the atomic cloud is shown in Fig (5.7). In each system, a DDS unit is used to generate the continuous wave RF radiation. The output frequency and amplitude are fully controlled from within the QDG Control System.

Rubidium Antenna System The Rubidium antenna system is being developed to supply microwave frequencies at 3.0 and 6.4GHz to trapped samples of ^{85,87}Rb gas. These frequencies correspond to the fine level splitting in the Rubidium isotopes (Fig. (4.2)). Currently, the components necessary for the signal generation have been built or purchased but are not fully integrated. As the components are modular, the difficulty is only in ensuring that the feedback locking system for the voltage controlled oscillator (VCO) output is working. A major aspect of the design, and one that hasn't been fully formalized, is that of the microwave antenna needed to couple the generated signal into the volume occupied by the Rb MOT. As was the case with the Lithium antenna, this will most likely require multiple design trials with empirical data to determine the efficiency.

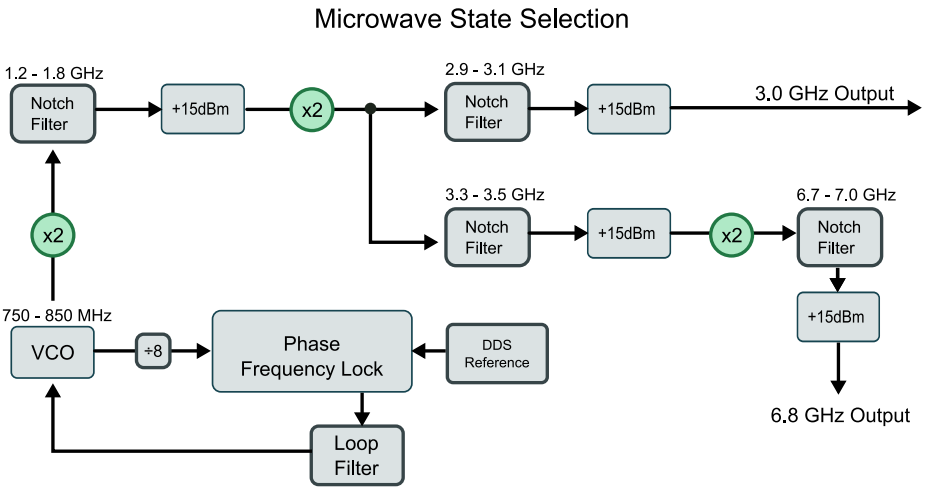

Figure 5.8: Schematic diagram showing the signal generation of the microwave state selection system. A single voltage controlled oscillator (VCO) is used to produce the necessary frequencies for both Rb isotopes. The implementation of an antenna to couple these fields has yet to be realized.

Chapter 6

Control System Hardware

The QDG control system has had many implementations and developers since its early inception. Much of the hardware is based on modified versions of Todd Meyrath's and Florian Schreck's designs while at the University of Texas at Austin. It is from here that the UTBus standard was devised, and where electronic designs of devices not directly associated with the control aspect of the experiment were first imagined.

6.1 Motivation

The nature of cold molecule experiments require precise control of both the state change of individual components, as well as the timing of these events. This control must be highly configurable and infinitely repeatable; the system must be flexible enough to accommodate the future addition of modular components, but rigid enough to repeat the same experiment continuously in order to accumulate the necessary data for proper statistical analysis. What follows is a detailed description of the implementation of the QDG computer control system; the hardware setup,the impetus behind the software design, the current state of the software, and the things that still need to be put in place.

6.2 Hardware Components

The hardware components of the QDG control system can be separated hierarchically by their functionality within the experimental system and by how they are accessed during an experimental sequence.

6.2.1 The UTBus

The UTBus is a parallel, uni-directional bus concept developed by Todd Meyrath and Florian Shreck while members of the *Atom Optics Laboratory* at the University of Texas at Austin. The UTbus consists of 25 lines; 16 data lines, 8 address lines and a single strobe line. This basic bus construct is easily implemented and flexible enough to allow many devices to be connected in parallel. UTBus hardware is common and easily found at reasonable prices from most major electronics distributors.

Strobe The strobe is necessary in order to allow for the inherent latency in latching the data of the devices across the bus. There are various methods of implementing the strobe line. Our method is to manually include the state of the strobe line as a component of the instruction sent out across the UTBus.

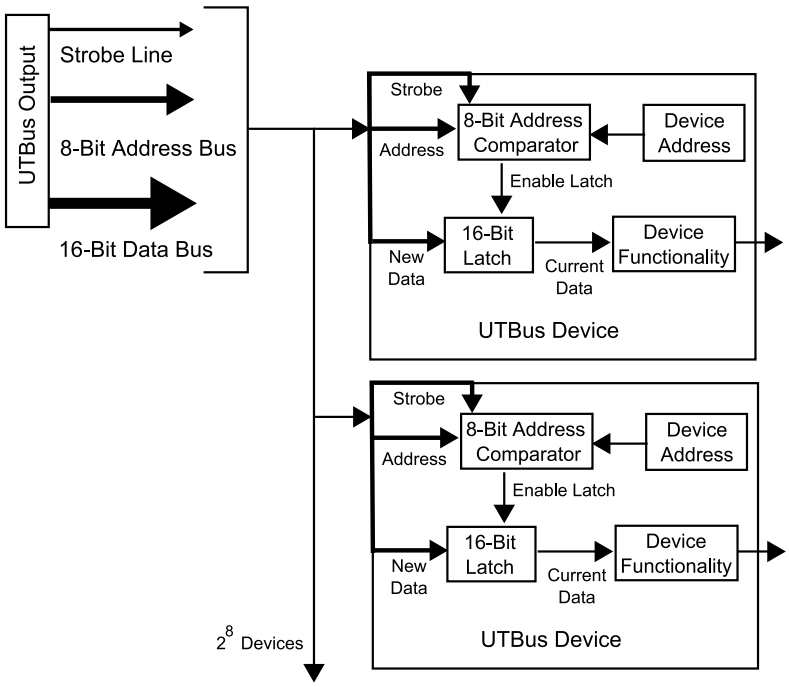

Figure 6.1: Conceptual representation of the UTBus output. Each instruction sent across the bus is received by all devices, but only the one with a matching address allows the data to be latched.

Each instruction is sent out three times; first with the strobe set low, followed by the identical instruction but with the strobe set high, followed again by a low strobe. Data is latched to the registers of a device during the high strobe. As demonstrated by the timing diagram in fig. (6.2), this is done to ensure that the data is given adequate time to latch, settle, and be read by the device before the next instruction is sent, as well as to ensure that the state change of the UTBus Buffer does not overlap in any way with data latching of a device.

It is also possible to have the strobe trigger automatically during a single clock cycle, or instruction output. Further details on this implementation can be found here [58].

Address Lines Each device used across the UTBus has a local 8-bit address, set using DIP switches, that is used in comparison with the address lines sent across the UTBus. Only if the address lines of the UTBus match the address of the device will the strobe signal be accepted, and the data lines latched to the device registers. In theory this allows up to 256 devices to be accessed individually across the bus; in practise this is not achievable as some devices use individual bits of the address line for other functionalities. The description, consequences, and solution to this complication will be discussed further in the addressing section.

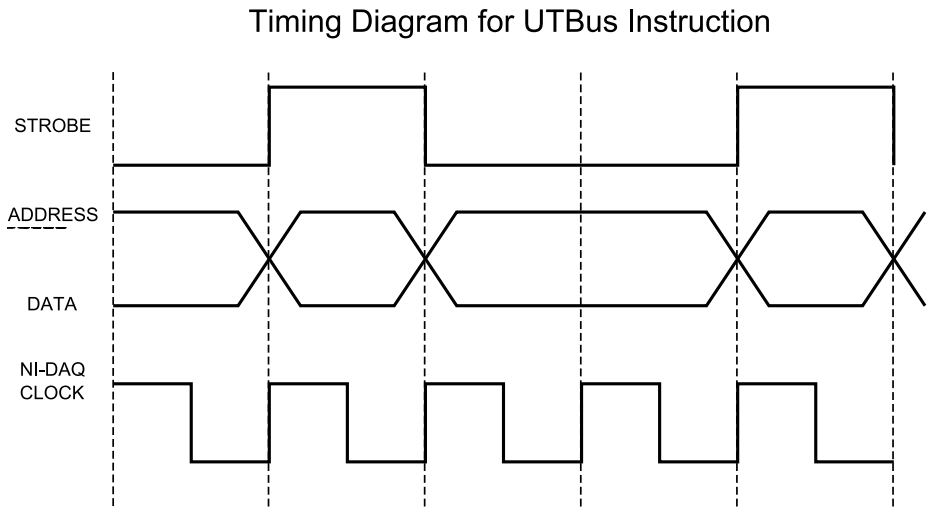

Figure 6.2: Timing diagram showing the latching of data to a device in relation to the strobe signal. Instructions are sent three times across the UTBus, with the strobe set low, to high, and back to low before a new instruction is likewise sent. This modulation of the strobe ensures that the data is properly latched and settled before the next instruction update.

6.2.2 Base Level Devices

This is the foundation of the hardware components. The devices found here act as the interface between the software encoded instruction set and the intermediate level devices. At present, this level consists of a National Instruments Data Acquisition Card (NI-DAQ) with a UTBus Buffer card used to convert and amplify the signal from the 68-pin output of the NI-DAQ card to the 50-pin standard used across the UTBus. In this way a single NI-DAQ card can be used to access many intermediate devices.

NI-DAQ

The NI6534 is a high speed digital I/O PCI device manufactured by National Instruments. Containing 32MB of onboard memory, an 80MB/s maximum transfer rate, and a 20MHz maximum clock, the board provides a well tested, but expensive, method to interface with the upper level devices of the experiment. The added memory bank and clock isolates the output of the card from the timing jitter associated with the multi-threaded operation of the local operating system. The memory bank also allows for a continuous stream of instructions by dividing the bank into independent halves. In this way, each section of the memory bank can be written to while the other section is being read from; instruction sets greater than the 32MB limit can be sequenced continuously with no implications to the timing.

The NI-DAQ is also equipped with input lines for an external clock and trigger. The external clock is a TTL signal sent to the REQ input of the card and is used as a replacement for the internal clock of the card. This can be beneficial for timing instances or to give more precise control of the clock. The internal registers of the

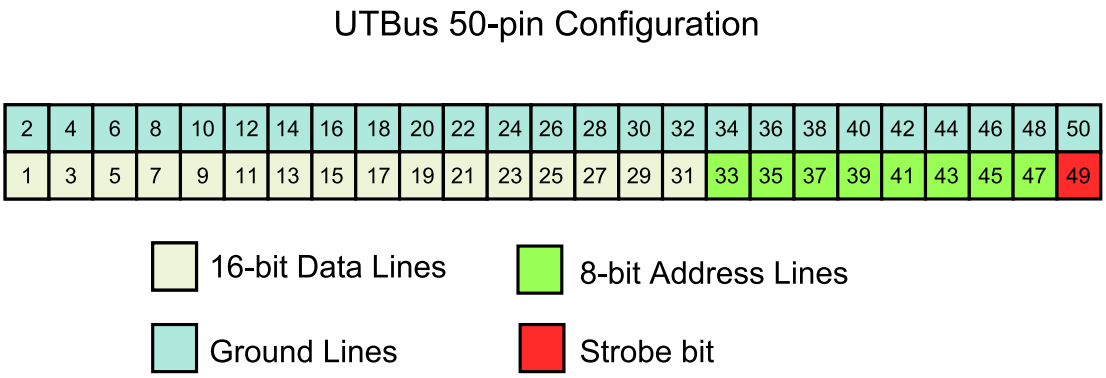

Figure 6.3: Configuration of the 50-pin UTBus connector. The cable and connectors support data transmission over long distances (20ft) and are readily available from most electronic suppliers.[3]

NI-DAQ must be set to accept the external signal in order for the external clock to be used.

The external trigger is extremely useful when the output of an instruction stack is dependent on the state change from some external device. The external trigger forces the output from the card to be held until a TTL high signal is sent to the ACQ1 input of the card. Once this trigger has been sent, the instruction set will output continuously from beginning to end. Again, the internal registers of the NI-DAQ must be properly configured in order use the external trigger functionality.

National Instruments provides thorough support for their devices, unfortunately this is mainly restricted to their proprietary Labview software and a somewhat more useful (in regards to the demands required by the design of our experiment) C class of drivers. Although drivers for use with a Linux based operating system are in existence, they are currently neither robust nor well developed. This is a limiting factor in the extensibility of any software implementation using a NI-DAQ card as it requires a local computer with a windows environment running a C++ based program as the interface to the card.

The initial idea was to have a software system in place that was fully independent of the operating system that it was running on. This is a lofty goal, and one that may still be implemented during future development, but one that is unattainable while remaining tied to the NI card.

UTBus Driver The output of the NI-DAQ card is sent across a 68-pin SCSI connector that is not immediately compatible with the UTBus. The UTBus Driver is used to convert the output from the NI-DAQ to the 50-pin UTBus through the use of an onboard buffer system. The board is also equipped with input lines for the NI-DAQ external clock and trigger, as well as an independent connector for the remaining 7 unused bits of the NI-DAQ. There are various uses for these bits, such as using them in conjunction with an address decoder chip to extend the scope of device

addresses across the UTBus, but none have been implemented within the QDG Control System. The UTBus Driver is also capable of generating a strobe signal based on the clock from the NI-DAQ, but this has been disabled within our system. The board was originally designed by Gerhard Hendl at the Institute for Quantumoptics and Quantuminformation of the Austrian academy of sciences at Innsbruck.

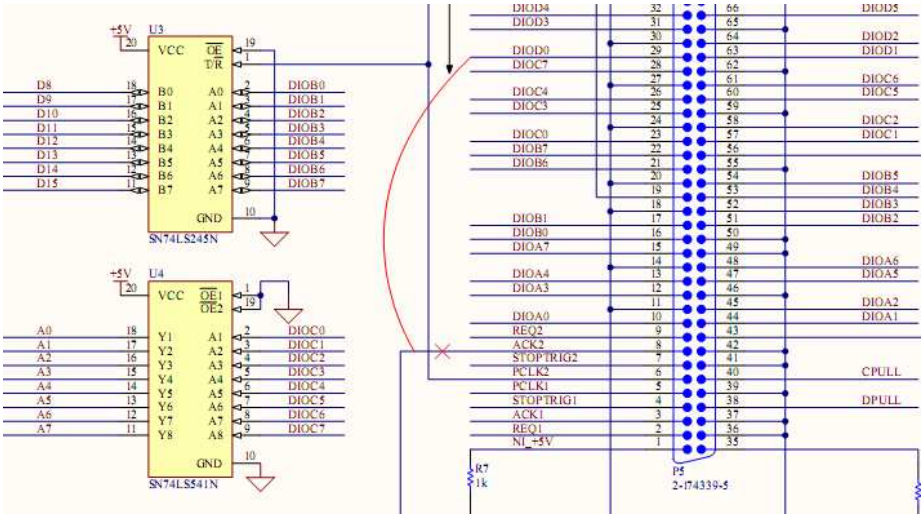

Figure 6.4: During the initial design, the ACK2 line was intended for use as the strobe signal output. However, this proved difficult to control from the software system, so instead the DIOD0 line was rewired for use as the strobe signal line.

Ethernut and Fast Bus Driver

The ethernut is a monolithic system controller developed by Egnite. These are Ethernet-Enabled Microcontroller boards featuring Ethernet, Serial I/O, SRAM/flash ROM, General Purpose I/O lines, and NUT/OS.

The Fast Bus Driver is a concept first proposed by Dan Steck, Kirk Madison and Bruce Klappauf. The Fast Bus Driver contains two blocks of memory; one is used to store the instruction set, the other is used to store a 32-bit time constant associated with each instruction in the set. A comparison is then made between the time constant and an onboard system counter that is endlessly looping from 1 to $2^{32}-1$. When the comparison is true, the instruction corresponding to that particular time stamp is sent onto the UTBus. This has many advantages over the current NI-DAQ implementation. First, Null instructions do not need to be sent over the bus to maintain proper timing intervals; events that are separated by orders of magnitude can be succinctly stored in a single instruction set. Second, the timing can be coupled to an external atomic clock instead of the system clock of the computer or clock of the NI-DAQ card.

The motivation behind using an Ethernut coupled with the Fast Bus Driver as a base-level device is to completely offload the duty of outputting instructions to the UTBus from a local PC running Windows or Linux to a self-contained system accessible from any internet enabled computer. The added advantage of cost and

extensibility are also extremely encouraging. Currently Ethernut boxes are used extensively for accessing data from GPIB enabled devices, while the Fast Bus Driver remains as a work in progress.

6.2.3 Intermediate Level Devices

These are electronic devices capable of outputting analog or digital signals based on the user configurable registers. Devices at this level are all accessed by way of a 50pin UTBus consisting of a 24-bit bus plus one strobe bit. The bus is further reduced to a 16-bit data bus and an 8-bit addressing bus. The addressing of each device will be explained in further detail,

Direct Digital Synthesizers

The original DDS device was designed by Todd Meyrath and Florian Schreck while at the University of Texas at Austin and is based around the AD9852 chip from Analog Devices. The DDS is able to generate radio frequency signals between DC and 150MHz. The PCB board is housed in an aluminium enclosure with BNC connections for Reference Clock and FSK inputs, and Cosine and Control DAC outputs.

The AD9852 has two high speed output; an RF (cosine) output and an arbitrary DC 'control' output. The RF output shares the DC offset of the control DAC output. A 9th order 135MHz Low Pass Elliptic Filter cleans the RF signal before the BNC output from the DDS. This gives a very fast drop off past 135MHz, with a 60dB stopband at the 150MHz Nyquist frequency.

The 16-bit data line of the instruction set is segmented by function. The first 6-bits (D0 to D5) are reserved for locating a specific register address of the AD9852. Although this gives 64 unique memory addresses, many of these are unused, while others are grouped together in order to increase the data size of the specific function. Subsequently, the D6 data bit is used to set the FSK/BPSK/Hold function, D7 is used for the shaped keying functions, and bits D8 through D15(MSB) represent the 8-bit data to be stored in the address register (Fig. 6.3). As an example, the amplitude of the cosine output can be changed by addressing two registers on the AD9852. These two registers combine to hold a 12-bit integer (the last 4-bits are unused) that determines the fraction of the total amplitude to be outputted. In order to modify the cosine amplitude parameter, two instructions must be sent across the UTBus. Often, a single state change of the DDS will involve addressing multiple registers of the AD9852.

The peak-to-peak cosine output from the DDS is -7dBm. Since the main function of the DDS devices in our experiment is to drive the acousto-optical modulators, an amplification system is necessary to reach the 31dBm necessary to drive the AOMs. The first stage in the amplification is a pre-amplifier with a +13dBm gain and a maximum input of +16dBm. The output from the pre-amplifier is then sent to a home-built amplifier capable of increasing the signal to a maximum 31dBm. Both devices were designed and built by the electronic shop resident to the UBC physics department.

The output power from each of these stages was measured as a function of both the output frequency and amplitude. This characterization shows a slight non-linearity of the final amplified signal with respect to an amplitude change, and some minor fluctuations with respect to frequency. For most applications these non-uniformities are insignificant; however, any implementation that is highly dependent on the precision of the output will need to correct for these deviations. In general, it is important that the outputs of the amplifier be terminated when in use to avoid damage caused by reflections from an unterminated output.

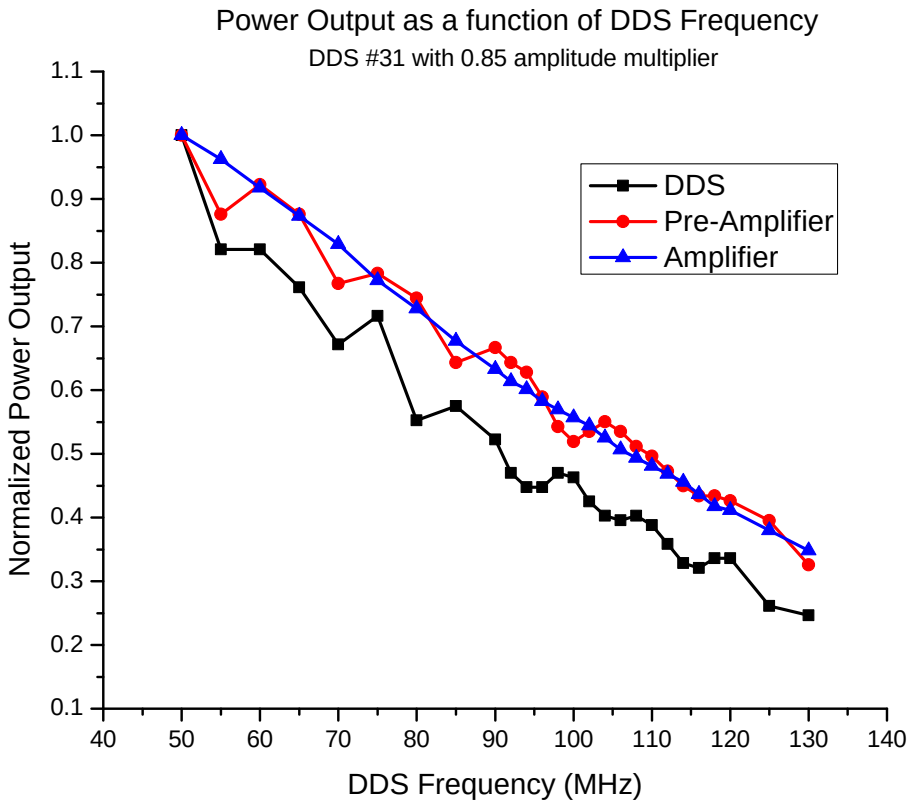

Figure 6.5: Frequency response of the DDS amplification system. The amplitude of the DDS decreases linearly as the frequency approaches the cutoff of the low pass filter of the cosine output. The response of the pre-amplifier and amplifier show non-linear variations.

The original design of the DDS PCB board was modified to allow greater and more transparent access to many of the built in functionalities present on the AD9852. Most critical was direct access to the frequency shape key input, necessary in order to use the DDS devices in conjunction with the locking system for our Master lasers. The original design can be viewed freely from Todd Meyrath's homepage [1]. The top view of the new design is shown in fig (6.7). Although this is a universal design, there

[1] http://george.ph.utexas.edu/ control/

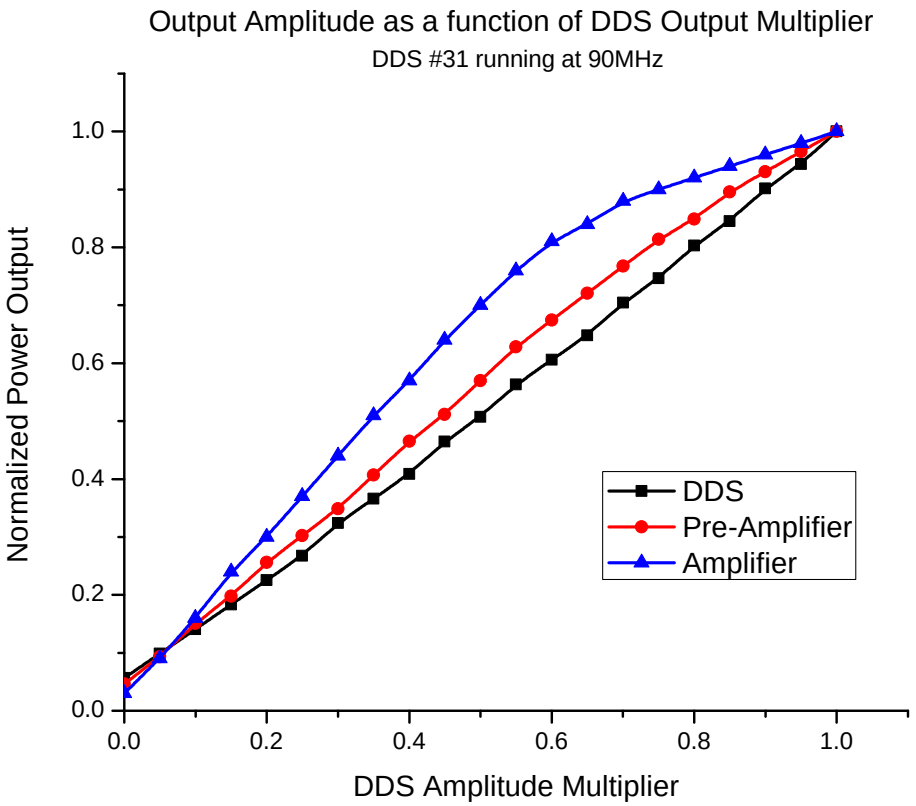

Figure 6.6: Amplitude response of the DDS amplification system.

are currently four different implementations, each serving a distinct purpose. The relevant jumper settings will be discussed independently for each DDS type.

The DDS can be run at a maximum frequency of 300MHz, giving a theoretical maximum output frequency of 150MHz. A 15MHz clock is fed via BNC to each of the DDS units. An internal PLL clock multiplier, set to an integer between 4 and 20, is used to increase this frequency to the maximum 300MHz. This 15MHz frequency is based on a 10MHz atomic Rubidium clock as discussed below.

Master Table DDS Design These DDS units were modified in a way that allowed the 177kHz dither signal from the lock boxes to be used as the input for Frequency Shape Keying (FSK). In order for this to work, the FSK input was first routed through the AD9852 onboard comparator. The TTL output from the comparator was then run directly to the FSK register pin on the AD9852. This allows the ramped output of the DDS to be synchronized to the internal dither signal of the lock box. These DDS units have jumpers W11 and W18 populated with 0Ω resistors, with W13 left unpopulated.

General FSK Modified DDS Design These are similar to the Master Table DDS units, except that the FSK BNC input has been routed directly to the input

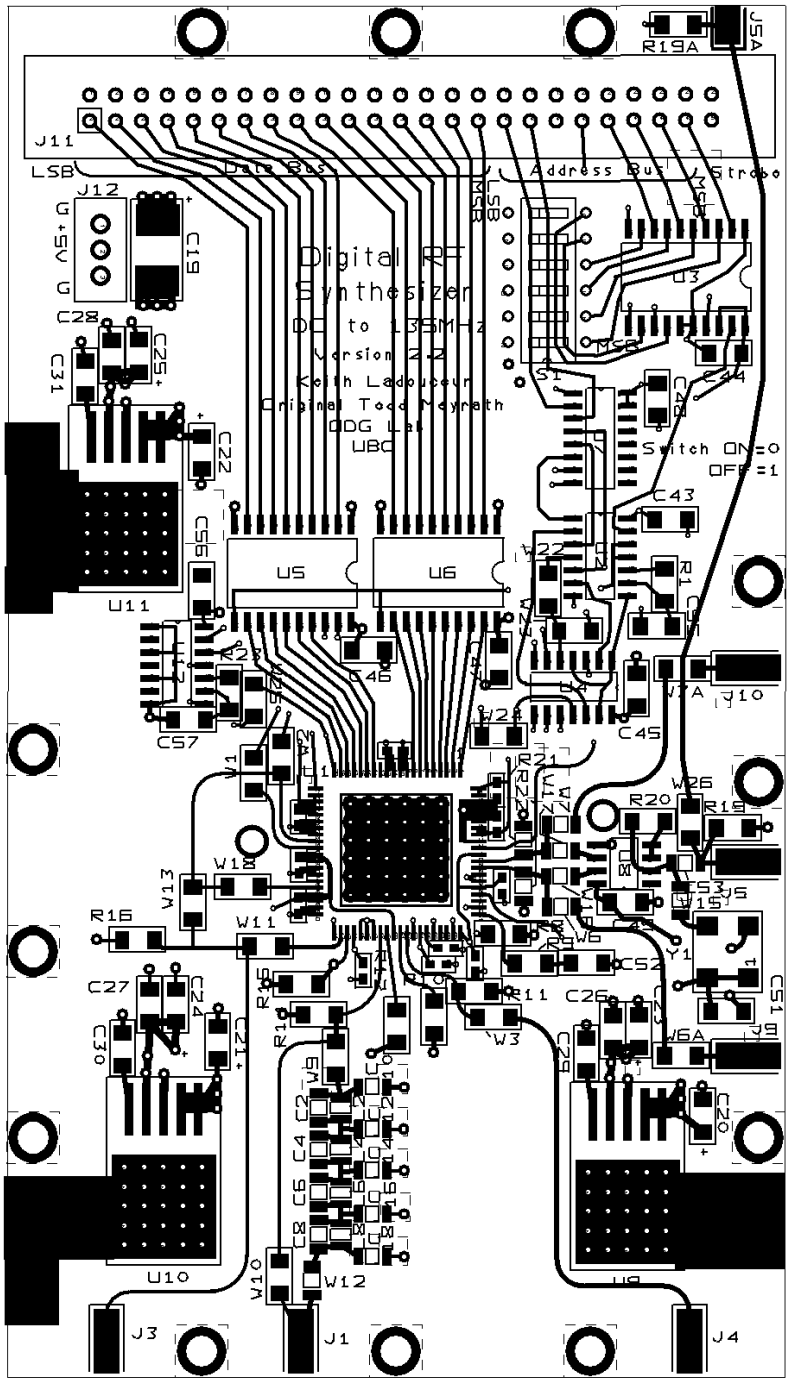

Figure 6.7: Top level PCB layout of the modified DDS device. The functionality of individual units can be tailored for a specific requirement by changing the location of 0Ω jumpers.

of the FSK register pin on the AD9852. Since the comparator has been bypassed, the input is required to be a TTL with a minimum 0 to +3.3V signal. These DDS units have jumper W13 populated with a 0Ω resistor, with positions W11 and W18 unpopulated.

Clock DDS Initially a Stanford signal generator was used as the source for the 15MHz DDS clock. The utilization of such an expensive device for such a static, mundane task was not optimal. Instead an attempt was made to clock all the DDS devices using a single DDS device as a 'master clock'. These units are identical to the *General FSK Modified DDS* described previously; the distinction is that they are clocked by a 10MHz reference from an atomic Rubidium clock. The 10MHz atomic clock cannot be used directly as the DDS clock as it does not maximize the internal frequency of the DDS, as the internal clock multiplier only goes up to 20. The 15MHz output is fed through a pre-amplifier and subsequently out to all other DDS units in the system. It was found that a single pre-amplification stage was sufficient to drive in excess of 32 DDS units. There is a single Clock DDS for the Master Table with a separate unit for the Photoassociation table.

TTL Output DDS Design It became apparent that a DDS with the ability to output a TTL signal at a user controlled frequency would be extremely useful within the context of the experiment. This functionality can be accomplished using the Digital Output devices, but this requires a periodic update across the UTBus for every state change of the signal. Clearly, this becomes an issue for extended time frames and for frequencies approaching the clock of the NI-DAQ card.

To achieve this we use the RF output as the input to the comparator on the AD9852. Initially there was an issue with the DC offset of the RF output. Since the comparator, by default, uses the ground plane of the board as the comparison signal, the output from the modified DDS units were permanently set to a high state. There are two solutions to this problem; using a simple DC block circuit to remove the offset, or to wire the control DAC output as the reference to the comparator in lieu of the ground plane. Both methods were implemented and tested, giving equivalent results. Ultimately the latter was used for all modified boards as it was the simpler and cleaner option, although it requires that the control DAC output be set properly in order to ensure a square wave output with a 50/50 duty cycle.

To duplicate the functionality of these boards, the following modifications are required. The output of the cosine DAC, taken prior to the low-pass filter, was wired to the non-inverting V_{in} (VINN) pin of the AD9852. The output of the control DAC was wired to the inverting V_{in} (VINP) pin of the AD9852. Finally, the output of the comparator was wired to the control DAC BNC output (jumper W3 must be unpopulated).

Analog Output Device

The Analog Output (AO) device is another product of Todd Meyrath and Florian Schreck. This device utilizes the DAC7744 from Texas Instruments as the basis for

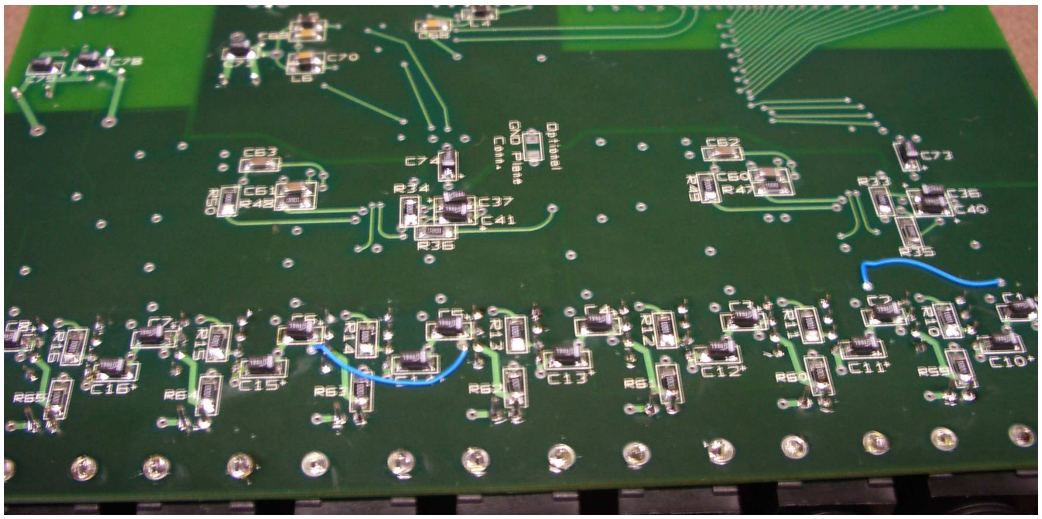

Figure 6.8: A broken connection to the power inputs of two integrated circuits on the Analog Output devices required the addition of small wires to bridge the gap.

an octal 16-bit digital to analog converter. Each quad DAC shares a single voltage reference across the four channels. This introduces the possibility of cross talk among those channels, but is simpler than implementing individual DACs with isolated voltage references. Only a single output can be updated on an instruction cycle, but each can be updated without altering the state of another channel. The BNC outputs are buffered to drive 50Ω loads using an OPA227 precision opamp with a BUF634 buffer line driver. The buffer is able to boost the current of the opamp output. Each channel is capable of outputting between ±10 Volts with 16-bit precision and a maximum current of 250mA.

If the strobe signal and address match the comparator, then the strobe signal is passed to the rest of the circuit. Three bits of the 8-bit address are used to select which of the 8 DAC channels (one bit selects the quad DAC, the other two the specific channel on that DAC) receives the chip select (CS) signal to load the data bits into its memory latch. Once the data has settled, the delayed strobe line triggers the 'load DAC' input that moves the data from the memory to the analog output where it is held until the channel receives another state change instruction.

AO Driver Fixes There have occurred minor issues with the build of our AO devices, these will be briefly discussed as a matter of documentation.

The boards were found to have a broken connection in the power connections to two of the ICs. The solution was to manually bridge the power connections using a small wire (the blue wires seen in fig. (6.8)).

It was also noticed during testing that certain boards failed to output the correct voltage. This was eventually attributed to a capacitor which had been soldered in the incorrect orientation, resulting in improper reference levels to the DAC7744. Once the capacitors were reoriented, the problem was fixed.

Testing and Implementation The circuit for the analog output devices contains a built in delay line that allows for the latched data to settle in the register before it is used to update the output of the DAC. This delay line, coupled with the inherent latency of the circuit results in an upper limit on the frequency that these devices can be updated. It was found that the default frequency of 20MHz for the internal NI-DAQ clock was too fast; the first instruction sent to the device was ignored as the data register was changed before the update trigger reached the DAC. The delay line is around 100ns, meaning that a maximum update of 10MHz should be possible.

The AO has a DIP switch setting for the strobe line, it is unique among the three devices in this regard. In order for everything to work properly (in terms of updating and timing) it is imperative that this switch be set so that the device latches the data on a strobe high. This is in line with the other devices.

Digital Output Device

Another device designed by Meyrath and Schreck, this is a 16 channel digital output capable of driving 50Ω loads at $+5V$. The board is a simple circuit consisting mainly of two 8-bit latch components. The Strobe bit is passed through the comparator if the local address matches the full 8-bit address line of the UTBus. This passed strobe commands the data latches to accept and hold the new 16 data bits. Each of these 16 data bits is followed by a line driver and a BNC output. The latch is necessary as a memory device for holding the state of the individual outputs until a new data set is sent across the bus. This means that it is not possible to address a single digital output channel, the state of unchanged channels must be resent with the desired changes in order to maintain their output state.

Addressing

In general these address lines are used as a comparison to the onboard DIP switch setting of a given device. If the address matches the DIP switch then the data lines are passed to the device (this is a simplification, but in a general sense it is valid). All devices are connected in series along the UT bus, addressing allows us to specify which device among many we wish to configure.

The difficulty lies in the fact that certain devices use some of the address lines for functions other than comparison. This means that careful consideration must be taken when assigning addresses so that a single data packet is not passed to multiple devices.

Direct Digital Synthesizer (DDS) The first two bits of the address line are used to determine the onboard strobe function of the device. This leaves the 6 most significant bits (MSBs) used for the onboard comparison that selects the device. In regard to the DIP switch settings: ON = 0 and OFF = 1; DIP switch 6 is the least significant bit (LSB) while DIP switch 1 is the MSB.

Analog Out (AO) The first three bits of the address line are used to select among the 8 outputs on the device. This leaves the 5 MSBs for device selection. Again,

8-bit Address Bus			
A0	A1	Option number	Function of Strobe bit
0	0	0	Latch Data Bus, Master Reset
1	0	1	Latch Data Bus, Load Data into DDS Buffer
0	1	2	Latch Data Bus, Update Output Register
1	1	3	Latch Data Bus
Address Bits A2 to A7 must match DDS Address DIP switch DIP Switches: ON = 0 ; OFF = 1			

Figure 6.9: Strobe function settings for DDS device[3]

ON = 0 and OFF = 1; DIP switch 1 is the LSB and DIP switch 5 is the MSB. DIP switch 6 sets the value of the onboard strobe bit comparison. This switch should be set to ON for all analog output devices used within the QDG control system.

Analog Output Address Settings		
Address	Output Connector	Output Label
111 XXXXX	J1	Out 7
011 XXXXX	J2	Out 6
101 XXXXX	J3	Out 5
001 XXXXX	J4	Out 4
110 XXXXX	J5	Out 3
010 XXXXX	J6	Out 2
100 XXXXX	J7	Out 1
000 XXXXX	J8	Out 0
Address Bits A3 to A7 (XXXXX) must match AO Address DIP switch DIP Switches: ON = 0 ; OFF = 1		

Figure 6.10: Output select settings for the Analog Output where XXXXX refers to the device address[4]

Digital Out (DO) The DO device is the simplest to consider as all 8 address bits are used solely in the comparison. As before ON = 0 and OFF = 1; DIP switch 1 is the LSB and DIP switch 8 is the MSB.

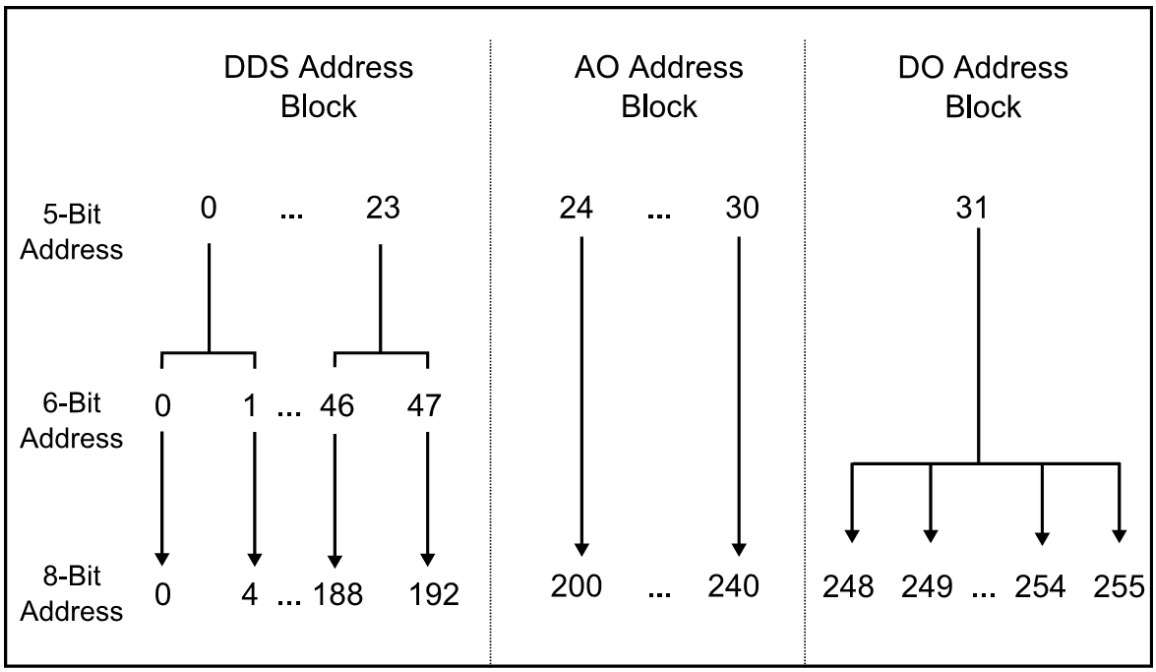

Figure 6.11: Addressing hierarchy for the QDG control system. This is necessary due to the variations in how the 8-bit address of the UTBus is used to access specific devices. This addressing method ensures that no two devices will be updated during the same clock cycle

QDG Addressing System In order to alleviate any complications arising from mistakenly addressing multiple devices, we begin by assigning address blocks within the 5-bit section common to all three devices. So long as these are unique we can be assured of never addressing multiple devices. After these blocks are assigned it is simply a matter of extrapolating the 5-bit address to an address corresponding to the number of comparison bits used by that device. Since the analog out devices use 5-bits, the values assigned are those that are used to set the onboard DIP switches. The 24 addresses assigned to the DDS devices actually correspond to 48 unique addresses when mapped to the 6-bit comparison used by the device. Finally, the single assigned address for the DO devices maps to 8 unique addresses.

6.2.4 High Level Devices (Actuators)

These devices perform some function during the experimental sequence, and are driven by the outputs from the intermediate level devices. Within this level there are acousto-optical modulators (AOM), electro-optical modulators (EOM), mechanical shutters, and CCD cameras.

AOM Acousto-optical modulators are used frequently within the experiment for frequency shifting, modulation, and as fast shutters. They are composed of a crystal with a density dependent index of refraction. When a high-power acoustic wave is coupled into the crystal, the resulting longitudinal sound wave generates a density

variation across the crystal. When driven in this manner, the crystal effectively becomes a diffraction grating, albeit one that is moving at the velocity of sound. A light beam sent through the crystal is diffracted such that the frequency of the first order beam is shifted by the frequency of the acoustic wave.

EOM Electro-optical modulators are composed of a crystal whose index of refraction is dependent on the strength of an applied electric field. Since the phase of a light beam travelling through the crystal is proportional to the refractive index, it is possible to fully control the phase of the emitted light by varying the electric field supplied to the crystal. The use of a Glan-Thompson prism at the output port of the EOM effectively allows for control of the light intensity by way of the phase. The electro-optical modulators used within the experiment are Linos LM 0202 'Laser Modulators'. A high-voltage driver is controlled by way of an analog input from 0 to 10V.

Mechanical Shutters Mechanical shutters allow for the complete extinction of laser light, and are used extensively within experimental sequences. Designed by Paul Lebel and Davey Mitchell[59], a set of Ultrafast Mechanical Shutters, exploiting a shutter flag attached to the actuator arm of a modified iPod© hard drive to block the beam path of a laser beam, are placed after each of the electro-optical modulators. The shutters are controlled by a driver circuit triggered from the output of a DO device with a response time of 141μs, and a jitter in the latency time of 8μs.

CCD Cameras The Pixelink and Apogee cameras used within the fluorescent and absorption imaging can be controlled remotely by way of firewire and USB connections to the control system computer. The exact nature of the control is far more complex than for the other devices described; they are triggered by a signal from a DO device, but other functionalities cannot be accessed across the UTBus. The modularity of the Python implementation has allowed for a new function class, incorporating device drivers for these cameras, to be written; among other settings, the gain, exposure time, and region of interest can all be controlled from within an experimental script.

Chapter 7

Control System Software

There was a great deal of discussion concerning how the software aspect of the control system should be implemented. The recurring theme throughout was that the implementation should be extensible; simple to use during testing, but deep enough to support complex timing and optimization routines once the autonomous data acquisition aspect of the experiment was reached. To this end, it was agreed that a Python based scripted hierarchy with C++ based daemon to interface with the NI-DAQ card would give the best balance between near-term usability and long-term adaptability. Although the software development began under my own attempts, it was soon realized that a system of this complexity would require someone with a much greater knowledge, and much more experience, to fully implement our ideas. The task of coding was taken up by our resident Python guru, Ovidu Toader. This section will not be a comprehensive dissection of the system, but instead should give the reader enough insight to understand the main components, the reasons they were implemented in the manner that they were, and the ability to write a basic instruction script for use within our experiment. Even as this section is being written, new functionality is being added to the control system by the addition of new class structures and modules. As this is an ongoing process, what will be presented is not the final state of the project.

7.1 Design

The design of the software is divided into two main sections; a Python based scripting language meant for the creation of user defined experiments, and C++ based interpreter for interfacing with the NI-DAQ card.

As with all computer peripherals, hardware specific drivers are required in order to interface the between the NI-DAQ card and the operating system. Currently, National Instruments has only developed drivers for their proprietary LabView program or ones written in C. It was clear that part, or all, of the system would need to incorporate one of these two programming languages.

Python Python is a high-level programming language that supports multiple programming methods, including object oriented, functional, and imperative. It is open source and cross-platform, with the ability to integrate with other languages.

LabView As with C++, there was some initial discussion about basing the entire control system software on LabView; our lab has access to a campus wide site license (negating slightly the cost analysis of this method), the drivers are native to the

program and thus more easily implemented, the initial time frame for implementing a working system would be shortened considerable by the inherent pre-built modules provided by NI. As usual, the easy way is not always the most appropriate. The greatest flaw in developing a system based on LabView is the desire that the program should eventually be portable and able to run on any computer. Further, some of the more complex aspects, such as timing conflict resolution, would have been much more difficult (if not impossible) to implement under the constrictions of the program. The ultimate placement of LabView programs within the control system hierarchy will be revisited, but it was not to be used at the interface with the NI-DAQ card.

C++ Moving away from the LabView option meant that C++ was to be the programming language of choice, but there was still the decision of creating a monolithic system from a single language, or to segregate the responsibilities between various subsystems. The first attempt, written and documented by Ray Gao [ref] as a summer student, was focused on the former idea; a single program that took care of parsing user input into an instruction stack to be sent out over the UTBus via the NI-DAQ card. A basic gui interface was developed, but the project languished in a usable but ultimately unfinished state. The task of completing the project, and incorporating some of the more complex modules, fell to various other members of the research group, and ultimately to myself. It soon became clear that the programming knowledge needed to fully implement every aspect of our ideal control system was beyond my abilities, especially considering that the experiment itself was quickly becoming functional and that a fully integrated system would need to be in place before any data could be taken. It was at this point that the services of Dr. Toader became available, and the decision to relegate the role of the C++ program to that of a bytecode interpreter and a virtual device to interface with the NI-DAQ card was made.

7.1.1 C++ Daemon

The C++ Daemon is ultimately responsible for interfacing with, and controlling, the NI-DAQ card on the local host machine. It acts as a *bytecode* interpreter that uses hardware drivers to send data from the NI-DAQ across the UTBus. *Bytecode* is the intermediate state of the data between the output from the QDG Control Program and the input to the C++ Daemon. It is a mixture of machine code instructions to be stored in the memory register of the NI-DAQ, and further commands concerning the internal states of the NI-DAQ itself. In this way *bytecode* should be differentiated from the *instruction stack* discussed in other sections, as the *instruction stack* refers only to the final set of 24-bit machine code instances to be sequentially sent out across the UTBus.

7.2 Control System Modules

The entire program has been created as a set of modules, each tasked with specific functionalities relating to the various aspects of the hardware system. These modules

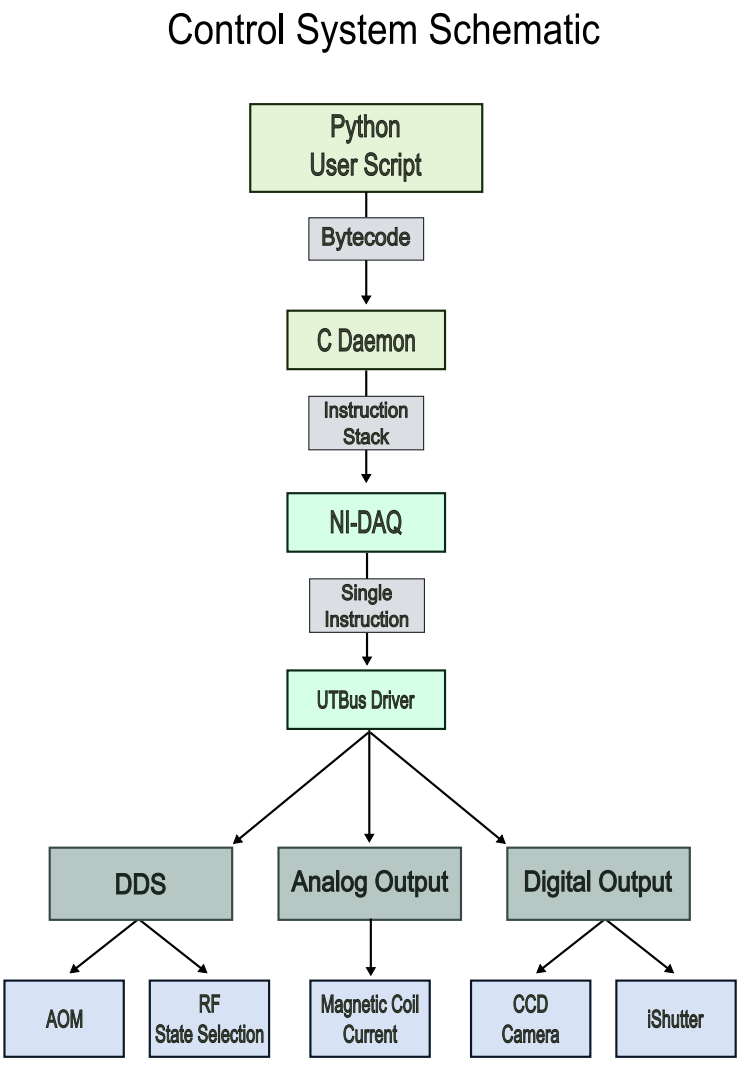

Figure 7.1: Schematic showing the Control System hierarchy. A user written control script is written in Python. Bytecode is generated and passed to the C++ Daemon, which in turn updates the NI-DAQ card and writes the instruction stack to the onboard memory. The NI-DAQ sends a single instruction across the UTBus every clock cycle. The instructions update the state of a specific device on the bus. The state of the device determines the output, which is in turn used to drive the state of an experimental actuator.

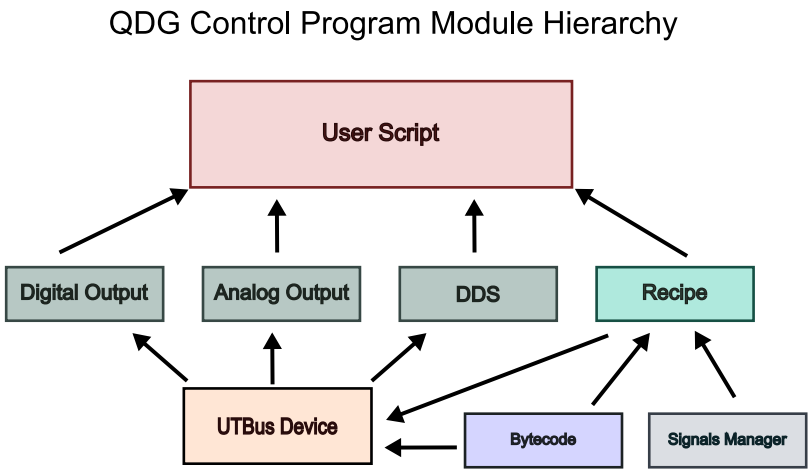

Figure 7.2: Module schematic showing the relation between the major components of the QDG Computer Control Program.

are named for storage and re-use, and can be arbitrarily nested to any depth. There are modules responsible for implementing commands to the DDS, the Analog Output, and the Digital Output, with a general UTBus module with functions common to all devices used across it. Further, there are modules with functions relating to the *bytecode* generation, and the managing of signals and events. The timing of each module is self-enclosed in that it does not rely on any absolute external reference. Timing is relative to the beginning of the top level module; individual elements can be moved in time either by altering the arrangement of the actions and directives relative to each other, by the inclusion of wait cycles, or by signifying a specific time placement relative to markers placed within the module. The state of each module is saved in a data file, this file is read during the recipe generation such that only those sections of the module that alter the existing state are scheduled. This is beneficial in reducing the run time of individual experimental sequences.

The full extent of the system will not be presented here, this is done mainly for reasons of clarity; the subtleties inherent to much of the *bytecode* generation and timing are inconsequential for writing and developing basic and high level experimental scripts. What will be presented is the main hierarchy of modules, with the most relevant commands for each.

7.2.1 DDS module

This module contains functions relating to the DDS device. The DDS module is itself a subclass of the UTBus Device module. A new DDS device is instantiated with the following command

$$\begin{aligned} &\textit{DDSName}\text{=DDS(address = }\textit{DDSAddress}\text{,refclock = }\textit{15MHz}\text{,}\\ &\qquad\text{refclock\_multiplier = }\textit{20}\text{, internal\_FSK = }\textit{False}\text{)} \end{aligned}$$

where *DDSAddress* corresponds to the 8-bit address of the unit. Once instantiated, the following commands can be used to change the state of the device.

DDSName.reset()
Resets the DDS device to the default values. There exists a reset functionality built into the AD9852 that this function uses. Often useful when initiating a DDS device for the first time, or as a fall back option when the device does not seem to be working properly. In the rare event that the device is not updating properly, and the *DDSName.reset()* call has no effect, it might be necessary to manually delete the state file for that device.

DDSName.set_amplitude(Value)
Sets the peak to peak amplitude of the cosine output. Requires a value between 0 and 1 as the input. This function requires fewer instructions to be sent across the bus than many of the frequency functions. If it is desired that the output of a particular DDS be turned off, a call of *DDSName.set_amplitude(0.0)* may be the simplest and quickest method.

DDSName.single_tone(FrequencyValue)
Programs the DDS to output a single frequency from the cosine output. Frequency values from DC to 135MHz are valid, although it should be noted that the output amplitude of frequencies above 110MHz decline rapidly with increasing frequency.

DDSName.unramped_FSK(Frequency1,Frequency2)
Requires two frequency values as input, where the first must be the lower of the two. Toggles between the two frequencies with a period equal to that of the TTL signal sent to the FSK input of the DDS unit. If this is used in conjunction with a Master Table DDS, it is important that the *DDSName.enable_comp()* call be used to ensure that the onboard comparator is enabled. These particular DDS units require a sine wave signal to the FSK input.

DDSName.ramped_FSK(Freq1,Freq2,FSK Period)
Sets the DDS to run in a ramped frequency mode where the output varies in discrete steps from the initial frequency to secondary frequency and back in a continuous fashion. The period of the TTL signal used as the FSK reference is required in order that the step size be properly calculated. If this value is incorrect, it is possible that either the full range of frequency values will not be reached, or that significant time is spent at one of the boundary frequencies before the ramp is continued.

DDSName.enable_comp()
Enables the onboard comparator of the DDS unit. By default, the comparator is disabled. Enabling the comparator is necessary for both the Master Table DDS units and the TTL DDS units.

DDSName.enable_control_DAC()
Enables the output of the control DAQ. By default the control DAQ is disabled. Must be enabled for the TTL DDS units to function properly.

7.2.2 Analog Output Module

This module contains functions relating to the Analog Output device. The module is itself a subclass of the UTBus Device module. A new AO device is instantiated with the following command

AOName=AnalogOutput(address= *AOAddress*)

where *AOAddress* corresponds to the 8-bit address of the unit. For simplicity, each individual output of a Analog Output board is treated as a unique device. Once instantiated, the following commands can be used to change the state of the device.

AOName.set_ scaled_ value(ScaledValue)
The *ScaledValue* parameter represents the desired output voltage of the analog output channel between -10 and 10. This is a decimal number with 16-bit accuracy.

7.2.3 Digital Output Module

This module contains functions relating to the Digital Output device. The module is itself a subclass of the UTBus Device module. A new DO device is instantiated with the following command

DOName=DigitalOutput(address = *DOAddress*)

where *DOAddress* corresponds to the 8-bit address of the unit.

DOName.set_ bit(Index, State)
Sets the state of a single channel for a particular Digital Output device. Since the entire 16-bit register is rewritten during each update, the previous state of all 16 channels are saved in a state file. When this function is called, the bit corresponding to the index of the output is changed with the saved states of the other bits held unaltered. To set the 6th channel of a sample Digital Output device to a high state would require *SampleDO.set_ bit(5,1)*.

DOName.reset()
Resets the state of all 16 channels to 0 (Low).
As an aside, it is important to note that the DDS module has been programmed with a hardware emulator that mimics the registers on the AD9852 DDS controller. The execution of a recipe results in a full update to the virtual registers, but only those instructions that alter the state of the physical DDS controller are included in the bytecode sent across the UTBus. This is done as a means of optimizing the instruction stack by reducing the number of instructions sent out across the UTBus. As an example, consider the case of a frequency update. A total of four registers are used to store the value of the frequency. If the difference between the new frequency value and the old one is small, it may only be necessary to change the value stored in the least significant register. In this instance, only a single instruction, instead of

four, would be sent across the UTBus. Although this method is useful in reducing bytecode chatter, it limits the ability to predict the exact time required for certain DDS instructions to be transferred via the UTBus. The only certainty is that the time needed to update the DDS device will be less than or equal to the time needed to program the device from a reset state.

7.2.4 UTBus Device Module

A generic module composed of functions and characteristics common to all devices across the UTBus. The user does not use any of these functions directly when creating an experimental control script.

7.2.5 Recipe Module

This module defines the recipe class, of which each user script is a subclass of. A recipe is instantiated at the beginning of the script with the following command

$$R = \text{Recipe}(\textit{RecipeName}, \text{use\_internal\_clock}=\textit{True}, \\ \text{sampling\_frequency\_divider} = \textit{2000}, \text{use\_external\_trigger} = \textit{False})$$

Further commands within the instantiation include the ability to set an external clock *set_utbus_external_clock = Frequency*. Once defined, *R.start()* marks the beginning of the control sequence, with *R.end()* marking the end. It is possible to include a delay within the instruction set through the use of the *R.wait_s(Time)* command. Related to this call is also *R.wait_ms(Time)* and *R.wait_us(Time)*.

7.2.6 User Defined Experimental Scripts

The user creates a 'Recipe' script consisting of all the actions and scheduling directives that fully define a specific experimental control sequence. These scripts call functions imported from the various modules that compose the QDG control software. The requisite modules are loaded through the **import** command. For example, the DDS module is imported for use using

$$\textbf{from} \quad UTBus1 \quad \textbf{import} \quad \text{DDS} \tag{7.1}$$

where, in this case, 'UTBus1' is the path where the modules are stored and represents the first version of the UTBus.

The following is a sample script used for an experimental sequence in the Miniature Atom Trap (MAT) experiment. It is a basic script, more complex scripts are possible but are beyond the scope of this thesis to discuss.

```
from math import sin,cos
import socket
import sys
```

```
from UTBus1 import Recipe
from UTBus1 import AnalogOutput
from UTBus1 import DigitalOutput
from UTBus1 import DDS

KHz = 1000.
MHz = 1000000.

R = Recipe(r"D:\tmp\bcode.utb",
           use_internal_clock=True,
           sampling_frequency_divider=2000,
           use_external_trigger=False)

R.start()

# ----------------- UT Bus Device instantiations  ---------------


MATCoolingAOM = DDS(address=136,refclock=15*10**6,refclock_multiplier=20,
             internal_FSK=False)

MATRepumpAOM = DDS(address=124,refclock=15*10**6,refclock_multiplier=20,
             internal_FSK=False)


# ----------------- MAT DDS Setup for Synchronous detection  ---------------

if 1:

    fRepumpCenter = 80*MHz

    fcenter = 80*MHz
    df = 0*MHz
    f2 = fcenter + df
    f1 = fcenter - df
    D = .00001

    MATCoolingAOM.reset()
    MATRepumpAOM.reset()

    MATCoolingAOM.single_tone(f1)
    MATRepumpAOM.single_tone(fRepumpCenter)

#  This command produces a frequency ramp from f1 to f2 in D seconds
```

```
    MATCoolingAOM.ramped_FSK(f1,f2,D)

    MATCoolingAOM.set_amplitude(0.7)
    MATRepumpAOM.set_amplitude(0.7)

    DO2 = DigitalOutput(address=255)
    DO2.set_bit(7,1)


R.end()
```

Chapter 8

Measurements

8.1 MOT Optimization

Our experimental apparatus has been constructed to support the simultaneous trapping of Li and Rb atoms. Single species trapping of Rb atoms is a well established technique; as is shown by preliminary measurements of the steady state atom number for our system in a single species Rb MOT configuration [2].

The decision to trap Li atoms directly from an effusive source, without any intermediary slowing mechanisms, requires a very careful determination of the steady state atom number, the loading time, and the loading rate over the entire parameter space of the experimental system. This is necessary not only to maximize the initial atom number, but also to determine if this method is viable as a means of eventually generating ultracold molecules from a dual species MOT. The results, and discussion, that follow is specific to the performance of the Li MOT in absence of any Rb vapour.

8.1.1 Alignment

Originally, the cooling and trapping light in each axis was split by way of a polarization beam splitter (PBS) to generate two beams propagating in opposite directions. This method allows for adjustments to be made to the intensity balance of each beam pair, although this results in the total intensity of the incoming light being shared across the two beams.

Unfortunately, our Lithium slave lasers on the photoassociation table have output powers of only 28mW [60]. Methods of increasing the intensity are being discussed, but they could not be immediately implemented within the existing system. Instead it was decided to resort to a retroreflection setup, where the cooling beams are sent directly through the trapping cell, then reflected back by way of retroreflecting mirrors. This proved to be a simple way to essentially double the intensity of the cooling light, giving atom numbers of approximately 2×10^7[2]. Due to the simplicity of the optical components, this method makes it easier to spatially overlap the beams. The reason this method was not used initially is that the intensity losses at each interface of the trapping cell result in an intensity imbalance between the beams. This imbalance pushes the center of the MOT away from the center of the magnetic field.

8.1.2 Atom Number Calibration

In general, the number of atoms in a MOT is related to the current signal from a photodiode by

$$N_{atom} = \frac{I_{PD}}{L \cdot \eta \cdot R \cdot \left(\frac{hc}{\lambda} \cdot \Gamma_{scatt}\right)} \tag{8.1}$$

where I_{PD} is the current from the photodiode, L is the signal loss due to optical components, η is the collection efficiency of the detection system, R is the responsivity of the photodiode in millivolts. The signal loss due to optical components was calculated to be $L = 0.307$. The light propagates through the trapping cell, two lenses, a dichroic mirror, and an interference filter before reaching the photodiode. The collection efficiency of the system is based on the solid angle of the imaging optics with the MOT as the center. The lens is 75mm in diameter and is placed 11.8mm from the MOT, giving a value of $\eta = 5.78 \times 10^{-3}$. Finally, the responsivity of the photodiode is $R = 0.38$A/W and is given as a manufacturer's specification. For a 2-level system, the scattering rate Γ_{scatt} is related to the frequency detuning (δ) of the cooling light by

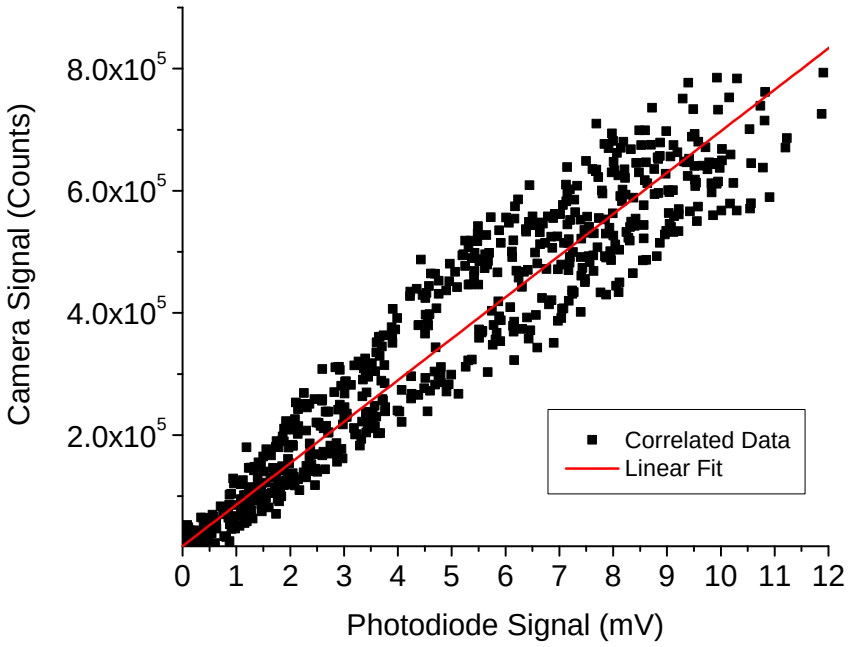

Figure 8.1: The relationship between the fluorescence signal from the CCD camera and the photodiode. The photodiode signal has been calibrated with the atom number; a linear fit allows for the camera signal to be likewise converted.

$$\Gamma_{scatt} = \frac{\Gamma}{2} \frac{s}{1 + s + \left(\frac{2\delta}{\Gamma}\right)^2} \tag{8.2}$$

where Γ is the natural linewidth of the atomic transition, and $s = I/I_{sat}$. Table (8.1) gives the respective values for the atomic species used in our dual MOT experiment. Since the detection of a photon is predicate on an atom being trapped in the MOT, it is assumed that each signal event within a time period smaller than the scattering

rate corresponds to a single atom within the MOT. By factoring the total efficiency of the detection system, we can determine a reasonable estimate of the atom number from the signal from a photodiode.

Species	Γ	s
^{6}Li	$(2\pi) \cdot 5.87$MHz	19.7
^{85,87}Rb	$(2\pi) \cdot 6.06$MHz	14.8

Table 8.1: Natural linewidths and values of $s = I/I_{sat}$ for the atomic species used in our experiment.

This calibration calculation was worked through for a photodiode signal of $I_{PD} = V_{PD}/1\text{M}\Omega = 11\text{nA}$, and detuning values of $\delta = \delta_p^o = \delta_r^o = (2\pi) \times (-34\text{MHz})$. The number of atoms was found to be

$$N_{atom} = 2.07 \times 10^7 \tag{8.3}$$

Using this value, it is possible to estimate the atom number of the MOT under other conditions.

8.1.3 MOT Loading Model

The loading behaviour of a MOT determined by two parameters; the capture rate of atoms into the trap, and the loss rate of atoms out of the trap. A simple differential equation suffices in describing the time dependence of the trapped atom number

$$\dot{N} = R - \gamma N \tag{8.4}$$

where N is the number of atoms, R is the loading rate, and γ is the loss rate due to collisions with both background atoms such as Hydrogen, and hot, untrapped Li and Rb atoms. Solving the differential equation for N gives

$$N = \frac{R}{\gamma}\left(1 - e^{-\gamma t}\right) \tag{8.5}$$

where we can define the value $N_{ss} = R/\gamma$ as the steady state atom number. The loading time is defined as the inverse of the loss rate $\tau = 1/\gamma$. This represents the time required to fill the trap to the steady state atom number, as well as the average time an atom exists in the trap before being expelled through a collision event.

As shown in Fig. (8.2), the loading model fits the experimental data extremely well.

8.1.4 Detuning

The frequencies of both the pump (cooling) and repump light greatly affects the number of atoms trapped in the MOT. The magnitude of the detuning from resonance

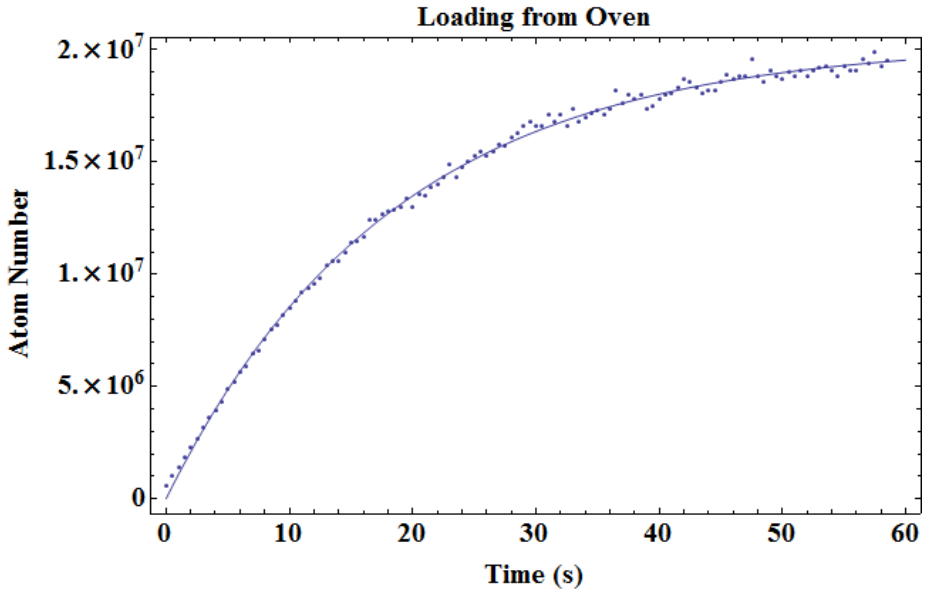

Figure 8.2: Fluorescence from a CCD camera was recorded every 500ms over the duration of the loading period of a Li MOT. The fluorescence was converted to atom number and fit using equation (8.5). The values of the parameters were found to be $R = 1.1 \times 10^6$ and $\gamma = 0.054$. This corresponds to a loading time of $\tau = 18.2sec$.

partially determines the maximum accessible velocity class of atoms. An empirical determination of the optimum detunings δ_p and δ_r was performed by collecting data on the fluorescence over the entire detuning space. A control script was written to iteratively load a MOT and capture the fluorescence level using both a CCD camera and a photodiode. The parameters δ_p, δ_r, and I_{coil}, where I_{coil} is the current supplied to the magnetic coils, were systematically varied during each iteration. The fluorescence emitted by the trapped atoms in the MOT was recorded using both a photodiode and a CCD camera. The photon count of the CCD camera is measured by integrating over the pixel range of the image; because of this, the exposure time of the camera must be taken into account when deriving quantities such as the atom number. Fig. (8.4) shows a sample comparison of the raw data at a magnetic coil current of $I_{coil} = 4$A. Although the regions of maximum fluorescence do not coincide exactly, the spatial overlap suggests that a detuning of $\delta_p/(2\pi) = -34$MHz and $\delta_r/(2\pi) = -25$MHz should provide a maximized fluorescence signal.

In order to determine the atom number from the photon count of the camera signal, it is necessary to first determine the relationship with respect to the photodiode voltage signal. It was observed that the position of the MOT within the trapping cell changed in relation to the frequencies of the light and the current to the magnetic coil. There was concern that this positional variation would cause the MOT image to stray beyond the capture range of the photodiode. Fortunately, the data suggests that this concern was unwarranted for this particular sequence. The best fit to the data is a linear equation that was then used to convert the camera signal to an equivalent voltage.

The scattering rate, and hence the atom number, is dependent on the frequency

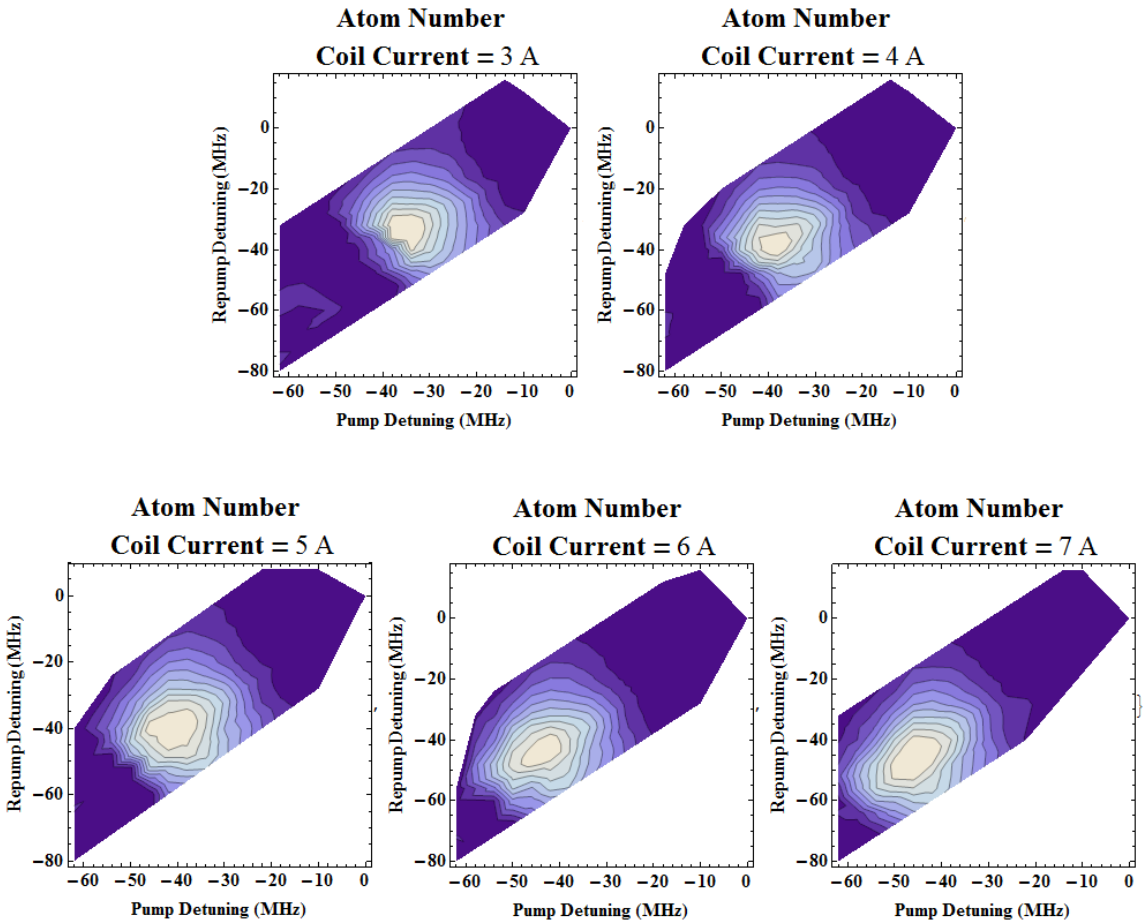

Figure 8.3: Atom number vs. laser detunings for increasing values of the magnetic coil current (I_{coil}). The coil current is proportional to the magnetic field gradient. Note the shift of the maximum atom number towards higher detuning values as the current is increased. The peak atom number of 2.61×10^7 atoms is found at $\delta_p = -42$MHz, $\delta_r = -44$MHz, and $I_{coil} = 7$A. For our experiment a reference current of 2.84A was measured to produce a magnetic field of 16.8G/cm.

detuning of the cooling light. Since both frequencies contribute to the cooling of the atoms, it was necessary to incorporate the changing values of δ_p and δ_r into the calculation. It is clear that the actual value of Γ_{scatt} is bounded by those calculated using the minimum and the maximum of the detuning frequencies

$$\Gamma_{scatt}(\mathrm{Min}[\delta_p, \delta_r]) \leq \Gamma_{scatt}(\delta_p, \delta_r) \leq \Gamma_{scatt}(\mathrm{Max}[\delta_p, \delta_r]) \tag{8.6}$$

In order to simplify the calculation, and to determine a lower bound on the atom number, the detuning that minimizes Γ_{scatt} was used. The atom number was then calculated from

$$N_{atom} = \left[\frac{V_{Cam}}{V_{Cam}^{ref}}\right] \times \left[\frac{\Gamma_{scatt}^{ref}}{\Gamma_{scatt}(\mathrm{Min}[\delta_p, \delta_r])}\right] \times (2.07 \cdot 10^7) \tag{8.7}$$

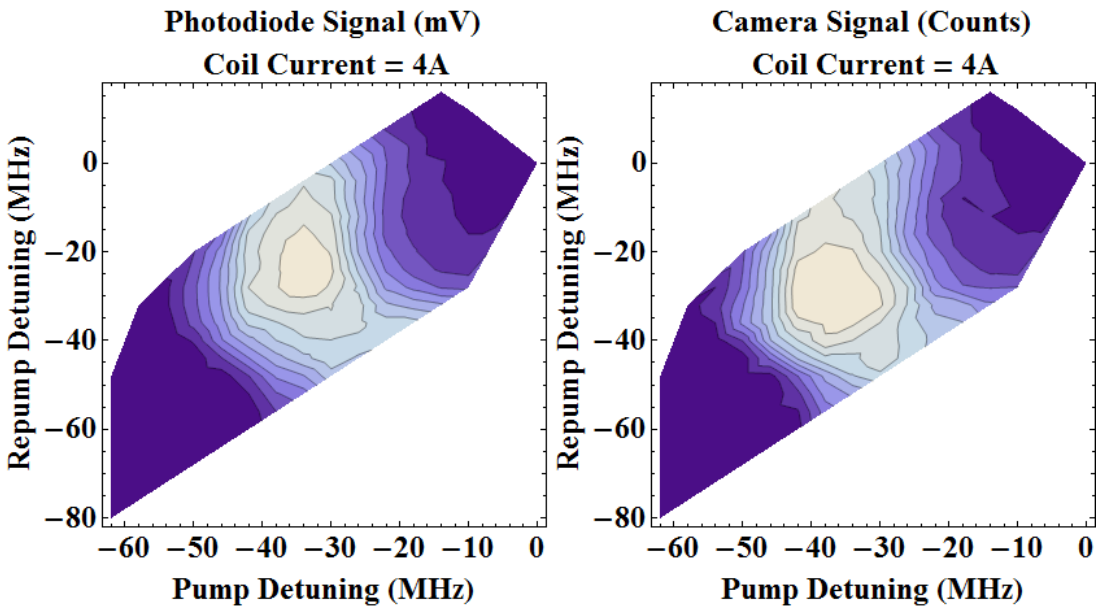

Figure 8.4: Sample contour plots at $I_{coil} = 4A$ showing the raw fluorescence data for both the CCD camera signal and the photodiode signal.

where $V_{Cam}^{ref} = 11\text{mV}$ and $\Gamma_{scatt}^{ref} = 2.45 \cdot 10^6$.

Fig.(8.3) shows the relationship between the atom number and the relative detunings of the pump and repump. It is clear that the values of the detunings that maximize the fluorescence signal are not necessarily those that maximize the atom number in the MOT. This means that there are two optimal detuning positions; the first where the atom number is largest, and the second where the fluorescence signal is maximized. The former is used when loading a MOT, while the second can be quickly shifted during a measurement in order to enhance the signal as much as needed to make a measurement.

8.1.5 Intensity Dependence

The relative intensities of the pump and repump beams also are important in maximizing the atom number of our Li MOT, as well as determining the need for an additional amplification stage before the light is sent to the MOT. In this measurement, the frequency detunings were held fixed at $\delta_p = (2\pi) \times (-34\text{MHz})$ and $\delta_r = (2\pi) \times (-25\text{MHz})$, with a magnetic coil current of $I_{coil} = 4\text{A}$.

The intensities were adjusted through the use of an electro-optic modulator placed between the output port of the optical isolators of the Lithium slave lasers and a PBS cube. In this way, both the pump and repump intensities could be independently controlled. Fig (8.5) shows the relationship to the atom number over the range of pump and repump powers. The total atom numbers present at higher pump and repump powers is promising, although the need for further amplification remains unresolved. The apparent plateau in the atom number as the pump power was changed may mean that our existing system is adequate, but this is far from a definitive result. For the

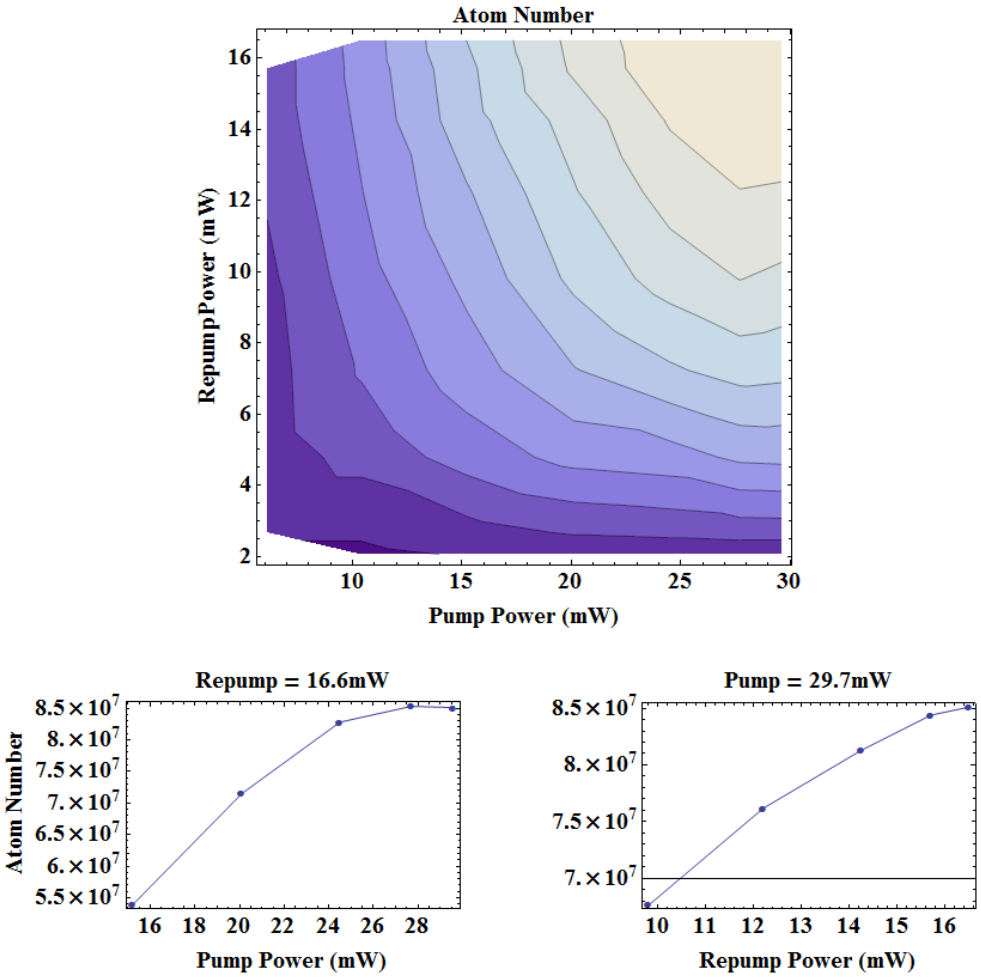

Figure 8.5: Clockwise from top: (a) Contour plot showing the atom number present in the MOT as a function of the light intensity of the pump and repump beams. (b) Increasing atom number for fixed pump power. (c) Increasing atom number for fixed repump power

purposes of the first generation experiment, the output of the Lithium slave lasers will be left unmodified.

It is useful to determine the corresponding intensity values of the pump and repump beams in each axis. In a retroreflection scheme, the reflected beam will incur greater loss due to interactions with the trapping cell and mirror. Table (8.2) shows the total intensities for the primary and reflected beams for the pump and repump in all three axes at maximum power values with corresponding transmission coefficients. The effect of the trapping cell on the intensity of the reflected beams, especially for s polarized light, is non-negligible. As stated earlier, this will reduce the efficiency of the cooling light, while also shifting the position of the atomic cloud relative to the zero field of the magnetic trap. Within the MOT, there exist fine structure changing

Beam	Power (mW)	Intensity (mW/cm^2)	T_s	T_s^3	T_p	T_p^3
Pump$_x$	14.77	18.70	0.837	0.587	0.986	0.957
Pump$_y$	5.83	7.38	0.837	0.587	0.986	0.957
Pump$_z$	2.1	2.66	0.929	0.863	0.929	0.863
Repump$_x$	4.1	5.19	0.837	0.587	0.986	0.957
Repump$_y$	4.3	5.44	0.837	0.587	0.986	0.957
Repump$_z$	4.3	5.44	0.929	0.863	0.929	0.863

Table 8.2: Intensities of Pump and Repump Beams in each axis with primary and reflected beam transmission factors for both s and p polarizations. The transmission coefficient determines the intensity value of the light when it reaches the MOT.

collisions where

$$\mathrm{Li}^*_{upper} + \mathrm{Li} \rightarrow \mathrm{Li}^*_{lower} + \mathrm{Li} + Energy \tag{8.8}$$

These collisions result in an increased velocity of the atom. According to [61], if the intensity of the cooling light is sufficiently high, it is possible to recapture the atoms from these fine-structure changing collisions. This recapture leads to heating in the trap, but increases the equilibrium atom number. Currently, with the exception of the primary pump beam in the x-axis, we are below the 15mW/cm^2 intensity observed to produce a trap depth sufficient to contain the atoms from these collisions. This means that we should continue to see gains from the recapture of these atoms as we increase the intensity of beams in all three axes.

The total atom numbers present at higher pump and repump powers is promising, although the need for further amplification remains unresolved. The apparent plateau in the atom number as the pump power was changed may mean that our existing system is adequate, but this is far from a definitive result. For the purposes of the first generation experiment, the output of the Lithium slave lasers will be left unmodified.

8.1.6 Oven Current

Finally, loading curves were taken for multiple oven currents and compensation z-coil current. This was done in order to determine the efficacy of our beam block in shielding the MOT from atoms escaping from the oven. The change in current changes the vertical position of the atom cloud within the trapping region. If the beam block is functioning as is expected, it is predicted that as the MOT is positioned beyond the shielded trapping region, the loss rate due to collisions with hot Lithium atoms should increase sharply. This would result in a sudden decrease in the loading time of the MOT.

The oven temperature is controlled through a resistive heating element, and is directly related to the flux of atoms from the collimated beam source. Increasing the atom flux from the oven increases the number of atoms below the capture velocity of the MOT, but also increases the contribution from non-capturable atoms to collisional

losses. It is important to determine the oven current at which these various effects are balanced.

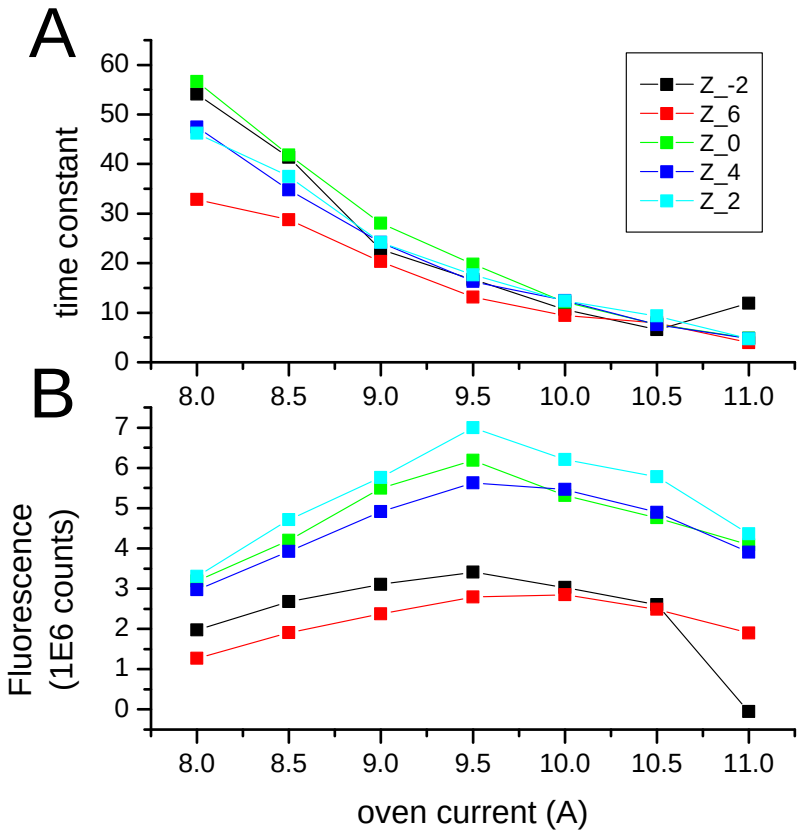

Figure 8.6: Fluorescence measurements and loading times determined as a function of oven current for multiple compensation z-coil voltages. These voltages correspond to currents, which in turn correspond to magnetic fields. These magnetic fields determine the MOT position within the trapping cell. Higher oven currents result in a larger flux of atoms, but with an increased shift in the velocity profile. Altering the voltage to the compensation z-coil shifts the MOT position relative to the center of the trapping field and was done to observe the effect of the beam block.

Fig.(8.6) demonstrates the effect of increasing oven temperature on both the loading time, and the fluorescence of the MOT. The fluorescence was measured on a Pixelink CCD camera every 500ms, with an exposure time of 6ms, during the loading stage of the MOT. When increasing the oven current, a time delay is required in order allow the oven to reach temperature before taking further measurements. Each data point of the fluorescence corresponds to the value obtained after fully loading the MOT.

The expected decrease in the loading time as the MOT was positioned outside the shielded region of the trap was not observed. The loading times remained consistent across all MOT positions at a given oven current. The fluorescence was maximized

at an oven current of 9.5A.

8.1.7 Conclusions

We have shown that loading from an effusive Lithium oven without the use of a traditional slowing mechanism is a viable method for producing atomic clouds in excess of 10^7 atoms. Considering the size, cost, and experimental complexity of incorporating a Zeeman slower into a vacuum system, this result is particularly useful for those situations where large atom numbers are not necessary within the context of the experiment to be performed. It is possible that refinements in the second generation experiment may lead to further gains.

Although this is a very promising result, the performance of the Li MOT within the context of a dual species system with Rb remains to be examined. It is expected that the added losses due to background collisions with the Rb atoms will decrease the steady state atom number of the Li MOT, but the magnitude of this decline is currently unknown.

8.2 Ablation Loading

It has been demonstrated that intense UV or broad-band light can significantly increase the background vapour pressure of certain species of alkali atoms [62]. This process is due to light-induced atomic desorption (LIAD), and has been shown to produce optically thick rubidium, potassium, and sodium atomic vapour. In a vapour cell, there exists a coating of alkali atoms on the inner surface. When light is incident on the inner surface, the atoms present in this coating are quickly desorbed from the cell wall; resulting in an increased vapour pressure and a higher number of trapped atoms. Since the light can be shuttered quickly, this method can be used to build large trap numbers while returning quickly to low background pressures.

Lithium atoms quickly adsorb to any available surface; the effusive atomic beam from our Li oven is blocked not only to create a sheltered region where the MOT resides, but also to limit the atoms from completely covering the optical access to the trapping region. Although the block was designed to keep specific areas of the trapping cell clean, there do exist regions of the cell where Li atoms from the oven are deposited on the surface. Fig.(8.7) shows the accessible area of deposited Lithium used in the desorption/ablation test.

Unlike Rubidium, the energy required to remove a Li atom from the adsorbed surface layer is larger than that supplied by a diffuse UV source. Access to a pulsed YAG laser, frequency doubled to 532nm, led to an interest in determining the viability of loading the Lithium MOT from a desorption/ablation source instead of the effusive oven.

8.2.1 Experimental Procedure

The frequency detunings were held fixed at $\delta_p = (2\pi) \times (-34\text{MHz})$ and $\delta_r = (2\pi) \times (-25\text{MHz})$, with the magnetic coil currents set to $I_{coil} = 4A$.

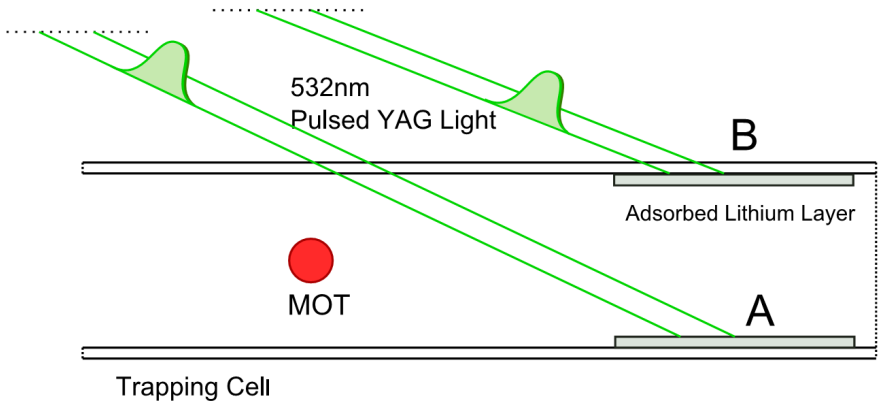

Figure 8.7: The adsorbed Lithium layer is present on all sides of the trapping cell, extending in a thin layer approximately 9mm past the position of the beam block. Ablation loading was tested first by directing the pulsed YAG light on the Lithium-Vacuum interface at the bottom of the cell (**A**), then by directing it on the Glass-Lithium interface at the top of the cell (**B**).

It is possible to trigger the pulsed YAG laser externally using a TTL signal. The signal was sent to the flashlamp input of the laser, with the Q-switch trigger set to trigger automatically from the flashlamp. Although this method introduces an increased noise in the total pulse power and timing interval of the output, these effects were deemed inconsequential considering the nature of the test.

The magnetic coils were turned off, clearing the system of any residual trapped atoms. With the coils off, ten background images, one every 10ms with an exposure time of 25ms, were taken as reference. The coils were then turned back on, with a further 10 images taken at 500ms intervals. These images were taken to ensure that the Lithium oven had cooled sufficiently and was no longer contributing atoms to the system. At this point, a pulsed YAG laser (20mJ pulses at 10Hz) was triggered using a Digital Output device. Images were collected from the Pixelink CCD camera every 500ms for a 60s duration, at which point the laser was turned off. Images continued to be taken every 500ms for a further 120s to measure the decay characteristics of the MOT.

A reference loading curve from the effusive Li oven was taken both as a comparison of the efficiency of the ablation method, and as a calibration for converting the camera signal to atom number, this is the data shown in Fig. (8.2).

Two positions were chosen for the ablation laser; the first on the lower surface of the trapping cell, so that the pulsed light was directed on the interface between the vacuum and the deposited Lithium layer, and the second on the upper surface so that the light was directed on the interface between the glass cell and the deposition layer. Three separate trials were taken at each position; the beam alignment was left unaltered to determine the effect of depletion on the loading rates.

8.2.2 Results

Fig. (8.8) shows the data collected while exposing the lower surface to the pulsed laser source. When compared to a loading curve taken with an effusive oven source, it is clear that the ability of the laser to produce high atom numbers for capture in the MOT is limited. Fitting the data from these trials to the MOT loading model gives loading and loss rates summarized in Table (8.3). The decrease in the loading rate and loss rate for each subsequent trial is most likely due to the depletion of the lithium layer where the pulsed light is hitting. This depletion means that fewer atoms are present to be released into the trapping region and collected.

Trial	Loading Rate R	Loss Rate γ	Load time τ (s)
Oven	1.1×10^6	0.055	18.2
1	5.4×10^4	0.122	8.2
2	1.4×10^4	0.035	28.6
3	8.6×10^3	0.026	38.5

Table 8.3: Loading rate and loss rates for ablation loading trials on surface **A**.

Although the loading from this surface was not great, the decay rates of the MOT after the laser light has been turned off is an important indication of the loss rate due solely to background gases present in the vacuum. Fitting an exponential decay to the data of the form

$$N(t) = N_o e^{-\gamma t} \tag{8.9}$$

gives a decay time of $\tau = 120.3s$ which is much longer than the initial load time of the MOT.

Fig. (8.9) shows the loading of the MOT when the pulsed laser is directed at the upper surface (**B**) of the Lithium-Cell interface. The data shows a markedly different response than for that of the previous test. The MOT is quickly loaded from the high flux of initial atoms. This flux is not maintained however, and the atom number of the MOT begins to decay to some new steady state value. Clearly, the flux of atoms, and the release of contaminants bound in the lithium layer changes quickly during the first few seconds of the loading sequence. It is interesting that the peak atom number is much higher than that for the previous test, and that the depletion of the lithium layer is much more pronounced as is shown by the extremely small signal detected during the third trial. A clue that the contamination is much higher during this test is the decay rate of the MOT once the laser light as been turned off, found to be $\tau = 7.5s$. Similar to the test on the bottom surface, the supply of Lithium atoms should cease instantaneously as it is quickly adsorbed to the surface of the cell or pumped out of the system. This means that any discrepancies in the decay time of the MOT between the two tests can only be attributed to the release of particles that had been trapped in the lithium layer on the cell surface.

8.2.3 Conclusions

The exact heating mechanisms and chemical composition of the deposition layers are not well understood. As such, conjecture as to the processes by which the two very different loading curves were created will be left for further review. The purpose of the test was to determine the viability of laser ablation as a means of loading a Lithium MOT. To this end, laser ablation has been shown effective in quickly loading a small atom number MOT while maintaining a very low residual gas vapour pressure. Unlike an oven source, this method allows for near instantaneous generation and cessation of background Lithium vapour.

Beyond the limited atom numbers, there are further concerns in regard to the random direction of the Lithium atoms when vapourized in this manner. Great care has been taken in the design of the effusive Lithium oven to ensure that contamination of the optical access of the trapping cell is minimized.

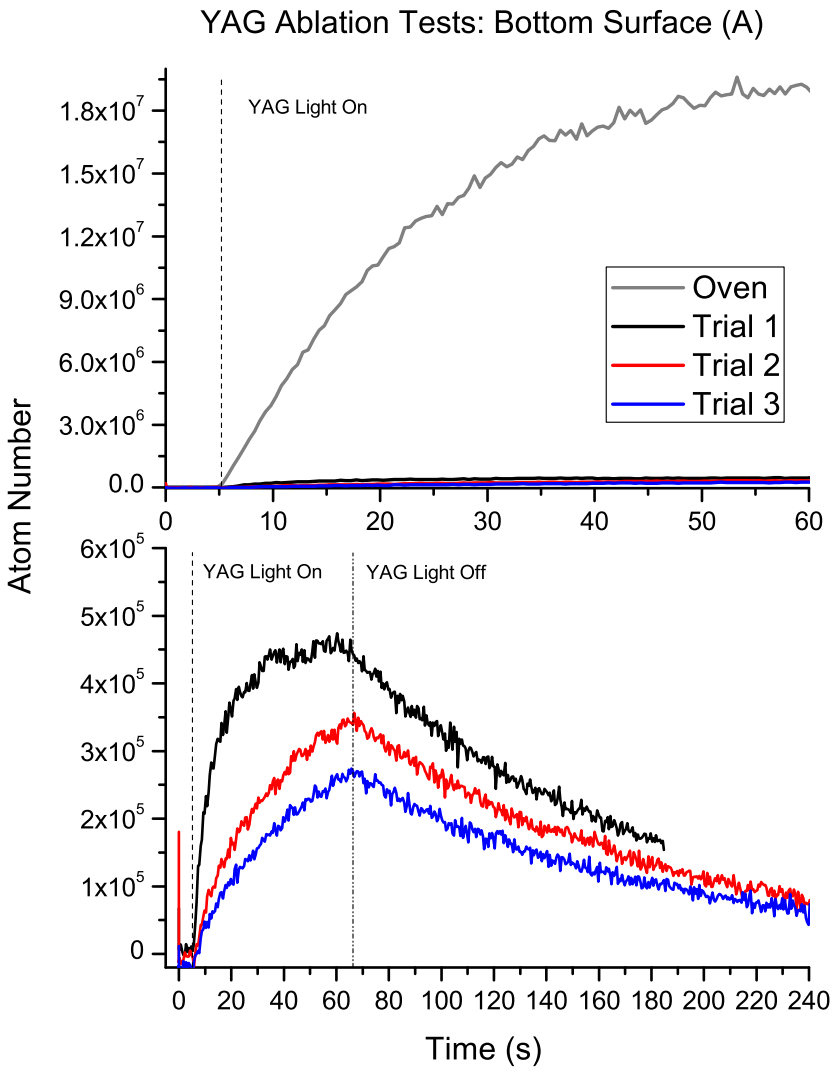

Figure 8.8: **Top**: A Li MOT is loaded by means of laser ablation at the interface of the vacuum-Lithium layer, as well as from an effusive oven source. The laser is triggered at the 5 second mark. **Bottom**: Increased view of the loading and decay curves of the laser ablation trials. The beam positon was held fixed throughout. The laser light is turned off 60 seconds after being triggered. The decay time for each of the three trial are calculated to be $\tau_1 = 118.2$s, $\tau_2 = 120.3$s, and $\tau_3 = 119.2$s.

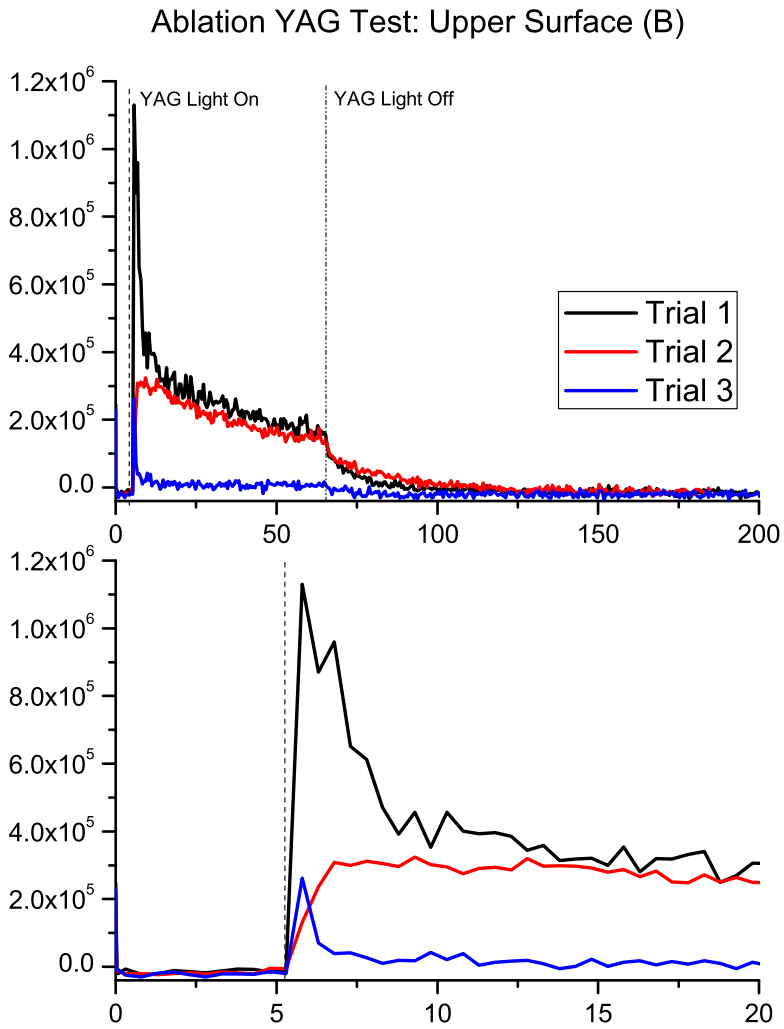

Figure 8.9: **Top**: A Li MOT is loaded by means of laser ablation at the glass-Lithium layer interface. Shown are the loading and decay periods for multiple trials at a single beam location. The laser light was triggered at the 5 second mark, and turned off 60 seconds later. The depletion of the deposition layer is significant as the atom number of the final trial is nearly nonexistent. The decay rate of the trapped atoms after the YAG light has been turned off is $\tau = 14.5$s. **Bottom**: A short time scale view of the initial loading conditions. The early spike in the atom number is maintained over four images at 500ms intervals. The laser is pulsed at 10Hz.

Bibliography

[1] Swati Singh. Progress towards ultra-cold ensembles of rubidium and lithium. Master's thesis, University of British Columbia, 2007.

[2] Nina Rauhut. Towards ultracold LiRb molecules. Master's thesis, Ludwig Maximilians Universität München, 2007.

[3] Todd P. Meyrath and Florian Schreck. Digital RF synthesizer: DC to 135MHz. Technical report, Atom Optics Laboratory Center for Nonlinear Dynamics University of Texas at Austin, 2005.

[4] Todd P. Meyrath and Florian Schreck. Octal 16-bit DAC. Technical report, Atom Optics Laboratory Center for Nonlinear Dynamics University of Texas at Austin, 2005.

[5] K.-A. Suominen. Theories for cold atomic collisions in light fields. *Journal of Physics B Atomic Molecular Physics*, 29:5981–6007, 1996.

[6] T.W. Hänsch and A.L. Schawlow. Cooling of gases by laser radiation. *Optics Communications*, 13, January 1975.

[7] M. H. Anderson, J. R. Ensher, M. R. Matthews, C. E. Wieman, and E. A. Cornell. Observation of Bose-Einstein Condensation in a Dilute Atomic Vapor. *Science*, 269(5221):198–201, 1995.

[8] K. B. Davis, M. O. Mewes, M. R. Andrews, N. J. van Druten, D. S. Durfee, D. M. Kurn, and W. Ketterle. Bose-einstein condensation in a gas of sodium atoms. *Phys. Rev. Lett.*, 75(22):3969–3973, 1995.

[9] D. DeMille. Quantum computation with trapped polar molecules. *Phys. Rev. Lett.*, 88(6), 2002.

[10] J.H. Eberly P.W. Milonni. *Lasers*. John Wiley and Sons, 1988.

[11] Y.B Ovchinnikov R. Grimm, M. Weidemller. *Rev. Sci. Instrum.*, 42:95, 2000.

[12] C.J. Foot. *Atomic Physics*. Oxford University Press, 2005.

[13] P. D. Lett, W. D. Phillips, S. L. Rolston, C. E. Tanner, R. N. Watts, and C. I. Westbrook. Optical molasses. *J. Opt. Soc. Am. B*, 6(11):2084, 1989.

[14] E. L. Raab, M. Prentiss, Alex Cable, Steven Chu, and D. E. Pritchard. Trapping of neutral sodium atoms with radiation pressure. *Phys. Rev. Lett.*, 59(23):2631–2634, 1987.

[15] Wolfgang Petrich, Michael H. Anderson, Jason R. Ensher, and Eric A. Cornell. Stable, tightly confining magnetic trap for evaporative cooling of neutral atoms. *Phys. Rev. Lett.*, 74(17):3352–3355, 1995.

[16] H.J. Metcalf and P. van der Straten. *Laser Cooling and Trapping*. Springer, 1999.

[17] Y. Castin, H. Wallis, and J. Dalibard. Limit of doppler cooling. *J. Opt. Soc. Am. B*, 6(11):2046, 1989.

[18] M. Weidemller and C. Zimmermann, editors. *Interactions in Ultracold Gases*. Wiley, 2003.

[19] Daniel A. Steck. Rubidium 87 d line data. Technical report, Los Alamos National Laboratory, 2001.

[20] P. D. Lett, R. N. Watts, C. I. Westbrook, W. D. Phillips, P. L. Gould, and H. J. Metcalf. Observation of atoms laser cooled below the doppler limit. *Phys. Rev. Lett.*, 61(2):169–172, 1988.

[21] J. Dalibard and C. Cohen-Tannoudji. Laser cooling below the Doppler limit by polarization gradients: Simple theoretical models. *Journal of the Optical Society of America B Optical Physics*, 6:2023–2045, 1989.

[22] J. Lawall, F. Bardou, B. Saubamea, K. Shimizu, M. Leduc, A. Aspect, and C. Cohen-Tannoudji. Two-dimensional subrecoil laser cooling. *Phys. Rev. Lett.*, 73(14):1915–1918, 1994.

[23] Mark Kasevich and Steven Chu. Laser cooling below a photon recoil with three-level atoms. *Phys. Rev. Lett.*, 69(12):1741–1744, 1992.

[24] W. Ketterle and N.J. van Druten. Evaporative cooling of trapped atoms. *Advances in Atomic, Molecular, and Optical Physics*, 37:181, 1996.

[25] Naoto Masuhara, John M. Doyle, Jon C. Sandberg, Daniel Kleppner, Thomas J. Greytak, Harald F. Hess, and Greg P. Kochanski. Evaporative cooling of spin-polarized atomic hydrogen. *Phys. Rev. Lett.*, 61(8):935–938, 1988.

[26] A. G. Martin, K. Helmerson, V. S. Bagnato, G. P. Lafyatis, and D. E. Pritchard. rf spectroscopy of trapped neutral atoms. *Phys. Rev. Lett.*, 61(21):2431–2434, 1988.

[27] N. Balakrishnan and A. Dalgarno. Chemistry at ultracold temperatures. *Chem. Phys. Lett.*, 341(5-6), 2001.

[28] J. J. Hudson, B. E. Sauer, M. R. Tarbutt, and E. A. Hinds. Measurement of the electron electric dipole moment using YbF molecules. *Phys. Rev. Lett.*, 89(2):023003, 2002.

[29] D. Seidel and J.G. Muga. Ramsey interferometry with guided ultracold atoms. *Eur. Phys. J. D*, 41(1), 2007.

[30] R. deCarvalho, J.M. Doyle, B. Friedrich, T. Guillet, J. Kim, D. Patterson, and J.D. Weinstein. Buffer-gas loaded magnetic traps for atoms and molecules: A primer. *Eur. Phys. J. D*, 7(3), 1999.

[31] Jinha Kim, Bretislav Friedrich, Daniel P. Katz, David Patterson, Jonathan D. Weinstein, Robert DeCarvalho, and John M. Doyle. Buffer-gas loading and magnetic trapping of atomic europium. *Phys. Rev. Lett.*, 78(19):3665–3668, 1997.

[32] Hendrick L. Bethlem, Giel Berden, and Gerard Meijer. Decelerating neutral dipolar molecules. *Phys. Rev. Lett.*, 83(8):1558–1561, 1999.

[33] J. Doyle, B. Friedrich, R.V. Krems, and F. Masnou-Seeuws. Editorial: Quo vadis, cold molecules? *Eur. Phys. J. D*, 31(2), 2004.

[34] H. R. Thorsheim, J. Weiner, and P. S. Julienne. Laser-induced photoassociation of ultracold sodium atoms. *Phys. Rev. Lett.*, 58(23):2420–2423, 1987.

[35] John Weiner, Vanderlei S. Bagnato, Sergio Zilio, and Paul S. Julienne. Experiments and theory in cold and ultracold collisions. *Rev. Mod. Phys.*, 71(1):1–85, 1999.

[36] Y. B. Band and P. S. Julienne. Ultracold-molecule production by laser-cooled atom photoassociation. *Phys. Rev. A*, 51(6):R4317–R4320, 1995.

[37] Warren T. Zemke and William C. Stwalley. Long-range potential energy curves for the $X^1\Sigma^+$ and $a^3\Sigma^+$ states of NaRb. *The Journal of Chemical Physics*, 114(24), 2001.

[38] H. Smith C.J. Pethick. *BEC in dilute gases.* Cambridge University Press, 2002.

[39] C. A. Stan, M. W. Zwierlein, C. H. Schunck, S. M. F. Raupach, and W. Ketterle. Observation of feshbach resonances between two different atomic species. *Phys. Rev. Lett.*, 93(14):143001, 2004.

[40] S. Inouye, J. Goldwin, M. L. Olsen, C. Ticknor, J. L. Bohn, and D. S. Jin. Observation of heteronuclear feshbach resonances in a mixture of bosons and fermions. *Phys. Rev. Lett.*, 93(18):183201, 2004.

[41] B. Deh, C. Marzok, C. Zimmermann, and P. W. Courteille. Feshbach resonances in mixtures of ultracold ^{6}Li and ^{87}Rb gases. *Phys. Rev. A*, 77(1), January 2008.

[42] Thorsten Köhler, Krzysztof Góral, and Paul S. Julienne. Production of cold molecules via magnetically tunable feshbach resonances. *Reviews of Modern Physics*, 78(4):1311, 2006.

[43] S. J. J. M. F. Kokkelmans, H. M. J. Vissers, and B. J. Verhaar. Formation of a bose condensate of stable molecules via a feshbach resonance. *Phys. Rev. A*, 63(3):031601, 2001.

[44] R. V. Krems. Controlling collisions of ultracold atoms with dc electric fields. *Physical Review Letters*, 96(12), 2006.

[45] Michael E. Gehm. Properties of ^{6}Li. Technical report, 2003.

[46] K. B. MacAdam, A. Steinbach, and C. Wieman. A narrow-band tunable diode laser system with grating feedback, and a saturated absorption spectrometer for Cs and Rb. *American Journal of Physics*, 60:1098–1111, December 1992.

[47] C. E. Wieman and L. Hollberg. Using diode lasers for atomic physics. *Review of Scientific Instruments*, 62:1–20, 1991.

[48] Cunyun Ye. *Tunable External Cavity Diode Lasers*. World Scientific, 2004.

[49] M. de Labachelerie and G. Passedat. Mode-hop suppression of littrow grating-tuned lasers. *Appl. Opt.*, 32(3):269, 1993.

[50] A. S. Arnold, J. S. Wilson, and M. G. Boshier. A simple extended-cavity diode laser. *Review of Scientific Instruments*, 69:1236–1239, March 1998.

[51] G.C. Bjorklund, M.D. Levenson, W. Lenth, and C. Ortiz. Frequency modulation (FM) spectroscopy. *Applied Physics B: Lasers and Optics*, 32:145–152, November 1983.

[52] G.L. Weissler and R.W. Carlson, editors. *Methods of Experimental Physics: Vacuum Physics and Technology*. Academic Press, 1979.

[53] G.F. Weston. *Ultra-high Vacuum Practice*. Butterworths, 1985.

[54] W. Becker. *Vak. Tech.*, 7:149, 1958.

[55] Michael A. Joffe, Wolfgang Ketterle, Alex Martin, and David E. Pritchard. Transverse cooling and deflection of an atomic beam inside a zeeman slower. *J. Opt. Soc. Am. B*, 10(12):2257, 1993.

[56] Todd Meyrath. Electromagnetic design basics of cold atom experiments. Technical report, Atom Optics Laboratory Center for Nonlinear Dynamics University of Texas at Austin, 2001.

[57] Paul Lebel. Contributions to the ubc quantum degenerate gas lab. Technical report, University of British Columbia, 2005.

[58] Todd P. Meyrath and Florian Schreck. A simple parallel bus computer control system for atomic physics experiments. Technical report, Atom Optics Laboratory Center for Nonlinear Dynamics University of Texas at Austin, 2004.

[59] Paul Lebel and Davy Mitchell. Ultrafast mechanical shutters for laser cooling application: the iShutter system. Technical report, University of British Columbia, 2008.

[60] Janelle Van Dongen. Simultaneous cooling and trapping of ^{6}Li and ^{85,87}Rb. Master's thesis, University of British Columbia, 2007.

[61] N. W. M. Ritchie, E. R. I. Abraham, Y. Y. Xiao, C. C. Bradley, R. G. Hulet, and P. S. Julienne. Trap-loss collisions of ultracold lithium atoms. *Phys. Rev. A*, 51(2):R890–R893, 1995.

[62] S. N. Atutov, R. Calabrese, V. Guidi, B. Mai, A. G. Rudavets, E. Scansani, L. Tomassetti, V. Biancalana, A. Burchianti, C. Marinelli, E. Mariotti, L. Moi, and S. Veronesi. Fast and efficient loading of a rb magneto-optical trap using light-induced atomic desorption. *Phys. Rev. A*, 67(5):053401, 2003.